GEORG-AUGUST-UNIVERSITÄT
GÖTTINGEN IN PUBLICA COMMODA SEIT 1737

Tripartite Information and Scrambling in Quantum Many-Body Systems

Dissertation

for the award of the degree

Doctor rerum naturalium

of the Georg-August-Universität Göttingen

within the doctoral program *Physics*

of the Georg-August University School of Science (GAUSS)

submitted by

Niklas Bölter

from Celle

Göttingen, 2023

Thesis Advisory Committee

Prof. Dr. Stefan Kehrein

Institute for Theoretical Physics
Georg-August-Universität Göttingen

Prof. Dr. Fabian Heidrich-Meisner

Institute for Theoretical Physics
Georg-August-Universität Göttingen

PD Dr. Salvatore R. Manmana

Institute for Theoretical Physics
Georg-August-Universität Göttingen

Members of the Examination Board

Reviewer: Prof. Dr. Stefan Kehrein

Institute for Theoretical Physics
Georg-August-Universität Göttingen

Second Reviewer: PD Dr. Salvatore R. Manmana

Institute for Theoretical Physics
Georg-August-Universität Göttingen

Further Members of the Examination Board

Prof. Laura Covi, PhD

Institute for Theoretical Physics
Georg-August-Universität Göttingen

Prof. Dr. Matthias Krüger

Institute for Theoretical Physics
Georg-August-Universität Göttingen

Prof. Dr. Michael Seibt

IV. Physical Institute
Georg-August-Universität Göttingen

Prof. Dr. Steffen Schumann

Institute for Theoretical Physics
Georg-August-Universität Göttingen

Date of the oral examination: 2023-05-09

Abstract

This thesis contributes to the study of quantum chaos and thermalization of closed quantum systems by applying tools from quantum information theory.

We study scrambling – the delocalization of quantum information – in one-dimensional quantum many-body systems using the observable-independent tripartite information I_3. We consider closed quantum systems that undergo unitary time evolution governed by a Hamiltonian, and compare them to the strong scrambling caused by random unitary operators (HAAR scrambling). The tripartite information is a tool from quantum information theory that allows us to quantify correlations in space and time by considering the unitary operator evolving the system as a state $|U(t)\rangle$ in a doubled Hilbert space $\mathcal{H} \otimes \mathcal{H}$. We found a ballistic spreading of information in translation invariant systems of spinless fermions that causes HAAR scrambling in interacting models. For strongly disordered versions of the XXZ chain and the transverse-field ISING chain we found a complete breakdown of information transport in non-interacting ANDERSON localized systems, as well as a logarithmically slow spreading of the information signal in systems that are said to be many-body localized (MBL).

Author's Note

Parts of this dissertation have been published in peer-reviewed journals.

- *Tripartite Information, Scrambling, and the Role of Hilbert Space Partitioning in Quantum Lattice Models* [Sch+19]
  O. Schnaack, **N. Bölter**, S. Paeckel, S. R. Manmana, S. Kehrein, and M. Schmitt
  Author's contributions: I contributed to fixing a bug, recalculated all the numerical results that were used to create the figures with my code and did some further investigations into the level statistics and the parity symmetry. All authors discussed the results.
- *Scrambling and Many-Body Localization in the XXZ Chain* [BK22b]
  N. Bölter, S. Kehrein
  Author's contributions: I generated all the raw data and figures and wrote the first draft of the article. Both authors revised the draft together for publication.

Additionally, the results from Section 6.3 are currently in preparation for a publication, and replication data for the already published articles has been published as well in Bölter and Kehrein [BK22a] and Schnaack et al. [Sch+21].

Contents

Chapter 1

Introduction

1.1 Motivation

The transport, storage and processing of digital information has not only become a fundamental part of our society but is also an exciting viewpoint for scientists. Shannon founded (classical) information theory with his seminal paper in 1948 and then quickly proceeded to prove most of its major results [Sha48; Sha49a; Sha49b]. Information theory describes how digital information can be transmitted without any loss of fidelity, which hugely improved existing technologies like telephone, radio and television and paved the way for more advanced computers and computer networks. Other important aspects of information theory are encryption and data compression, both of which are critically important for modern technology like the internet[1]. Physically, no two audio CDs of the same album can be exactly identical – yet through the marvel of information technology the digital data read from them is indistinguishable. Records of our civilization can be preserved for the future without any degradation.

From the perspective of quantum mechanics, we want to understand the inner workings of quantum-mechanical systems, which transport not only chiefly physical properties like energy and momentum, but information as well. Different parts of a quantum system will become correlated as they exchange information, and studying this will allow us both to predict how systems can be used to store and process information and also to make generic observable-independent statements about the behaviour of the system. It is important to stress that information is a part of physical reality and not just a higher-level description

[1] See also `https://youtu.be/z2Whj_nL-x8` Claude Shannon – Father of the Information Age

– for example, Landauer's Erasure Principle shows us that work has to be performed to delete information [Lan91].

Similar to its classical counterpart, the applications of *Quantum Information Theory* could also transform our world. There are *Quantum Computers*, for example, which have become increasingly popular in theoretical studies starting in the early 1980s, showcased by the *Physics of Computation* conference in 1981[2] that was co-sponsored by IBM and MIT [N22]. The keynote speech by Feynman [Fey82], in particular, popularized the idea of quantum computers as universal quantum simulators – in stark contrast to classical computers, a quantum computer can implement the particular features of quantum mechanics natively, which could yield an exponential speedup when the behaviour of a quantum system is simulated. This could provide great benefits to the study of chemical reactions and the properties of condensed matter and biological systems like proteins, which would significantly impact the development of new industrial procedures in chemistry, material science (e.g. improved solar cells, superconductors or energy storage systems) and the development of new medicines [Llo96; Dal+22]. It is worth mentioning that these ideas predate Feynman's speech, notable earlier works include Manin [Man80] and Benioff [Ben80].

In addition to the simulation of quantum systems, quantum computers could potentially also provide large performance boosts when solving other problems, for example, in the fields of optimization and artificial intelligence. Examples include Grover*'s algorithm*, which is a database search algorithm with a quadratic speedup compared to optimal classical solutions [Gro96; Gro01; NC00], as well as the famous Shor*'s algorithm*, which provides an exponential speedup for the prime factorization problem [Sho94]. The search for prime factors of large integer numbers is of particular interest since its complexity guarantees the security of widely used encryption schemes like RSA [RSA78; Ber+17]. The set of problems that can be solved efficiently by universal quantum computers is an open question in *quantum complexity theory*, a review of which can be found in Chapman and Policastro [CP22].

To implement these schemes successfully, however, *fault-tolerant* quantum computers would ideally be used, which do not exist yet. Otherwise, decoherence will destroy the information stored in the quantum computer and prevent calculations of useful length from being carried out [Sho96; Got98]. Similarly to classical information theory, which leads to error correction codes and fault-tolerant classical computations, quantum error correction [KLZ98; Kit03; AB08] could provide the same for quantum computers and is a hot topic in

[2] https://mitendicotthouse.org/physics-computation-conference/

quantum information theory at the moment.

Many quantum computation strategies depend on quantum memory: it should be possible to read and write coherent quantum information in analogy with memory in classical computers. For this, the question of information transport and delocalization that we are studying in this thesis is of utmost importance. Indeed, systems that show many-body localization like those studied in Chapter 6 are potential candidates for quantum memory devices since they retain information about their initial state in localized degrees of freedom instead of thermalizing, a crucial feature of a memory device [NH15].

In addition, there is also *quantum cryptography*, where the BB84 protocol [BB84] had already been published in 1984 in the proceedings of a conference for *Computers, Systems and Signal Processing*, which left most physicists blissfully unaware, and then gained more traction when the E91 protocol [Eke91] was published in *Physical Review Letters* in 1991. Here a secret key can be exchanged by using entangled states and classical communication as resources. Privacy, in this case, is guaranteed by the *monogamy of entanglement*, which does not allow a system controlled by an attacker to be strongly correlated with the systems controlled by the communication partners [CKW00; OV06]. This provides much stronger protection than the classical counterparts, which, for example, depend on the previously mentioned prime factorization problem to be of sufficient complexity to deter attacks. Naturally, this is also a vibrant area of research in quantum information theory because of the promise of perfectly secure communication.

We will, however, limit ourselves in the following to applying quantum information theory to fundamental research of many-body quantum systems while keeping the potential applications in mind.

What are the questions we want to answer? Our main interest lies in *scrambling*, that is the delocalization of information in a closed quantum system with local interactions. An ideal closed quantum system undergoes unitary time evolution described by a Hamiltonian H, which prevents any overall loss of information: quantum states and measurement operators at different times can be mapped onto each other by unitary operators, so the information which is extractable at different times by global measurements is identical. Importantly, however, a measurement operator W that is local at some initial time $t = 0$ can spread over the entire system and couple to a large number of its degrees of freedom as it is evolved according to the HEISENBERG equation of motion even if the Hamiltonian

and the initial operator are simultaneously local in some basis [Hos+16]:

$$W(t) = W + it\,[H, W] - \frac{t^2}{2!}\,[H, [H, W]] - \frac{it^3}{3!}\,[H, [H, [H, W]]] + ... \tag{1.1}$$

At the initial time we could have performed the measurement described by W with only access to a small part of the HILBERT space and were free to trace out the remaining part, but at a much later time we need access to the entire system since the higher order commutators can become long-range operators. In this sense, some of the initially local quantum information has become delocalized (scrambled) across the system.

Scrambling can be diagnosed with the *out-of-time-order* correlators (OTOCs), for example, where a second local operator V is introduced that commutes with W as the two operators are initially localized inside separated parts of the HILBERT space but becomes non-commuting with $W(t)$ as it spreads under time evolution, i.e. $[W(t), V] \neq 0$ [Hos+16]. As OTOCs show us how two areas in the system become correlated over time, picking local operators with different separations, we can gain insight into information transport by plotting the buildup of spatiotemporal correlations in a lightcone visible in a distance vs time plot.

The buildup of correlations can also be measured with the *entanglement entropy* $S_A = -\mathrm{Tr}\rho_A \log_2 \rho_A$ of the reduced density matrix $\rho_A = \mathrm{Tr}_B \rho$ describing one part of a bipartite system AB. In this case, the initial state should be some state with low entanglement between the two regions, such that the buildup over time can be seen. This method has the advantage that it is observable-independent and can be used to make generic statements about the systems.

We will use a third approach, the so-called *tripartite information* I_3 because it is both observable-independent like the entanglement entropy and can also resolve information transport between small parts of our model system like the OTOCs and hence complements the other two methods. The observable-independence can be a big advantage if the information transport between two extended regions is studied: instead of looking at the correlation functions of many different local observables individually, we can make a comprehensive and generic statement about the buildup of correlations and the flow of information.

The tripartite information has not been extensively studied using advanced numerical methods before and cannot be easily calculated in the standard framework of existing numerical codes, so a new software project was created. Notably, the time evolution method used is a rather naive exact diagonalization of the full Hamiltonian, which was chosen in this case

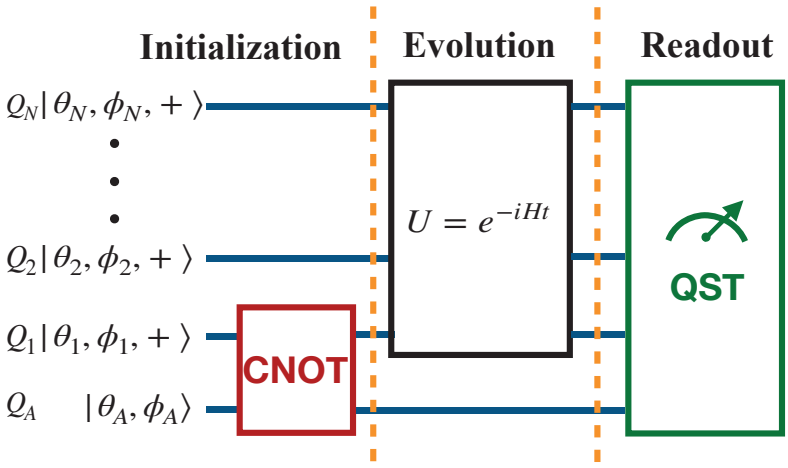

Figure 1.1: Schematic representation of the generic experimental protocol for studying quantum information scrambling by measuring the tripartite information. Taken from Sun, Cui, and Fan [SCF21]. Reprinted with permission from APS.

since it is less error-prone than other methods and turned out to not be a significant bottleneck for the runtime or memory consumption of the overall calculation anyway. The largest system size that can be solved in this way is 16 qubits, which requires a partial trace over a pure state of 32 qubits without symmetry reductions (which corresponds to a state vector of size 64 GiB or, in a naive implementation, a trace over a density matrix with a size too large to store on any computer).

An experimental realization of the tripartite information has also been considered in Sun, Cui, and Fan [SCF21] and is shown schematically in Fig. 1.1. The setup there differs significantly from the one we are considering (which will be explained in more detail in the following chapters) since the time evolution is acting on all but one of the qubits, one of which is maximally entangled with the additional ancilla qubit Q_A. However, using *quantum state tomography*, which is available in experimental setups like trapped ions [Jur+17], superconducting qubits [Xu+18; Yan+19; Chi+22], or nuclear magnetic resonance experiments [Li+19], the tripartite information (called tripartite mutual information (TMI) in the reference) can in principle be experimentally observed.

The tripartite information has also been used in the context of topologically ordered states, where it is called *topological entanglement entropy* [KP06], although we are not aware of any physical connection between this and the scrambling we are considering.

1.2 Overview of the Thesis

In the next chapter, Chapter 2, we will give a quick introduction to classical and quantum information theory and introduce the tripartite information.

We will then explain how the delocalization of quantum information (scrambling) can be studied using the tripartite information in Chapter 3. In particular, the tripartite information allows us to study the transport of information in an observable-independent way.

The numerical implementation will be explained in Chapter 4, where we detail the testing methodology, code and data management, and the implementation of the crucial algorithms. Because the implementation of the partial trace for fermions can be subtle, it is described in particular detail. This chapter is of particular interest to anyone who is looking to calculate the tripartite information numerically.

Regarding the classification of physical systems, the decay of OTOCs has been linked to quantum chaos[RSS15; SS14a; SS14b; RS15; SS15; MSS16] which enables us – via a link between OTOCs and I_3 – to also study quantum chaos. We will see in Chapter 5 that information in a one-dimensional system of spinless fermions travels inside a lightcone that grows linearly in time and will identify a butterfly velocity. Turning on scattering terms in this setup causes the information to be scrambled, which happens both for non-integrable and BETHE integrable [Bet31] cases. We also found similar results for scrambling in momentum space, although we were running into more significant finite-size effects in this case.

On the other hand, *many-body-localized* (MBL) systems that fail to thermalize or thermalize extremely slowly have been linked to a logarithmic growth of the entanglement entropy[ŽPP08; BPM12; SPA13; AES14; HHA21; Hua21]. In Chapter 6, we will see the same logarithmic dependence on time for the tripartite information in the interacting Heisenberg chain. In addition, we find that disorder suppresses scrambling in the system, which allows us to clearly distinguish between multiple important cases: disorder-free systems are expected to thermalize, have a linear information lightcone and are good scramblers, while scrambling is suppressed in strongly disordered systems. These fall into two classes: interacting systems have a logarithmically growing lightcone, while information transport vanishes completely in the non-interacting case. Moreover, we looked at systems that show a transition from paramagnetic to spin-glass in addition to an MBL transition in Section 6.3.

We provide conclusions and an outlook in Chapter 7. Some of the advantages and disad-

vantages of the tripartite information in comparison to other approaches are discussed, and we mention a few of the interesting problems we encountered that are not yet solved but open up interesting new directions for future research.

Chapter 2

Tripartite Information

2.1 Classical Information Theory

Information theory is based on probability theory: the most fundamental random experiment in information theory is the fair coin flip with two outcomes we will call 0 and 1 and associated probabilities $p(0) = p(1) = \frac{1}{2}$.

We now consider the outcome of the random experiment as a piece of information we want to store or transmit, and it turns out that the probabilities will play a major role in how this can be achieved optimally. In digital communications and computer science, information is usually transmitted and stored as a sequence of 0s and 1s, each of which is called a *bit*.

To measure transmitted information, Shannon defined the *information content* $h(x)$ of a specific outcome $x \in A$ of the random experiment as $h(x) = \log\left(\frac{1}{p(x)}\right)$, which follows uniquely – up to the freedom to choose the base of the logarithm arbitrarily – from two requirements: **events with larger probability should have a smaller information content**, where an assured outcome carries no information and the **total information content of two *independent* random experiments should be additive**: $h_{AB}(x, y) = h_A(x) + h_B(y)$. In the case where all probabilities are equal (so $p \equiv \frac{1}{|A|}$), this definition simplifies to an earlier one by Hartley: $h(x) = \log |A|$. [Sha48; Har28]

The *average information content* can be measured with the *Shannon entropy* [Sha48]:

$$H(A) = \langle h(x) \rangle = \sum_{x \in A} p(x) h(x) = -\sum_{x \in A} p(x) \log p(x). \tag{2.1}$$

We can then immediately calculate that the coin flip experiment has an information content

of $\log(2)$. For this reason, we will always use the logarithm to the base 2 in the following so that all our information-theoretic quantities will be measured in terms of the information content of a coin flip: $H(X) = \log_2(2) = 1$. This unit of information is also called *bit*, or sometimes *shannon* to differentiate from the bit used in computer science[1], which is more closely related to HARTLEY's definition.

Since very improbable events are associated with a large information content, that quantity is also sometimes called *surprisal* [Tri59], and the entropy is then, confoundingly, the *expected surprisal*.

Note that if you have N computer science bits (e.g. a file on a computer) the average information content measured in shannon will only equal the number of bits if they are described by an ensemble that assigns each of the 2^N possible configurations the same probability of $\frac{1}{2^N}$, or in other words the bits are maximally random. Any kind of pattern or redundancy will make the storage less efficient as the size becomes larger compared to the contained information. For efficient use of storage *data compression* can then be used to push the average information content closer to the maximum of 1 shannon per bit. We will follow the usual convention in the following and simply call both quantities *bit*.

The next quantity that can be constructed from the SHANNON entropy is the mutual information $I(A : B)$, which describes the relationship between two random experiments A and B that are not necessarily statistically independent and hence must be described by a *joint probability distribution* $p_{AB}(x, y)$, $x \in A$, $y \in B$:

$$I(A : B) = H(A) + H(B) - H(AB), \tag{2.2}$$

where the Shannon entropies $H(A), H(B)$ are calculated from the *marginal probability distributions* $p_A(x) = \sum_{y \in B} p_{AB}(x, y)$ and $p_B(y) = \sum_{x \in B} p_{AB}(x, y)$.

If the two random experiments turn out to be independent after all, the joint probability will factorize $p_{AB}(x, y) = p_A(x)p_B(y)$, and by construction, the Shannon entropy of two independent experiments is additive[2]: $H(A, B) = H(A) + H(B)$, and if we plug this into Eq. 2.2, we see that the mutual information of independent experiments turns out to be zero.

The other extremal case is that of maximally correlated experiments that also have the

[1] The choice of measuring information in multiples of the information content of the coin-flip experiment fixes the arbitrary pre-factor in the definition of the information content or the entropy, which is now uniquely defined.

[2] In fact, the logarithm in the definition of the entropy exists to exactly ensure the additivity property.

same number of degrees of freedom: here no additional information can be gained from doing a second experiment and all entropies are the same: $H(AB) = H(A) = H(B)$ and we see that the mutual information is bounded from above by the entropy: $I(A : B) \leq H(A), H(B)$. The maximal mutual information between two experiments with one bit of entropy is again one bit, and, in this case, the experiments are redundant: because of the perfect correlation, any one of them already predicts the outcome of the other one. In summary, the mutual information is a quantitative measure of the strength of correlations.

We are now ready to introduce the *tripartite information*: it is constructed out of mutual informations and describes the correlations between **three** random experiments:

$$I_3(A : B : C) = I(A : B) + I(A : C) - I(A : BC). \tag{2.3}$$

If we have more than two experiments, correlations become more complicated and separate into different categories. We can study a few prototypical examples:

1. **Mutually maximally correlated experiments**. Since all experiments contain the same information, again all the entropies are identical and the mutual informations are maximal. For one-bit experiments, we then have $I_3 = 1 + 1 - 1 = 1$. A positive tripartite information is called *redundancy* as more than 1/3 of the information can still be extracted even if one of the three measurement outcomes is lost.

2. **Mutually independent experiments** $p_{ABC}(x, y, z) = p_A(x)p_B(y)p_C(z)$. In this case, we again have that all entropies are additive and all mutual informations vanish, as will the tripartite information. Losing 1 bit of measurement outcome will lose 1 bit of total extracted information.

3. **Perfectly delocalized and maximally correlated**. Here the mutual information between any two experiments vanishes, but $I(A : BC)$ is maximal. For one bit experiments, we have $I_3 = 0 + 0 - 1 = -1$. A negative tripartite information is called *synergy* as multiple outcomes must be combined to extract information about the remainder of the system.

Since the last case is the most interesting and unintuitive one we will illustrate it with an example. Consider two independent coin-flip experiments A, B and set the third random variable C to their *exclusive or* ($\oplus$) as prescribed by Table 2.1: $C = A \oplus B$. By construction, we have $I(A : B) = 0$ since their joint probability distribution trivially factorizes (All possible outcomes (A, B) have the same probability of $1/4$).

However, we also see that if we fix the outcome of either A or B while leaving the other un-

A	B	A ⊕ B
0	0	0
0	1	1
1	0	1
1	1	0

Table 2.1: Exclusive or (XOR) logic table

defined then C is also still completely indeterminate, so we also have $I(A:C) = I(B:C) = 0$. Conversely, however, knowing any two of the outcomes predicts the third one with certainty as we have $A = B \oplus C$, $B = A \oplus C$ and $C = A \oplus B$ by the beautiful symmetry of the exclusive or, hence $I(A:BC) = I(B:AC) = I(C:AB) = 1$ and finally:

$$I_3(A:B:C) = \underbrace{I(A:B)}_{0} + \underbrace{I(A:C)}_{0} - \underbrace{I(A:BC)}_{1} = -1. \tag{2.4}$$

In this special case in wich all the information-theoretic quantities are symmetric, we can also immediately deduce that I_3 is **invariant under the permutation of its arguments**. Interestingly, this is always the case, as can be shown with a straightforward calculation using the definition of the mutual information. For this reason, the arguments are often left out and we simply write I_3.

How can we understand the maximally negative tripartite information in the *exclusive or* example? It tells us that **the information in the system is *extensive* or *delocalized*[3]**: We need to perform multiple random experiments to learn anything about the remaining system. In other words: the information is scrambled because knowledge about the outcome of only one random experiment is useless in predicting the outcomes of any single one of the others.

This property of the *exclusive or* operation has important applications in cryptography, which typically rely on the fact that the mutual information between the unencrypted (*plaintext*) and the encrypted data (*ciphertext*) is very low, which makes it difficult to decrypt the message unless a third component – the *secret key* – is also known. Important encryption schemes like Rijndael [DR02] heavily rely on the *exclusive or* operation.

In fact, we can easily model a simple encryption scheme (the *One-Time Pad* [Bel11; Ver26]) using our example: if two parties share a secret key bit A and want to send a message bit B, sending $C = A \oplus B$ over a public channel gives perfect secrecy: anyone who intercepts the encrypted message but does not know the key cannot learn anything since $I(B:C) = 0$.

[3] To prevent confusion with intensive/extensive scaling, we will prefer the term *delocalized*.

This method is perfectly secure, so simple it can be done manually on a piece of paper, and rather impractical, as the encryption key needs to be as long as the message itself and has to be distributed in advance[4]. What is shared with many more advanced (and practical) encryption schemes is that the secrecy of the message only depends on the secrecy of the key, while the implementation details can be made public (KERCKHOFF's Principle [Ker83]), which yields a similar structure of *synergy* as in our example. For these, two of the three parties A, B, C are the plaintext message and the secret key as before, while the third party consists of information like the encryption scheme and the encrypted message that can be made public without endangering the security of the method.

2.2 Quantum Information Theory

In the quantum version of information theory we will use the same definitions for the mutual information and the tripartite information as before, but instead, replace the SHANNON *entropy* that depends on a classical probability distribution with the VON-NEUMANN *entropy* that depends on the density matrix of a quantum system. Although quantum information theory was more recently developed from the older classical version, the VON-NEUMANN entropy was already used to study problems in statistical physics [vNeu32] (which also features the related GIBBS entropy) before either of the theories was founded and also predates the SHANNON entropy [5].

For a density matrix $\rho = \sum_j p_j \left|\psi_j\right\rangle \left\langle\psi_j\right|$ the VON-NEUMANN entropy is defined as follows:

$$S = -\operatorname{Tr} \rho \log_2 \rho, \tag{2.5}$$

where the $\left|\psi_j\right\rangle$ are generic pure states, the p_j are (non-negative) probabilities that sum up to one and the density matrix has the usual properties:

$$\begin{aligned} \rho &= \rho^\dagger \quad \text{Hermitian,} \\ \rho &\geq 0 \quad \text{Semi-definite,} \\ \operatorname{Tr} \rho &= 1 \quad \text{Trace one.} \end{aligned}$$

From these properties it follows that there is a spectral decomposition $\rho = \sum_i \lambda_i \left|\phi_i\right\rangle \left\langle\phi_i\right|$ into the eigenvalues λ_i and associated orthogonal eigenvectors $\left|\phi_i\right\rangle$ with $\sum_i \lambda_i = 1, \lambda_i \geq 0$

[4] The method was, however, used by secret agents and spies [Kah96].

[5] Apparently, von Neumann recommended to Shannon that he should call his quantity entropy (instead of *information* or *uncertainty*) because it had been used under that name in statistical physics and also nobody really understood entropy and so he would always have the advantage in a debate [TM71].

which then provides the link to the SHANNON entropy:

$$S(\rho) = -\operatorname{Tr}\rho\log_2\rho = -\sum_{ij}\left|\langle\phi_i|\phi_j\rangle\right|^2\lambda_j\log_2\lambda_j = -\sum_i\lambda_i\log_2\lambda_i = H(\{\lambda_i\}).$$

The coin flip random experiment from classical theory is replaced by a quantum mechanical two-state system (*qubit*), which can be thought of as a spin-1/2 degree of freedom and is described by a ray in the simple two-dimensional Hilbert space $H = \mathbb{C}^2$. The maximally mixed state of this system is described by $\rho = \frac{1}{2}\mathbb{1}_{2\times 2}$ with VON-NEUMANN entropy equal to one.

Despite the many analogies, the quantum version is fundamentally different when it comes to correlations. For this, we need the quantum analogue of the joint and marginal probability distributions: The density matrix of a subsystem (corresponding to the marginal probability) will be calculated by a partial trace of the total density matrix (corresponding to the joint probability) over the remainder of the system, e.g. $\rho_A = \operatorname{Tr}_B\rho_{AB}$. This is fundamentally different from the classical version $p(x) = \sum_{y\in B}p(x,y)$ because it depends on the entire matrix and not just the eigenvalues or probabilities.

A striking example of this difference is a maximally entangled bipartite state (e.g. a spin singlet):

$$|\Psi\rangle_{AB} = \frac{1}{\sqrt{2}}\left(|0\rangle_A\otimes|1\rangle_B - |1\rangle_A\otimes|0\rangle_B\right) \tag{2.6}$$

For a pure state $|\Psi\rangle$ the spectral decomposition is trivial: $\rho = 1\,|\Psi\rangle\langle\Psi|$ and $S_{AB} = -1\log_2 1 = 0$. So there is no uncertainty about the state of the total system. However, if we perform the partial trace we see that the two subsystems are in a maximally mixed state: $\rho_A = \rho_B = \frac{1}{2}\left(|0\rangle\langle 0| + |1\rangle\langle 1|\right)$ and $S_A = S_B = -\frac{1}{2}\log_2\frac{1}{2} - \frac{1}{2}\log_2\frac{1}{2} = 1$. So we see that the mutual information in this case is:

$$I(A,B) = S_A + S_B - S_{AC} = 1 + 1 - 0 = 2. \tag{2.7}$$

This violates the classical bound $I(A,B) \leq \max(S_A, S_B)$ by a factor of 2: **maximally entangled states are more strongly correlated than any classical state**. This result is also consistent with the fact that they violate the BELL inequality [Bel64], which is a result that uses hidden classical variables and hence would also admit a description using classical information theory.

We see from our example that $S_A = S_B$. In fact, this is true more generally: If the entire system is in a pure state, i.e. $S_{AB} = 0$, then we can perform a SCHMIDT decomposition

(also known as *Singular Value Decomposition*) and see that the eigenvalues of the reduced density matrices ρ_A and ρ_B and hence their entropies are necessarily the same [NC00]:

$$
\begin{aligned}
|\Psi\rangle_{AB} &= \sum_{i=1}^{s} \sqrt{\lambda_i}\, |a_i\rangle_A \otimes |\beta_i\rangle_B \quad \text{Schmidt decomposition} \\
\rho_A &= \mathrm{Tr}_B\, |\Psi\rangle_{AB} \langle\Psi| = \sum_{i=1}^{s} \lambda_i\, |a_i\rangle_A \langle a_i| \\
\rho_B &= \mathrm{Tr}_A\, |\Psi\rangle_{AB} \langle\Psi| = \sum_{i=1}^{s} \lambda_i\, |\beta_i\rangle_B \langle \beta_i| \\
S_A &= H(\{\lambda_i\}) = S_B
\end{aligned}
$$

We are now ready to look at the first simple example of a multipartite quantum system: the tripartite information of a pure state $|\Psi\rangle_{ABC}$, where we again have, by the purity of the total system and the Schmidt decomposition, that the entropies of complementary subsystems are identical, e.g. $S_A = S_{BC}$, etc. Using this we quickly see that the tripartite information vanishes:

$$
\begin{aligned}
I_3 &= I(A:B) + I(A:C) - I(A:BC) \\
&= (S_A + S_B - S_{AB}) + (S_A + S_C - S_{AC}) - (S_A + S_{BC} - S_{ABC}) \\
&= S_A + S_B + S_C - (S_{AB} + S_{BC} + S_{AC}) + S_{ABC} \\
&= S_A + S_B + S_C - (S_C + S_A + S_B) + S_{ABC} \\
&= S_{ABC} = 0.
\end{aligned}
$$

This shows us that if we are considering pure state entanglement, **three is not enough**: the tripartite information is a measure of *quartipartite entanglement*. We need the state of the tripartite system ABC to be mixed, i.e. $\rho_{ABC}^2 \neq \rho_{ABC}$ for the tripartite information to be non-zero. We can, however, introduce the purification $|\Psi\rangle_{ABCD}$ by embedding the density matrix in a larger Hilbert space, with the prescription $\rho_{ABC} = \mathrm{Tr}_D\, |\Psi\rangle_{ABCD}$ [NC00]. In the following, we will only talk about total quartipartite systems $ABCD$ that are in a pure state, which can then have non-vanishing tripartite information if none of its partitions are in a pure state.

Interestingly, it is irrelevant which three of the four partitions we pick to calculate the tripartite information. We can trace out any single one of them before the tripartite information of the remaining three subsystems is calculated (using either ρ_{ABC}, ρ_{ABD}, ρ_{ACD} or ρ_{BCD} depending on if we traced out D, C, B or A first), so we have $I_3(A:B:C) = I_3(A:B:D) = I_3(A:C:D) = I_3(B:C:D)$ for these systems in addition to the per-

mutation symmetry of the arguments, so we will keep writing I_3 without specifying arguments[6].

2.3 Entropic Inequalities

We will need some important inequalities of the SHANNON and VON-NEUMANN entropies and for that purpose first switch back to classical theory and define the *conditional probability* $p_{A|B}(x|y), x \in A, y \in B$, that is the probability of outcome x of the random experiment A given that we already know the outcome of B is y [GW14; MKP03]:

$$p_{A|B}(x|y) = \frac{p_{AB}(x,y)}{p_B(y)}. \tag{2.8}$$

The conditional probability defines an *information content* in the usual way $h(x) = -\log_2 p(x)$, which yields the *conditional entropy* by averaging over ensembles A and B:

$$H(A|B) = \sum_{x,y \in A,B} p_{AB}(x,y) h_{A|B}(x|y) = -\sum_{x,y \in A,B} p_{AB}(x,y) \log_2 p_{A|B}(x|y). \tag{2.9}$$

We note that although the information content now depends on the conditional entropy, the average always has to be unbiased and needs to be weighted by the joint entropy, which is **not** conditioned on B.

The conditional entropy is related to the previously defined ones by the *Chain rule of information content* [MKP03]:

$$H(AB) = H(A|B) + H(B) = H(B|A) + H(A). \tag{2.10}$$

This makes sense: the information content of the joint ensemble AB can be decomposed into performing e.g. random experiment A first and acquiring information measured by its entropy $H(A)$ and then performing random experiment B and learning the remaining information given by $H(B|A)$, which will be a quantity that can be as large as the unconditional $H(B)$ for independent experiments or vanish for maximally correlated experiments.

We can write the mutual information also in terms of the conditional entropy using the chain rule:

$$I(A:B) = H(A) + H(B) - H(AB) = H(A) - H(A|B). \tag{2.11}$$

[6]For example to replace $I_3(A:B:C)$ with $I_3(B:C:D)$ we just rewrite $S_A \to S_{BCD}, S_{AB} \to S_{CD}$ etc.

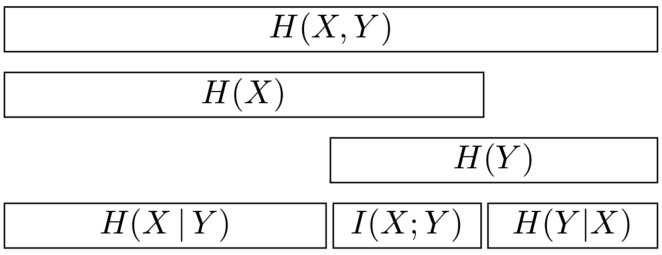

Figure 2.1: Comparison of different information-theoretic quantities. Source: MacKay, Kay, and Press [MKP03].

Or, more interestingly, we can introduce a third random experiment C and define the *conditional mutual information* CMI [MKP03], where now all quantities are conditioned on C:

$$I(A:B|C) = H(A|C) + H(B|C) - H(AB|C) = H(A|C) - H(A|BC). \tag{2.12}$$

It is not that difficult to show that the conditional mutual information is non-negative, as we can write it in the following form [Wil17]:

$$I(A:B|C) = \sum_{z\in C} p_C(z) I(X:Y|C=z). \tag{2.13}$$

For fixed z the second factor in the sum is a mutual information which is always non-negative (cf. Fig. 2.1), as is the probability, so we get the non-negativity of the CMI:

$$I(A:B|C) \geq 0. \tag{2.14}$$

If we write out the CMI using $H(A|B) = H(AB) - H(B)$:

$$I(A:B|C) = H(AC) - H(C) - (H(ABC) - H(BC))$$

we see that the non-negativity of the CMI is equivalent to the following important statement:

$$H(AC) + H(BC) \geq H(ABC) + H(C) \quad \textbf{Strong subadditivity}. \tag{2.15}$$

We are now almost ready to compare and contrast inequalities relating to classical and quantum information theories. We run into one problem right at the start: there is no quantum version of the conditional probability $p_{A|B}$, and there are multiple potential definitions of the conditional quantum entropy that are incompatible with each other. We will define it here using the classical chain rule of information content (Eq. 2.10) we already

established:

$$S(A|B) = S(AB) - S(B) \quad \text{Conditional Quantum Entropy – } \textbf{Definition} \tag{2.16}$$

By construction (Eq. 2.9), the classical conditional entropy is non-negative:

$$H(A|B) = H(AB) - H(B) \geq 0 \tag{2.17}$$

This seems to be rather obvious since adding a second random experiment cannot decrease the uncertainty and so $H(B) \leq H(AB)$. It is also patently untrue for its quantum version: we have seen in our first example of a maximally entangled state (Eq. 2.6) that the joint entropy S_{AB} can vanish even if the marginal entropies S_A, S_B are maximal. **The conditional quantum entropy can be negative.** Instead, we get the Araki-Lieb triangle inequality [Wil17]:

$$|S_A - S_B| \leq S_{AB} \tag{2.18}$$

What holds true in both worlds, however, are **Subadditivity of Entropy** [Wil17]:

$$H(AB) \leq H(A) + H(B) \qquad S_{AB} \leq S_A + S_B \tag{2.19}$$

and also **Strong Subaddivitiy of Entropy** which we saw above[7] [Wil17]:

$$H(ABC) + H(C) \leq H(AC) + H(BC) \qquad S_{ABC} + S_C \leq S_{AC} + S_{BC} \tag{2.20}$$

As in the classical case it is still equivalent to the non-negativity of the conditional mutual information: $I(A:B|C) \geq 0$.

We want to use strong subadditivity to better understand the tripartite information, and hence rewrite it in terms of the conditional mutual information:

$$\begin{aligned} I_3 &= S_A + S_B + S_C - (S_{AB} + S_{BC} + S_{AC}) + S_{ABC} && (2.21)\\ &= \underbrace{(S_A + S_B - S_{AB})}_{I(A:B)} + \underbrace{(S_{ABC} + S_C - S_{AC} + S_{BC})}_{-I(A:B|C)} && (2.22)\\ &= I(A:B) - I(A:B|C) && (2.23) \end{aligned}$$

Since the last term (including the minus sign) is non-positive, we find the following upper

[7] The quantum version of this statement is non-trivial to show, and much of quantum information theory rests on its shoulders [Wil17].

bound for the tripartite information:

$$I_3 \leq I(A:B) \tag{2.24}$$

This meshes well with our earlier examples in Section 2.1: the mutual information between two individual parts measures the redundancy of information, which is also measured by a positive value of the tripartite information as we saw in our first example of a mutually maximally correlated experiment. If, on the other hand, the information is completely delocalized, the upper bound vanishes and indeed the tripartite information will become negative, as we saw in our third example of a perfectly delocalized and maximally correlated experiment.

2.4 Rényi Entropies

The Shannon and von-Neumann entropies can be generalized to the family of the Rényi entropies that are parametrized by a real parameter $\alpha \in [0, \infty]$ [Rén61]. The definition of the *quantum Rényi entropy of order* α is the following:

$$S^{(\alpha)} = \frac{1}{1-\alpha} \log_2 \operatorname{Tr} \rho^\alpha. \tag{2.25}$$

The two extremal cases are called the *max-entropy* ($\alpha \to 0$), that provides a natural upper bound for the entire family:

$$S^{\max} = \lim_{\alpha \to 0} S^{(\alpha)} = \log_2 \operatorname{Tr} \mathbb{1}_{\dim \mathcal{H} \times \dim \mathcal{H}} = \log_2 \dim \mathcal{H}, \tag{2.26}$$

and the *min-entropy* ($\alpha \to \infty$), which can still be calculated if, e.g., only the largest eigenvalue of ρ is accessible perturbatively:

$$S^{\min} = \lim_{\alpha \to \infty} S^{(\alpha)} = -\lim_{\alpha \to \infty} \frac{1}{\alpha} \log_2 \sum_i \lambda_i^\alpha = -\lim_{\alpha \to \infty} \frac{1}{\alpha} \log_2 \lambda_{\max}^\alpha = -\log_2 \lambda_{\max}, \tag{2.27}$$

where $\lambda_{\max}$ is the largest of the eigenvalues $\{\lambda_i\}$ of the density matrix.

The family is ordered inversely with respect to the parameter α, with the min-entropy having the smallest, and the max-entropy the largest value:

$$\alpha > \beta \Rightarrow S^{(\alpha)} \leq S^{(\beta)}. \tag{2.28}$$

We are mostly interested in two special cases: for $\alpha \to 1$ we recover the VON-NEUMANN entropy:

$$\begin{aligned}
\lim_{\alpha\to 1} S^{(\alpha)} &= \lim_{\alpha\to 1} \frac{1}{1-\alpha} \log_2 \operatorname{Tr} \rho^\alpha \\
&= \lim_{\alpha\to 1} -\frac{\mathrm{d}}{\mathrm{d}\alpha} \log_2 \operatorname{Tr} \rho^\alpha \quad \text{L'Hôpital's rule} \\
&= \lim_{\alpha\to 1} -\frac{1}{\operatorname{Tr} \rho_i^\alpha} \operatorname{Tr} \frac{\mathrm{d}}{\mathrm{d}\alpha} e^{\alpha \log \rho} \\
&= -\operatorname{Tr} \rho \log \rho = S
\end{aligned}$$

And for $\alpha \to 2$ we find the *collision entropy*:

$$S^{(2)} = \frac{1}{1-2} \log_2 \operatorname{Tr} \rho^2 = -\log_2 \operatorname{Tr} \rho^2. \tag{2.29}$$

We will (naively) replace the VON-NEUMANN entropy with the RÉNYI entropies to define composite properties like the mutual information and the tripartite information:

$$I^{(\alpha)}(A:B) \stackrel{\text{def}}{=} S_A^{(\alpha)} + S_B^{(\alpha)} - S_{AB}^{(\alpha)} \tag{2.30}$$

$$I_3^{(\alpha)} \stackrel{\text{def}}{=} I^{(\alpha)}(A:B) + I^{(\alpha)}(A:C) - I^{(\alpha)}(A:BC) \tag{2.31}$$

The collision entropy turns out to have some advantages because it is easier to calculate and measure and the collision tripartite information can be linked to the decay of two-point correlation functions, as we will see in the next chapter. The members of the RÉNYI family, except of course for the VON-NEUMANN entropy, are, however, not ideal for quantum information theory, as they in general fail to satisfy important properties like strong subadditivity unless a less naive definition of the conditional mutual information is chosen that fulfils $I^{(\alpha)}(A:B|C) \geq 0$ [BSW15; AGS12].

Chapter 3

Scrambling

3.1 Origins of Scrambling

The concept of scrambling originates from the quantum information theory of black holes, in particular, how they process infalling bits of information. As was already shown in Page [Pag93] and Page [Pag95], a black hole can become entangled with its environment via the HAWKING radiation it emits as it evaporates. The HAWKING radiation is the theorized emission of black body radiation from the vicinity of a black hole's event horizon that causes its slow evaporation [Haw74; Haw75]. More precisely, although the first half of the quanta the black hole emits over its lifetime does not have any structure and the radiation subsystem is described by a thermal state, the quanta emitted later can be maximally entangled with the previous ones so that the black hole gradually decreases its entanglement with the outside and the radiation subsystem can be in a pure state when the black hole has completely evaporated.

We are considering a more recent concept of scrambling as illustrated by the HAYDEN-PRESKILL gedankenexperiment shown in Fig. 3.1 [HP07]. In this setup, instead of looking solely at the evaporation of a black hole, there is also Alice's secret diary A that is falling into the black hole at some point during its lifetime. The adversary Bob, who wants to read the secret diary, knows about the internal dynamics of the black hole (the unitary operator U) and is also measuring all the Hawking radiation that is being sent by it (controls subsystem D). Similar to the previous case, if half the information quanta have already left the black hole, then the secret information is re-emitted very quickly, in the sense that Bob can, in theory, reconstruct any qubit thrown in by Alice by waiting for an additional

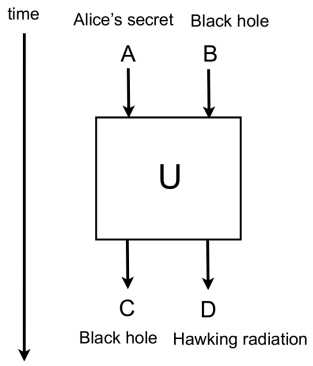

Figure 3.1: The Hayden-Preskill gedankenexperiment. Taken from Hosur et al. [Hos+16].

qubit to be emitted and performing a unitary transformation and measurement on D. This measurement yields the same result as if it had been performed on one of the qubits in Alice's secret A. Note that this experiment is not necessarily practical since finding and performing the correct transformation to reconstruct the information might be extremely difficult in general, in addition to the already daunting task of capturing and storing all the emitted radiation quanta.

Interestingly, this means that if the black hole has already reached the second half of its life, the infalling information is re-emitted immediately because the internal degrees of freedom are maximally entangled with the subsystem D in Bob's control, hence the term "mirror" in the title of Hayden and Preskill [HP07]. This, in turn, requires that the information in A has been very rapidly delocalized across the internal degrees of freedom of the black hole, in other words, black holes are fast scramblers. They, in fact, satisfy the bound found in Maldacena, Shenker, and Stanford [MSS16] on the scrambling speed in quantum theory, so they are the fastest scramblers of quantum information.

3.2 Tripartite Information of Time Evolution

We are not interested in black holes, at least not for the purposes of this thesis, but instead want to study the scrambling of quantum information in typical model systems from condensed matter theory due to unitary time evolution. We are applying the same methodology as can be found in Hosur et al. [Hos+16], which means that the setup looks similar to Fig. 3.1, where now the initial state of the many-body quantum system is described by the system AB containing L qubits, and the time-evolved system is described by CD (naturally also containing L qubits). To study the scrambling dynamics, we are using the tripartite

information of the system $ABCD$, as introduced in Chapter 2.

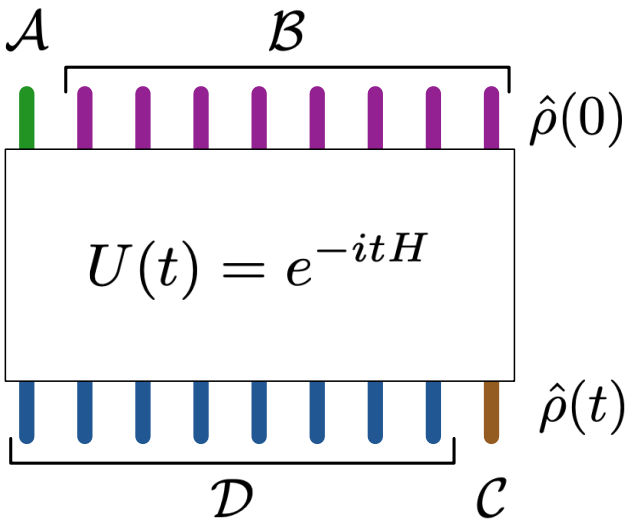

Figure 3.2: A quantum channel describing the time evolution of the quantum system and the subsystems used for calculating the tripartite information. Fig. 3 from Bölter and Kehrein [BK22b].

The natural HILBERT space structure is to describe the state of the l^{th} qubit as a density operator ρ_l on a two-dimensional HILBERT space h_l and construct the total system state as the KRONECKER product of the density matrices $\rho = \otimes_{l=1}^{L} \rho_l$, which now operate on the 2^L-dimensional tensor product $\mathcal{H} = \otimes_{l=1}^{L} h_l$.

To study the flow of information, if the system is not given any time for scrambling (so the time-evolution operator is just the identity operator), a measurement in a subsystem of CD must yield the same information as that in the equivalent subsystem of AB, so they must initially be maximally entangled (here $\{|\nu\rangle\}$ is an orthonormal basis of the HILBERT spaces $\mathcal{H}_{AB} \cong \mathcal{H}_{CD}$):

$$|\psi\rangle = \frac{1}{\sqrt{2^L}} \sum_{|\nu\rangle} |\nu\rangle_{AB} \otimes |\nu\rangle_{CD} \,. \tag{3.1}$$

This state can be understood as a collection of maximally entangled BELL pairs, where the n-th qubit of the system AB and the n-th qubit of the system CD form one pair together [NC00].

It is also the dual of the identity operator $\mathbb{1} = \sum_{|\nu\rangle} |\nu\rangle_{AB} \otimes \langle\nu|_{CD}$ under the so-called *channel-state duality* [NC00], which maps the operation of the channel (in this case: the identity operation) to a pure state in a doubled HILBERT space, up to normalization. We will continue to use states in the doubled HILBERT space $ABCD$ to describe the unitary channels that implement the time evolution from the physical HILBERT spaces $\mathcal{H}_{AB}$ to $\mathcal{H}_{CD}$. The state $|\psi\rangle$ can also be seen as the *thermofield double state* $|\text{TFD}\rangle_\beta$ at infinite temperature (with the diagonalization of H as usual: $H|n\rangle = E_n|n\rangle$ and the partition sum $Z = \text{Tr}\, e^{-\beta H}$) [Hos+16]:

$$|\text{TFD}\rangle_\beta = \frac{1}{\sqrt{Z}} \sum_n e^{-\beta E_n/2} |n\rangle \otimes |n\rangle \in \mathcal{H}_{AB} \otimes \mathcal{H}_{CD} \tag{3.2}$$

The thermofield double state is a purification of the thermal state $\rho = \frac{1}{Z} e^{-\beta H} \equiv \text{Tr}_{CD} |\text{TFD}\rangle_\beta \langle\text{TFD}|$. Since we already found out on information-theoretic grounds that we want to have the form given in Eq. 3.1 at the initial time we will drop the added complication of specifying the temperature and will set $\beta = 0$ for now.

If we now allow the system to evolve (and scramble information) for a time t, we have to model this by evolving the system CD with the time-evolution operator $U(t) = e^{-iHt}$ and we will get the most general form of the state we will be studying [Hos+16]:

$$|U(t)\rangle_{\beta=0} = \frac{1}{\sqrt{2^L}} \sum_n e^{-iE_n t} |n\rangle \otimes |n\rangle \in \mathcal{H} \otimes \mathcal{H} \tag{3.3}$$

Given a state of this form, we can calculate the tripartite information I_3 as described in Chapter 2.

Calculating I_3 for generic cases is quite difficult and we will usually rely on numerical methods to achieve this, there are, however, a few simpler cases that can be calculated analytically. Because we initially have all the qubits form BELL pairs between the two systems AB and CD, we know that those two systems have to be maximally mixed, $\rho_{AB} = \rho_{CD} \propto \mathbb{1}$ with maximal entropy S given by the logarithm of the HILBERT space dimension (the max-entropy if we are thinking about the Rényi entropies from Section 2.4), which in this case is just the number of qubits L in the system ($\log_2 \dim \mathcal{H} = \log_2 2^L = L$). This also applies to their subsystems A, B, C, and D. This will not change under unitary dynamics, so all of these entropies only depend on the respective HILBERT space dimensions and are time-independent. More complicated, however, are the two remaining subsystems, AC and AD, whose entropies are required to calculate I_3. At the initial time they either contain entire BELL pairs, which do not contribute to the subsystem entropy as they are in a pure state,

or qubits that are in a Bell pair with another qubit outside the subsystem and hence are maximally mixed and contribute one bit of entropy. For $t > 0$ the situation becomes non-trivial, and we will in general use numerical methods to calculate $S_{AC}(t)$ and $S_{AD}(t)$.

Because the entropies (measured in bit) are equal to the number of qubits for the maximally mixed subsystems, we have $S_A + S_B = S_C + S_D = S_{AB} = S_{AD} = L$ and the tripartite information simplifies accordingly:

$$\begin{aligned} I_3(t) &= I(A:C) + I(A:D) - I(A:CD) \\ &= S_A + S_B + S_C + S_D - (S_{AB} + S_{AC}(t) + S_{AD}(t)) \\ &= L - (S_{AC}(t) + S_{AD}(t)) \end{aligned} \tag{3.4}$$

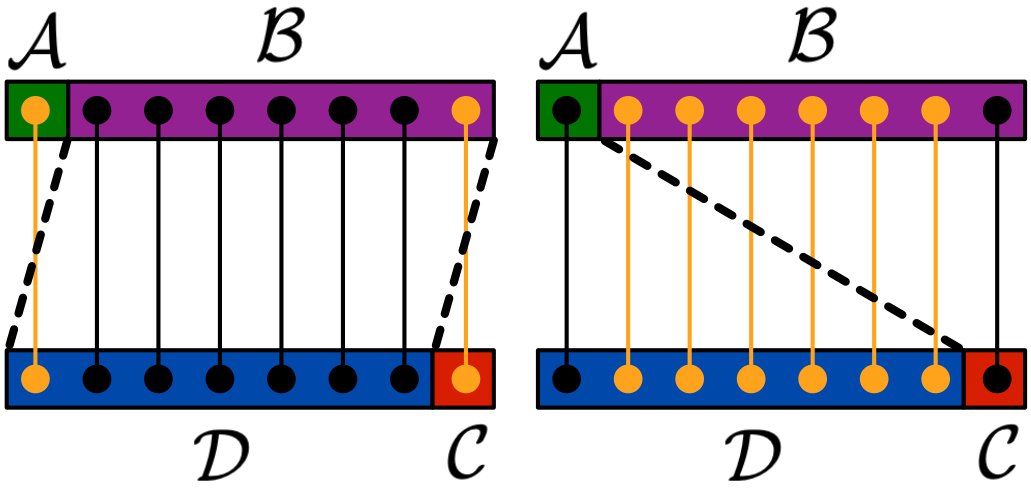

(a) Subsystem AC **(b)** Subsystem AD

Figure 3.3: Schematic illustration of the entropies S_{AC} and S_{AD} at $t = 0$ where the system is a product state of Bell pairs. The qubits that are separated from their partner by the partitioning are contributing one bit of entropy. a) The subsystem AC is connected with the remainder by two pairs and $S_{AC} = 2$ b) The subsystem AD is connected with the remainder by $L - 2$ pairs and the entropy is $L - 2$.

Additionally, at $t = 0$ the systems AB and CD are connected by L Bell pairs, where we can count the number of pairs that get separated by the bipartition to calculate the entropy (see Fig. 3.3): all of the qubits in A can only connect to either C or D, so all of the ones that connect to C will add one bit to S_{AD} and those that connect to D will add one bit to S_{AC}. Similarly, all of the pairs that connect to B will be separated by either bipartition, and those that connect to C will add one bit of entropy to S_{AC} (because $S_{AC} \equiv S_{BD}$) and those that

connect to D will add one bit of entropy to S_{AD} (because $S_{AD} \equiv S_{BC}$). If we add up all of the contributions, we see that each qubit in either A or B adds one bit of entropy to the sum of the two entropies, and we have $S_{AC} + S_{AD} = L$.

Quite beautifully, we see that for all qubit systems the tripartite information initially vanishes:

$$I_3(0) = L - (S_{AC}(0) + S_{AD}(0)) = 0. \tag{3.5}$$

Importantly, if there are additional constraints on the system that limit the accessible states such that the effective HILBERT space dimension is not 2^ℓ for subsystems of size ℓ, there might be an offset to the initial value of the tripartite information. Examples we encountered included a restriction to a fixed number of particles in fermionic/bosonic systems or a restriction to a fixed magnetization in spin chains, in which case the initial value can still be calculated analytically with combinatorics but becomes model-dependent.

3.3 Haar Scrambling

To diagnose scrambling we need to compare the behaviour of the tripartite information to some reference scrambler. We follow Hosur et al. [Hos+16] again and compare the tripartite information of unitary time evolution using a Hamiltonian with that of a random unitary operator, which we calculate by taking samples from the unitary group according to the HAAR measure, the numerical method for this can be found in Mezzadri [Mez07].

For each sample of the unitary group, the tripartite information is calculated as in the previous section, with $U(t)$ replaced by the sample, and then the results are averaged. For larger systems, there is strong self-averaging, so very few samples are required as they all already agree to many decimal places.

Importantly, OSKAR SCHNAACK showed in his Master's thesis that the random unitaries should respect the same symmetries as that of the Hamiltonian so that they have the same block structure in the mutual eigenbasis with the symmetry operators as the Hamiltonian [Sch17; Sch+19].

Exemplarily, we can look at the Hamiltonian of the spinless fermion system, which we will be studying in more detail in Chapter 5, with a system size of three lattice sites and parameters set to 1 ($L = 3, \lambda = 1, V = 1$). We see four different (interleaved) blocks corresponding to symmetry sectors of particle numbers 0, 1, 2, and 3 (marked red, blue, orange, and green respectively).

$$\begin{pmatrix} 0 & 0 & 0 & 0 & 0 & 0 & 0 & 0 \\ 0 & 0 & -1 & 0 & -1 & 0 & 0 & 0 \\ 0 & -1 & 0 & 0 & -1 & 0 & 0 & 0 \\ 0 & 0 & 0 & 1 & 0 & -1 & 1 & 0 \\ 0 & -1 & -1 & 0 & 0 & 0 & 0 & 0 \\ 0 & 0 & 0 & -1 & 0 & 1 & -1 & 0 \\ 0 & 0 & 0 & 1 & 0 & -1 & -1 & 0 \\ 0 & 0 & 0 & 0 & 0 & 0 & 0 & 3 \end{pmatrix}$$

A matrix plot of both this Hamiltonian and a generic random unitary operator is shown in Fig. 3.4. If we compare this to the time evolution operator e^{-itH} in Fig. 3.5 we can again see the same block structure (in this case due to the conservation of particle number) as in the Hamiltonian. If we instead fill each of these blocks with a smaller random unitary operator, we get the symmetry-adapted random unitaries as shown in Fig. 3.6. If the mutual eigenbasis of the symmetry operators differs from the computational basis, we first construct the random unitary in the mutual eigenbasis, in which the block structure is manifest, and rotate it into the computational basis.

If the correct Haar-averaged value of the tripartite information I_3^{Haar} is known, the results can then be normalized to $I_3(t)/I_3^{\text{Haar}}$. If this value converges to unity, we say that the system behaves like a HAAR scrambler.

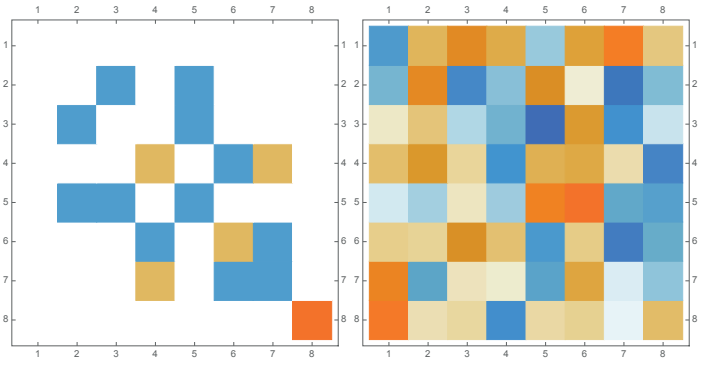

(a) Hamiltonian **(b)** Random Unitary Operator

Figure 3.4: The structure of the Hamiltonian vs a generic random sample from the unitary group

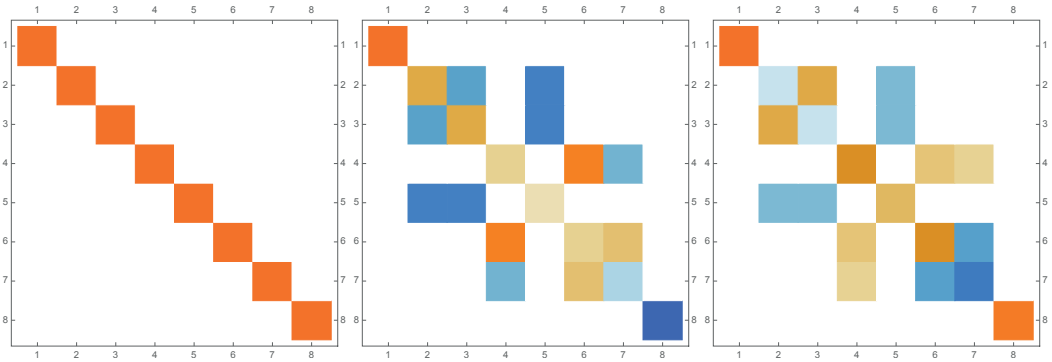

(a) $t = 0$ **(b)** $t = 1$ **(c)** $t = 2$

Figure 3.5: Time evolution operators e^{-itH}

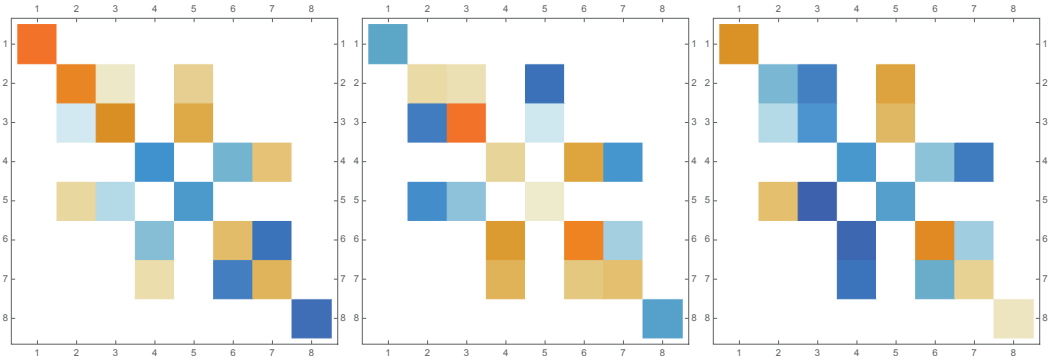

(a) Random Sample 1 **(b)** Random Sample 2 **(c)** Random Sample 3

Figure 3.6: Symmetry adapted random unitary operators

3.4 Link to Out-of-Time-Order Correlation Functions

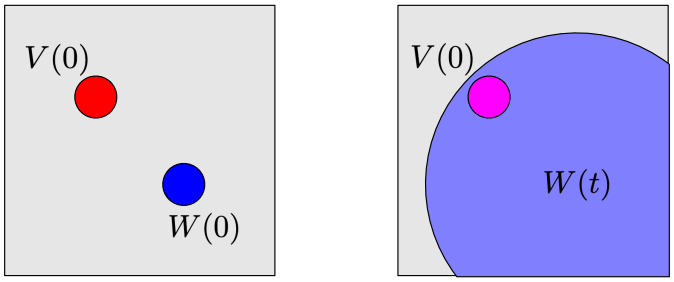

Figure 3.7: Spreading of initially local operator under time evolution. Fig. 1 from Bölter and Kehrein [BK22b].

Another approach to studying scrambling is the use of *Out-of-Time-Order correlation functions* (OTOCs). We consider two observables V and W, that are initially localized on spatially separated parts of the system, which also causes them to commute $[V, W] = 0$. If we now look at the time evolution of the operator W as described by the HEISENBERG equation of motion [SN21]:

$$\frac{\mathrm{d}W(t)}{\mathrm{d}t} = \frac{1}{i}[W(t), H], \tag{3.6}$$

we see that it could eventually spread over the entire system (also see Fig. 3.7):

$$W(t) = W + it[H, W] + \frac{(it)^2}{2}[H, [H, W]] + ... \tag{3.7}$$

In a chaotic system, the absolute value of the commutator with the local operator V that vanishes originally should grow to a large value in the long-time limit (called the quantum butterfly effect) [MSS16]:

$$\left\langle [W(t), V]^2 \right\rangle_\beta \to 2 \left\langle WW \right\rangle_\beta \left\langle VV \right\rangle_\beta . \tag{3.8}$$

Interestingly, if we replace the commutator with a POISSON bracket in a semi-classical analysis we find the exponential separation in phase space that is a hallmark feature of classical chaos:

$$\hbar^2 \{q(t), p\}^2 = \hbar^2 \left(\frac{\delta q(t)}{\delta q(0)} \right)^2 \propto \hbar^2 e^{2\lambda t}, \tag{3.9}$$

where λ is a LYAPUNOV exponent of the system [SJ05].

The commutator Eq. 3.8 of observables separated in time is also closely linked to the out-of-time-order correlations function (OTOC) $\left\langle W(t)VW(t)V \right\rangle_\beta$, and their decay can be used to

diagnose the onset of non-commutativity of the operators under the time evolution [MSS16].

As shown in Hosur et al. [Hos+16] (see also Schnaack [Sch17]) the butterfly effect as diagnosed by OTOCs implies scrambling as diagnosed by tripartite information calculated using the quantum collision entropy $I_3^{(2)}$ (see Section 2.4) in spin-$\frac{1}{2}$ systems. In particular, if ϵ_{min} is the minimum value for the average of the OTOCs and $(-I_3^{(2)})_{\text{max}}$ is the maximal value of $-I_3^{(2)}$ then it was shown that:

$$|\langle W(t)VW(t)V\rangle| = \epsilon \Rightarrow -I_3^{(2)} \geq (-I_3^{(2)})_{\text{max}} - 2\log_2 \frac{\epsilon}{\epsilon_{\text{min}}}. \tag{3.10}$$

In other words, a decay of all OTOCs – associated with the quantum butterfly effect – implies that the tripartite information I_3 reaches a large negative value – associated with scrambling [Hos+16].

Chapter 4

Numerical Implementation

4.1 Overview

A software project was created from scratch to calculate the tripartite information in many different physical situations numerically. We also performed analytical calculations in parallel that only yielded limited results, which will be discussed in Section 5.3.

The primary goals of the numerical implementation are:

1. Thorough internal testing of the plausibility and consistency of results
2. Results exact up to machine precision
3. Flexibility to study different model systems and system partitionings
4. Higher performance than existing implementations

At the start of the project, we were not aware of any published numerical results for the tripartite information in condensed matter models, which makes it challenging to verify the correctness of the results. For this reason, particular care was taken when testing and only numerically exact methods were used, which limits the performance and the accessible system sizes. It will be interesting to develop further methods in the future for which our numerically exact results can serve as verification data. Also, no multi-threading was used since this can potentially introduce numerous bugs, and no meaningful difference to the performance was expected as long as the resulting single-threaded program is executed multiple times in parallel with different parameters to spread the load over all available cores.

When comparing to previous work, namely the master's project by Oskar Schnaack [Sch17], the goal was to extend the calculation to support a more diverse set of model systems and system partitionings and also larger system sizes. We did not use any pre-existing code from that project because an independent implementation was required to be able to test the correctness of both codes in lieu of existing numerical or analytical comparison data. We also compared with results that were produced by Sebastian Paeckel using a DMRG implementation [Pae+19] when working on Schnaack et al. [Sch+19], as will be explained in more detail in Chapter 5.

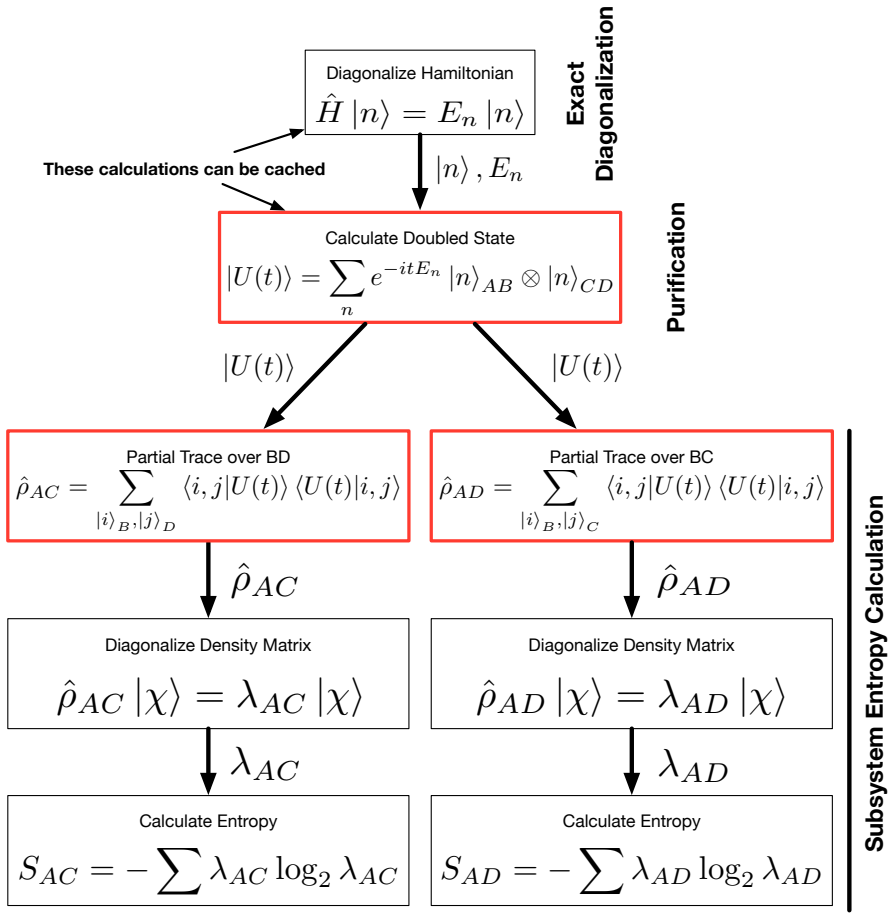

Figure 4.1: Schematic overview of the important steps in the numerical calculation of the tripartite information. The performance bottlenecks of the code – that take up the majority of the execution time – are highlighted in red.

The calculation can be divided into three significant parts, as shown in Fig. 4.1:

Firstly, the Hamiltonian matrix is set up in the computational basis depending on the sys-

tem parameters like coupling strengths, external fields, and the system size. Typically, we are studying one-dimensional chains of length L (with open or periodic boundary conditions) where each link can be mapped to a qubit so that the shape of the Hamiltonian matrix is $2^L \times 2^L$. We consider both the position and momentum basis. The block structure of the Hamiltonian matrix (which is typically in block diagonal form because of symmetries) is also analysed and stored in memory, and then each of the blocks is diagonalized, which diagonalizes the Hamiltonian. The energy eigenvectors and eigenvalues can be cached on disk to save some time in future executions. If the program is started multiple times with the same parameters to this step, the first program that exclusively locks the cache file will perform this step while the others are waiting and will read the cache once it becomes available. The correct file size and the SHA 256 hash [CST12] of the cache are verified to detect data corruption. This part is usually not very time-consuming (using less than 1% of the computation time for larger system sizes, even when not cached) in part because all expensive operations are handled by highly optimized linear algebra packages like Intel oneAPI or AMD Optimizing CPU Libraries (AOCL). In summary, the main output of this part is the Hamiltonian eigensystem in the 2^L-dimensional computational basis:

$$\hat{H} \left|n\right\rangle = E_n \left|n\right\rangle . \tag{4.1}$$

Secondly, the pure state of the doubled system $ABCD$ is calculated, where AB is the initial system with L qubits and CD is the system time-evolved in the usual way with the time evolution operator $U(t) = e^{-itH}$. The input for this part is the output of the previous part and the duration t of the time evolution. The block structure of the Hamiltonian matrix and the energy eigensystem from the previous step are used to speed up the calculation, which is quite straightforward but can be very time-consuming since the Hilbert space of the doubled system has dimension 2^{2L} and the state vector can get very large. We tried to skip this part and calculate the elements of the state vector on-the-fly in the next part, which slightly reduced memory consumption and dramatically slowed down the program, and this approach was discarded. Optionally, it is possible to include a chemical potential and a finite temperature in this step:

$$\left|U(t)\right\rangle = \frac{1}{\sqrt{Z}} \sum_n e^{-\beta(E_n - \mu N_n)/2} e^{-itE_n} \left|n\right\rangle \otimes \left|n\right\rangle . \tag{4.2}$$

We used this only very rarely, setting $\beta = \mu = 0$ for the most part:

$$|U(t)\rangle = \frac{1}{\sqrt{\dim \mathcal{H}}} \sum_n e^{-itE_n} |n\rangle \otimes |n\rangle . \tag{4.3}$$

Thirdly, the time-dependent reduced density matrices ρ_{AC} and ρ_{AD} are calculated with a partial trace operation that required a large amount of work to test and optimize. The description of the partial trace operation $\rho_{AC} = \mathrm{Tr}_{BD} |U(t)\rangle \langle U(t)|$ (*mutatis mutandis* for ρ_{AD}) can be found in the next section. When the reduced density matrix has been calculated, it is diagonalized with the usual linear algebra packages and its quantum Renyi entropies (cf. Section 2.4) of order one (VON-NEUMANN entropy), two (collision entropy), and infinity (min-entropy) are calculated. The tripartite information can then be calculated as discussed in Section 3.2:

$$I_3(t) = \text{const.} - (S_{AC}(t) + S_{AD}(t)), \tag{4.4}$$

where the constant term is model dependent and can usually be calculated analytically.

4.2 Partial Trace

In this section, we will write out the algorithms in both mathematical notation and diagrams and also show the associated C code to make the material useful to a broader audience. Some of the performance characteristics can only be understood from the actual code, which will be interesting for readers looking to program their own implementation.

As the standard linear algebra operations (diagonalization, QR factorization, matrix-matrix multiplication) are handled by the LAPACK and BLAS routines of optimized software packages (either AMD Optimizing CPU Libraries or Intel Math Kernel Library depending on the CPU vendor), the most complex and computationally demanding operation we had to implement is actually the partial trace operation that yields the reduced density matrices ρ_{AC} and ρ_{AD} from the very large state of the total system ρ_{ABCD}. Other density matrices are easier to calculate, as ρ_{AB} and ρ_{CD} are thermal states that can be constructed explicitly from the eigenvalues and eigenstates of the Hamiltonian, and a simpler partial trace operation that traces out just one subsystem from either ρ_{AB} or ρ_{CD} gives ρ_A, ρ_B, ρ_C or ρ_D. Since these six density matrices are typically also time-independent they only need to be calculated once.

So the most challenging problem that needs to be solved numerically is the partial trace

System Size	Memory Usage $\|U(t)\rangle$	Memory Usage ρ_{ABCD}
2	256 B	4 kiB
4	4 kiB	1 MiB
6	64 kiB	256 MiB
8	1 MiB	64 GiB
10	16 MiB	16 TiB
12	256 MiB	4096 TiB
14	4 GiB	1048576 TiB
16	64 GiB	268435456 TiB

Table 4.1: Memory Consumption of pure states and density matrices of the doubled system $ABCD$

operation that yields ρ_{AC} and ρ_{AD}. A (very) naive implementation might calculate the density matrix ρ_{ABCD} explicitly before the partial trace operation in the manner described in Eq. 4.5 and the following code excerpt[1]. However, the memory consumption (cf. Table 4.1) makes this approach intractable for any system size larger than $L = 8$. Hence, we must calculate the matrix elements of ρ_{ABCD} on-the-fly during the partial trace operation.

$$\langle i_A, i_B, i_C, i_D|\rho_{ABCD}|j_A, j_B, j_C, j_D\rangle = \langle i_A, i_B, i_C, i_D|U(t)\rangle \langle U(t)|j_A, j_B, j_C, j_D\rangle \quad (4.5)$$

```
long long int row_ABCD;
long long int column_ABCD;
long long int dim = 1 << (2 * L);
for(row_ABCD = 0; row_ABCD < dim; row_ABCD++)
{
  for(column_ABCD = 0; column_ABCD < dim; column_ABCD++)
  {
    rho_ABCD[column_ABCD + dim * row_ABCD]
      = state[column_ABCD] * conj(state[row_ABCD]);
  }
}
```

The mathematical equation we have to implement is the following:

$$\langle i_A, i_C|\rho_{AC}|j_A, j_C\rangle = \sum_{d_B=1}^{\dim(\mathcal{H}_B)} \sum_{d_D=1}^{\dim(\mathcal{H}_D)} \langle i_A, d_B, i_C, d_D|U(t)\rangle \langle U(t)|j_A, d_B, j_C, d_D\rangle \quad (4.6)$$

[1]We will use bit shifting to calculate powers of two, e.g. $2^x =$ 1<<x for small positive integers x

A naive implementation of the partial trace might run over the basis states of all subsystems in the following way:

```
for(row_A = 0; row_A < dim_A; row_A++)
  for(row_C = 0; row_C < dim_C; row_C++)
    for(column_A = 0; column_A < dim_A; column_A++)
      for(column_C = 0; column_C < dim_C; column_C++)
        for(diag_B = 0; diag_B < dim_B; diag_B++)
          for(diag_D = 0; diag_D < dim_D; diag_D++)
            row_AC = row_A + dim_A * row_C;
            column_AC = column_A + dim_A * column_C;
            rho_AC[row_AC + dim_AC * column_AC] += [...]
```

The time complexity, in this case, is dominated by memory access since even the system state vector $|U(t)\rangle$ can still become quite large (as we saw in the second column of Table 4.1) and there are only very few simple CPU instructions in the innermost loop. It turns out that a better approach is to access either $|U(t)\rangle$ or $\langle U(t)|$ in memory order, which gives the following outermost loops:

```
for(row_AB = 0; row_AB < dim_AB; row_AB++)
  for(row_CD = 0; row_CD < dim_CD; row_CD++)
    [...]
```

We now have the row indices for access into $\langle U(t)|$, which corresponds to the first two and the last two for loops in the naive implementation merged together. We only need to loop over the columns of the reduced density matrix ρ_{AC} now, which are the remaining two loops in the naive implementation, and then calculate all the indices for access into ρ_{AC} and $|U(t)\rangle$.

```
for(row_AB = 0; row_AB < dim_AB; row_AB++)
  for(row_CD = 0; row_CD < dim_CD; row_CD++)
    for(column_A = 0; column_A < dim_A; column_A++)
      for(column_C = 0; column_C < dim_C; column_C++)
        [...]
```

The system layout is stored in 4 bitmasks `mask_A`, `mask_B`, `mask_C`, `mask_D` that have the nth bit set to 1 if the nth qubit is part of that subsystem and 0 otherwise. Using these, the indices can be calculated by extracting or depositing only exactly the bits masked by the bitmask (see Fig. 4.2). Fortunately, the BMI2 instruction set makes this operation ex-

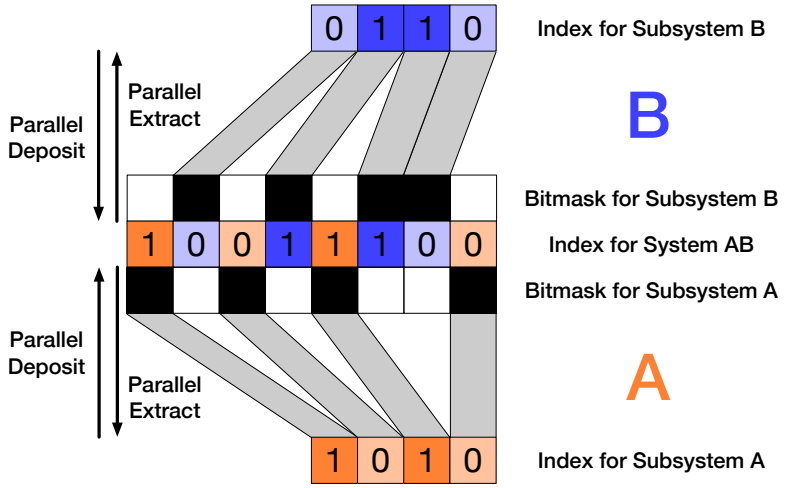

Figure 4.2: Schematic overview of how the indices into the basis sets of the system AB and its subsystems A and B can be transformed into each other using the BMI2 instructions pext (parallel bits extract) and pdep (parallel bits deposit).

tremely fast on newer CPU microarchitectures.

The BMI2 instructions are efficiently implemented in hardware for Intel starting with the Haswell generation (launched in 2013), and for AMD starting with the Zen 3 generation (launched in 2020) [AMD20]. Unfortunately, older Zen architectures implement them in CPU microcode, with a significant performance penalty. Using the Parallel Bits Deposit and Extract instructions the remaining dependent indices are calculated as follows:

```
#include <x86intrin.h>
row_A = _pext_u64(row_AB, mask_A);
row_C = _pext_u64(row_CD, mask_C);
B_diag = row_AB & mask_B;
column_AB = _pdep_u64(column_A, mask_A) + B_diag;
column_CD = _pdep_u64(column_C, mask_C) + D_diag;
```

Since only the last line depends on the innermost loop variable, the other lines can be moved to outer loops (or will be moved by the optimizing compiler anyway) and have even less impact on the performance[2]. For bosonic systems, the only other instructions in the innermost loop are then multiplications/additions to calculate the remaining indices and the actual summation, which looks as follows:

[2]The loops could also be split up in different equivalent ways. However, the presented structure is the one that yielded the best results, given the hardware and compiler versions we had access to at the time. Your mileage may vary.

```
  rho_reduced[AC] += conj(state_ABCD[row_ABCD]) * state_ABCD[col_ABCD];
```

The actual code used (with checks and debugging stripped out) then looks as follows:

```
for(row_AB = 0; row_AB < (1 << L); row_AB++)
{
    row_A = _pext_u64(row_AB, mask_A);
    B_diag = row_AB & mask_B;

    for(row_CD = 0; row_CD < (1 << L); row_CD++)
    {
        row_C = _pext_u64(row_CD, mask_C);
        D_diag = row_CD & mask_D;

        row_ABCD = row_CD + (row_AB << L);

        for(col_A = 0; col_A < (1 << length_A); col_A++)
        {
            col_AB = _pdep_u64(col_A, mask_A) + B_diag;

            for(col_C = 0; col_C < (1 << length_C); col_C++)
            {
                col_CD = _pdep_u64(col_C, mask_C) + D_diag;

                AC = col_C + ((col_A +
                    ((row_C + (row_A << length_C))
                      << length_A)) << length_C);
                col_ABCD = col_CD + (col_AB << L);

                rho_red[AC] += conj(TFD[row_ABCD]) * TFD[col_ABCD];
            }
        }
    }
}
```

We would like to note that the notation previously used in this chapter had been slightly modified for didactic purposes when compared to the organically grown code.

4.2.1 Fermionic Trace

An additional complication arises because the partial trace has to be calculated differently for bosonic and fermionic degrees of freedom. In a simple example, we want to trace out one of the two qubits from a system which is in the state $|\Psi\rangle_{AB} = \frac{1}{\sqrt{2}}(|01\rangle + |11\rangle) = \frac{1}{\sqrt{2}}(1 + \hat{a}_A^\dagger)\hat{a}_B^\dagger|00\rangle$. Here $\hat{a}^\dagger$ are the creation operators that could be either fermionic or bosonic. The partial trace that yields the reduced density matrix looks as follows for this case:

$$\begin{aligned}
\rho_A &= \mathrm{Tr}_B |\Psi\rangle_{AB}\langle\Psi| \\
&= \langle 0|_B |\Psi\rangle_{AB}\langle\Psi| |0\rangle_B + \langle 1|_B |\Psi\rangle_{AB}\langle\Psi| |1\rangle_B \\
&= \frac{1}{2}\langle 0|_B (1 + \hat{a}_A^\dagger)\hat{a}_B^\dagger |00\rangle \langle 00| \hat{a}_B(1 + \hat{a}_A)|0\rangle_B \\
&+ \frac{1}{2}\langle 0|_B \hat{a}_B(1 + \hat{a}_A^\dagger)\hat{a}_B^\dagger |00\rangle \langle 00| \hat{a}_B(1 + \hat{a}_A)\hat{a}_B^\dagger|0\rangle_B \\
&= \frac{1}{2}(1 \pm \hat{a}_A^\dagger)|0\rangle_A \langle 0|(1 \pm \hat{a}_A) \\
&= \frac{1}{2}(|0\rangle \pm |1\rangle)(\langle 0| \pm \langle 1|),
\end{aligned}$$

where the upper sign is valid for bosonic operators that commute and the lower sign for fermionic operators that anti-commute. We note that we get a potential sign on both the left half and the right half of the result, but they do not cancel out in this example, so the final result does depend on the statistics of the particles.

Naturally, the situation becomes more difficult when we now need to trace out two out of four subsystems, each of which can be multiple qubits in size. Our strategy to calculate, for example, the *fermionic trace* Tr_{BD} is to "pull apart" a state into a KRONECKER product where the qubits that need to be traced out are on one side and the qubits that are described by the reduced density matrix we want to calculate are on the other side and count the number of times two creation operators need to be commuted. If the number is even, we have an overall positive sign $|\Psi\rangle_{ABCD} = |\psi\rangle_{BD} \otimes |\psi'\rangle_{AC}$, otherwise an overall negative sign $|\Psi\rangle_{ABCD} = -|\psi\rangle_{BD} \otimes |\psi'\rangle_{AC}$.

Because the binary representation of the row and column indices corresponds exactly to the state of the system in the computational basis, we can easily calculate the sign by iteratively moving the bit representations for the two subsystems (still in the computational basis of the composite system, so with a full width of L bits) relative to each other by bit-shifting one of them and counting the number of bits that are set simultaneously in both

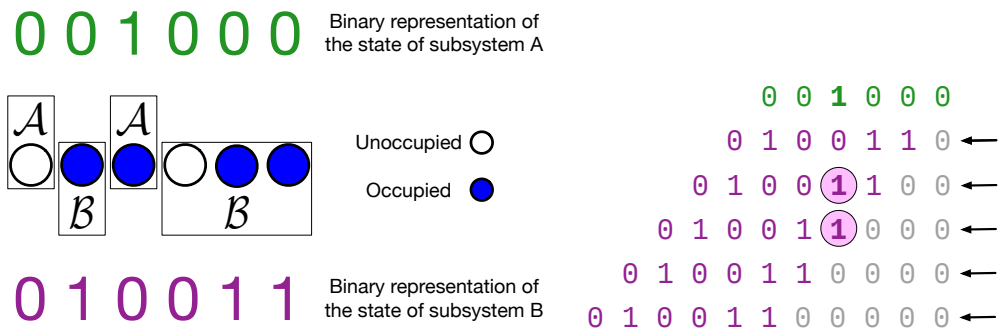

(a) Binary representation of subsystems **(b)** Shifting of one representation

Figure 4.3: a) The binary representation of two subsystems in the computational basis of the composite system. Occupied states inside the respective subsystem are marked with a 1, and unoccupied states or states outside of the subsystem with a 0. b) Shifting of one subsystem's representation with respect to the other and counting the number of overlapping 1 bits (here: two overlaps in total, marked in bold) yields the number of transpositions of fermionic operators.

representations, i.e. the number of overlapping 1 bits. This process is visualized in Fig. 4.3. We have four of these operations since we need to pull apart both AB and CD on the left side of the ket and the right-hand side of the bra similar to the previous example. We need to shift one of the two binary representations (<<), calculate the overlap with a bitwise AND (&) and then count the number of bits set to 1 with the *population count* operation (Modern compilers have a builtin function `__builtin_popcount` (32bit) or `__builtin_popcountll` (64bit) for this). This results in the following code:

```
#include <x86intrin.h>
for(i = 1; i < L; i++)
{
    j += __builtin_popcountll(_pdep_u64(row_A, mask_A) & (B_diag << i));
    j += __builtin_popcountll(_pdep_u64(row_C, mask_C) & (D_diag << i));
    j += __builtin_popcountll(_pdep_u64(col_A, mask_A) & (B_diag << i));
    j += __builtin_popcountll(_pdep_u64(col_C, mask_C) & (D_diag << i));
}
```

The number of operator commutations is then `j`, which gives the correct overall sign as -1^{j}. We note that only the last line inside the loop body depends on our previously innermost loop variable in the partial trace, and the other three lines can be moved to outer loops, with the necessary changes. The complete code of the partial trace with the fermionic

sign implemented which has been used to calculate the results in Schnaack et al. [Sch+19] and Bölter and Kehrein [BK22b] can be found in Appendix B. We also note that the performance increased by about one order of magnitude if the value of L is known at compile time because the compiler vectorizes the tightest inner loop, so we created multiple instances of the source code of the partial trace with fixed values of the system size using preprocessor macros.

Originally this fermionic sign was omitted in our code, which yields reduced density matrices that are physically incorrect, but unfortunately still have all the correct mathematical properties of a density matrix, which makes it harder to spot that there is a problem with the results.

4.3 Random Unitary Sampling

To compute the random unitary operators (cf. Section 3.3), we need to make sure that we sample from the unitary group $U(n)$ using the correct Haar measure.

The issue can be illustrated with a simplified example, where we want to sample from the group of 3D rotations $SO(3)$. To find a random rotation axis, we cast a ray from the origin to a random point on the surface of a sphere centred on the origin, and this sphere is typically parametrized by the azimuthal angle φ and the polar angle θ (spherical coordinate system). In a naive sampling where we picked all polar angles $\theta \in [0, \pi)$ with equal probability, a concentration of probability at the poles would occur since the circles of constant polar angle become smaller and smaller away from the equator (which is the circle with $\theta = \pi/2$), so we need to be more careful. One solution is to pick cartesian coordinates x, y, z from a Gaussian distribution (centred on 0) and normalize the vector to unit length, which yields a random point on the unit sphere as the Gaussian distribution is spherically symmetric. A similar strategy works for general $U(n)$.

We closely follow Mezzadri [Mez07] for the random sampling, where we first generate a quadratic matrix of the desired size and initialize every matrix element with a normal-distributed complex random variable using a Box-Muller transform[BM58] and then use our linear algebra packages to do a QR decomposition[Pre+07], which yields a unitary matrix Q and an upper rectangular matrix R. The unitary matrix Q is then multiplied by a reflection matrix D that is diagonal and has diagonal elements of either $+1$ or -1, where the sign coincides with the sign of the diagonal elements of the rectangular matrix R, $D = sgn(diag(R))$. This last step ensures that the eigenvalue probability density is constant, as required by the Haar sampling. We tested our implementation with some

test samples of size $N = 4096$. The results for the phases of the eigenvalues are shown in Fig. 4.4, where we found the expected probability densities. Naturally, the unitariness was also checked explicitly before production use.

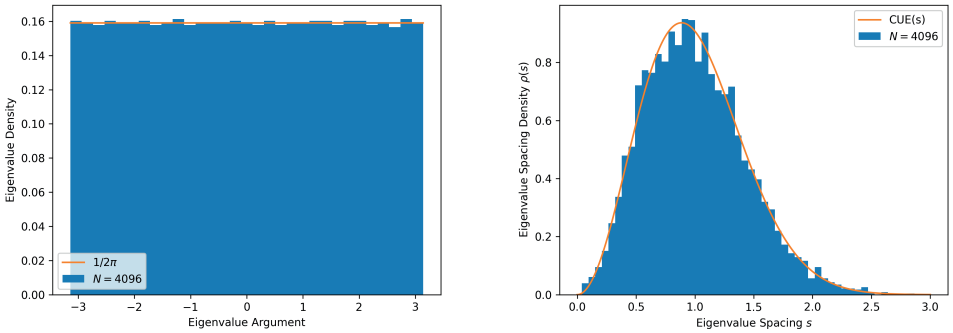

(a) Eigenvalue Distribution

(b) Spacing Distribution

Figure 4.4: Distribution of the eigenvalues (more specifically, their phase angles since their absolute values do not follow a very interesting distribution) of the random unitary samples. a) Shows the probability density of the eigenvalues b) Shows their spacing distribution and the expected Circular Unitary Ensemble CUE distribution (cf. Mezzadri [Mez07]).

4.4 Programming Practices and Testing Methods

Since there were no published results for the tripartite information in the one-dimensional spinless fermion system when the project started, particular care had to be taken to find any inconsistencies in the results without reliable and independent comparison data.

4.4.1 Version Management

As per the research group's requirements for good scientific practice, all source code used to generate scientific results is version-managed using Git [CS14]. In particular, the following repositories were used in the preparation of the published journal articles:

- `qubit-chain-tfd` Calculate the tripartite information of a qubit-chain interpreting the time-evolution operator as a state. Supports spinless fermions, hard-core bosons, transverse-field Ising, XXZ-chain with disorder.
- `xxz-chain-with-disorder-data` Raw data and processed data for the XXZ spin chain with disorder

- `xxz-chain-with-disorder-postprocessing` Python code to generate the processed data and figures for the XXZ spin chain with disorder
- `tfim-chain-with-disorder-data` Raw data and processed data for the Ising spin chain in a transverse field with disorder
- `tfim-chain-with-disorder-postprocessing` Python code to generate the processed data and figures for the Ising spin chain in a transverse field with disorder
- `condor_tools` Some python scripts for use on the GoeGrid[GoeGrid] cluster (rocks) to diagnose the HTCondor queueing system
- `pbs-tools` Some python scripts with improved output compared to qstat, qnodes for use on the rocks cluster

The following repositories were also used for investigations during the project, but the results remain unpublished.

- `transverse-field-ising-model-tfd` Calculate the Tripartite Information for the Fully Connected Transverse Field Ising Model
- `qubit-chain-thermalization` Observe the equilibration of a chain of spinless fermions if two parts are at different temperatures or in different eigenstates initially.
- `cluster-tutorial` A simple project to demonstrate running code on the GoeGrid cluster of the Institute for Theoretical Physics.

These repositories will be found at the research group's page[3] after the publication of this thesis.

Particular care was taken with the central code repository `qubit-chain-tfd` since it contains the code that generated all the raw data we used and has the highest potential for errors. During compilation, the git version hash (which can be found using the shell command `git describe`) was included in the executable programs, and every raw data point was marked with the code version that generated it. This makes it possible to reliably identify any faulty data after a mistake has been found in the code and successfully tracked down to the commit that introduced it.

For the particular implementation for our case (C code built by Make[Make]), the version is put into the executable in the following manner:

[3] Currently located at `https://gitlab.gwdg.de/stefan-kehrein-condensed-matter-theory`

```
#Makefile (simplified)
GIT_DESCRIBE := $(shell git describe --always --dirty|tr -d "\n"|tr -C [:alnum:]_ _)
CFLAGS += -DGIT_DESCRIBE="\"$(GIT_DESCRIBE)\""
# ...
%$(SUFFIX).o: %.c
    $(CC) -c -o $@ $^ $(CFLAGS) $(CPPFLAGS)

fermion-chain: qubit-chain.c qubit-chain-shared.c $(OBJECTS)
        $(CC) -o $@ $^ $(CFLAGS) $(CPPFLAGS) $(LDFLAGS) -DDBPATH="\"fermion-chain.db\""

# ...
```

And the preprocessor macro `GIT_DESCRIBE` can then be used to get the git version:

```
// C code (snippet)
// ...
  printf("Version %s (compiler version %s)\n", GIT_DESCRIBE, __VERSION__);
// ...
```

If any uncommitted changes were present during the compilation, the suffix `-dirty` is added to the version hash by git, and raw data that has a "`-dirty`" version is not used for publication so that the exact state of the codebase that generated a dataset is known. If a mistake is found in the code, all the raw data generated with the affected versions are verified and, if necessary, discarded.

The git version hash of the LaTeX 2_ε source code for this thesis is `fc37d75`.

4.4.2 Assertions

The intermediate data inside the program has to fulfil many mathematical and physical properties that can be checked. Almost all of the found programming errors were immediately found by these straightforward checks.

The simplest checks are on the input parameters:

- System size is an integer larger than one
- Temperature is non-negative
- The specified subsystems actually fit inside the total system size

In particular, for data that is cached between program invocations, the following requirements have been implemented:

- The filename for both writing and reading is automatically generated and not input by the user
- All system parameters that affect the cached data are included in the filename of the cache file
- While the data to be cached is calculated, an exclusive write lock is held on the cache file
- All other processes waiting on the data hold a shared read lock and block execution while the data is calculated
- The binary data is checksummed using SHA256 [CST12] and the checksum stored in the cache file
- Before using cached data, the length and checksum of the data are verified

For data that is not read from the cache but generated on the fly, all the following properties are checked using an explicit calculation during regular execution of the program:

- Hamiltonians conserve particle number, momentum and/or total magnetization
- Eigenvectors are normalized
- The eigenvalues of density matrices are all non-negative and sum up to one

There is also a debug mode, which checks the following additional properties that have a larger impact on performance:

- Hamiltonians are hermitian
- Density matrices are hermitian
- Random unitary operators are unitary
- The entropies of subsystems BD, BC, and CD are indeed identical to those of AC, AD, and AB, respectively

To verify that the Hamiltonian is correctly implemented, we fed the symbolic notation of the Hamiltonian into the python package QuSpin [WB17; WB19] and compared the eigenvectors and eigenenergies. For the spin chains, we also implemented the Hamiltonian using just Pauli matrices and linear algebra functions from the linear algebra library armadillo

[SC16; SC18] to construct the 1-spin and 2-spin operators explicitly and sum them all up. This yielded the same Hamiltonian matrix, although at a glacial speed when compared to our C implementation and unusable for production usage.

None of these checks caught the missing minus signs in the fermionic trace, as described in the previous section. It was, however, caught by manual testing in the following sense: for the spinless fermion chain with periodic boundary conditions (the spinless fermion *ring*), all results need to be translation invariant. This provides an additional sanity check, which the program failed since moving the subsystems in lockstep around the ring changed the results, which was clearly an unphysical effect.

This unphysical effect was also present in a previous implementation, and we eventually discovered that partial traces with fermions are tricky since the anti-commuting operators cause many minus signs to appear. After both codes were fixed by adding all the fermionic minus signs, the results were indeed translation invariant, as required. After this, the previous results for the spinless-fermion chain had to be reevaluated, the details of this can be found in Chapter 5.

4.4.3 Comparison to Analytical Results

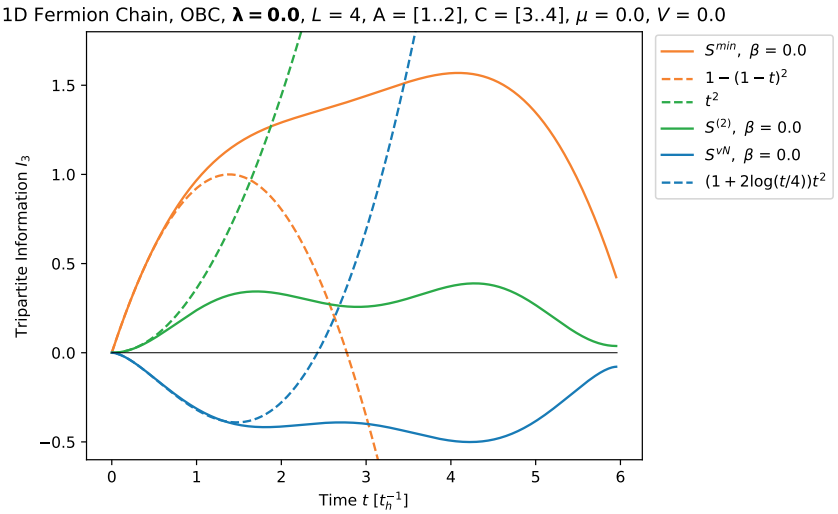

Figure 4.5: Comparison of the analytical and numerical results for the free spinless fermion chain (only nearest-neighbour hopping) for short times. The analytical calculation is only valid up to quadratic order in time. The system and its parameters will be described in more detail in Chapter 5.

We also tried to calculate the tripartite information analytically for a simple system of non-interacting spinless fermions or hard-core bosons. The calculation can be found in Appendix D, where we managed to find the short-behaviour of the tripartite information (for the VON-NEUMANN, the min-Entropy, and the collision entropy cases, cf. Section 2.4) up to quadratic order in time in an extended chain. The simplest case is the collision tripartite information, where for the fermions, the result is again quadratic in time and positive ($I_3^{(2)} = t^2 + O(t^3)$), while the sign is reversed for the hard-core bosons ($I_3^{(2)} = -t^2 + O(t^3)$). The results for the free fermion chain are shown in Fig. 4.5, where we see that the short-time behaviour of our numerical results matches the analytical calculations.

4.4.4 Comparison to Numerical Results

Our numerical results for the spinless fermion system were also compared to data that was generated using the SymMPS framework[SymMPS] created by Thomas Köhler and Sebastian Paeckel. We used both the TDVP and MPO time evolution methods to create time-evolved states with a system size of $L = 8$ and calculated about 50000 different data points for the tripartite information, where the largest deviation from our numerical results was off by a factor of about 1/500. The details of the SymMPS setup can be found in Appendix C. For a review of the method used please see Paeckel et al. [Pae+19].

We also performed some regression tests, where we stored the data generated by an earlier version of the program and performed an automated test to verify that the current version generated the same data, up to some precision cutoff. The cutoff is required because, for example, the IEEE 754 floating point numbers implemented in the computer hardware are not associative and the order of operations slightly affects the result between versions and CPU models. We used a cutoff of $\Delta = 10^{-12}$ and did not see any failed tests. Because different models were studied throughout the project, these tests were of somewhat limited usefulness and can probably be skipped if it is possible to do external verification using independent results instead.

4.4.5 Data Publication

The raw data that was generated by the code in the `qubit-chain-tfd` repository and then processed has also been published on the Göttingen Research Online platform of our university. In particular, replication data for Schnaack et al. [Sch+19] has been published in Schnaack et al. [Sch+21], and replication data for Bölter and Kehrein [BK22b] has been published in Bölter and Kehrein [BK22a]. In the second case, the code in the repository

`xxz-chain-with-disorder-postprocessing` from the research group's GitLab page[4] can be used to generate the figures directly from the processed data.

4.5 Row- and Column-Major Order

Another issue that we encountered is the layout of multi-dimensional data in different programming languages. Python's numpy and C use the row-major layout, while FORTRAN (and MATLAB) use the column-major layout, which is equivalent to transposing any matrix exchanged between the two conventions. Since the LAPACK and BLAS FORTRAN interfaces[And+99] are used for low-level linear algebra operations, it is important to keep this distinction in mind.

While studying the transverse field Ising chain in Section 6.3, we saw that the behaviour of the spin-glass order parameter deviated slightly from published results which was caused by mixing up the data layouts during the calculation of the order parameter. Unfortunately, a verification of the results against eigenvectors from the Python QuSpin package[WB17] showed identical deviations because we assumed that the eigenvectors returned by QuSpin would be accessed like `eigenvectors[i]`. However, since the same FORTRAN interface is used in the background, the returned matrix has to be transposed and the eigenvectors accessed like `eigenvectors[:,i]`. After this was fixed in both implementations our results were consistent with those found in Kjäll, Bardarson, and Pollmann [KBP14].

[4] `https://gitlab.gwdg.de/stefan-kehrein-condensed-matter-theory/`

Chapter 5

Scrambling in Translation Invariant Systems

5.1 Spinless Fermions

The first system we studied is a chain of spinless fermions described by the following Hamiltonian H:

$$H = -\frac{1}{2}\sum_{j=1}^{L}\left(\hat{c}_j^\dagger \hat{c}_{j+1} + \lambda \hat{c}_j^\dagger \hat{c}_{j+2} + \text{H.c.}\right) + V\sum_{j=1}^{L}\hat{c}_j^\dagger \hat{c}_j \hat{c}_{j+1}^\dagger \hat{c}_{j+1} \tag{5.1}$$

This model has been non-dimensionalized by setting the pre-factor of the nearest-neighbour hopping to unity, which leaves two dimensionless parameters: the strength of the hopping between next-nearest neighbours λ and the repulsion of fermions on neighbouring sites described by V. If both λ and V vanish, the model can be solved by a simple Bloch wave ansatz [Blo29], which yields a cosine dispersion relation. If the repulsive interaction V is turned on, the model is still integrable via Bethe ansatz [Bet31; YY66b; YY66a], while turning on both parameters will give a non-integrable model. Using the tripartite information we can explore the scrambling behaviour in these different regimes.

The natural choice for a partitioning of the 2^L-dimensional Hilbert space into L qubits is the position basis, where each qubit corresponds to one lattice site. It is important to note that this partitioning is sensible both for open boundary conditions (where the inter-

action between the last and first qubits is dropped) and for periodic (BORN-VON KÁRMÁN) boundary conditions. The other physically relevant partitioning we looked at is into momentum modes by performing a FOURIER transform of the system with periodic boundary conditions, where the Hamiltonian can be written as follows: [Sch+19]

$$\begin{aligned} H = &- \sum_k \left(\cos(k) + \lambda \cos(2k)\right) \hat{c}_k^\dagger \hat{c}_k \\ &- \frac{V}{N} \sum_{k,k',q} \cos(q) \hat{c}_{k+q}^\dagger \hat{c}_{k'-q}^\dagger \hat{c}_k \hat{c}_{k'} \end{aligned} \tag{5.2}$$

In this representation, the Hamiltonian has fewer off-diagonal scattering terms since all the hopping terms have moved to the diagonal. It is even entirely diagonal if the interaction strength V is turned off, and we expect that the scrambling dynamics are strongly suppressed in this simple case. Each qubit corresponds to one momentum mode, i.e. the qubit state $|1\rangle$ represents an occupied mode and $|0\rangle$ an unoccupied mode. Otherwise, the construction is identical to that in position space.

We looked only at the three previously mentioned cases: position and momentum representation in the periodic system, and position representation in the system with open boundary conditions. In theory, there are many more ways to partition the HILBERT space into qubits, though most of them do not seem physically relevant, still, it might be possible that a particular partitioning is of interest for a specific model system only.

In order to calculate the tripartite information, only the time-dependent entropies S_{AC} and S_{AD} need to be calculated numerically (see Chapter 3):

$$I_3(t) = L - (S_{AC}(t) + S_{AD}(t)). \tag{5.3}$$

The results for the periodic system are shown in Fig. 5.1, where we see that for the non-interacting case $V = 0$, the scattering is strongly suppressed: In position space, the tripartite information stays far below the HAAR-averaged value, while in momentum space – where the Hamiltonian is diagonal – there is no scrambling at all, as the tripartite information vanishes for all times. The diagonal terms in the Hamiltonian do not contribute to the scrambling in this case. In the interacting case, the approach to the HAAR value is slower in momentum space, which agrees with our earlier observation that there are fewer off-diagonal scattering terms in the momentum representation. The plateau that is eventually reached is also slightly below the HAAR-averaged value, which we will discuss further down.

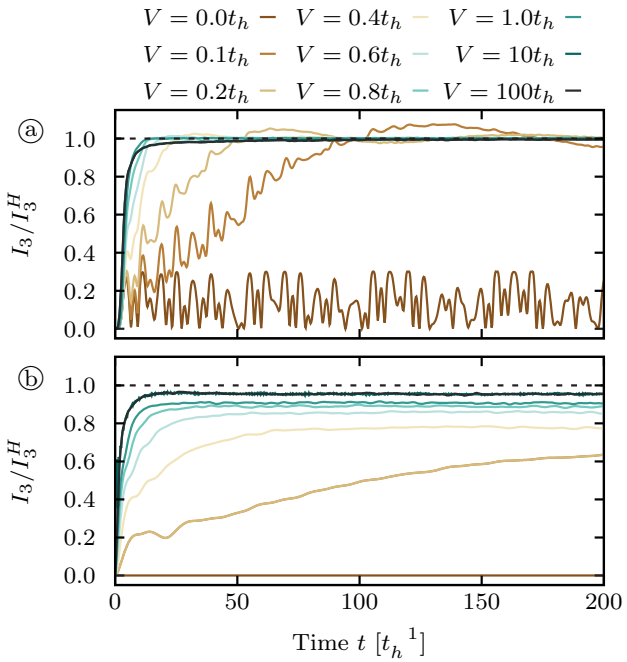

Figure 5.1: Time evolution of the negative tripartite information in a chain of $N = 12$ sites for $\lambda = 0.5$ and different values of the interaction V. (a) In real space, where A and D are single-site subsystems on diametrically opposing sides of the ring. (b) In momentum space, where A is the mode $n = 0$ and D is the mode $n = 11$. The dashed lines indicate the HAAR-scrambled value of the tripartite information. Figure 2 from Schnaack et al. [Sch+19].

Since the Hamiltonian is short-ranged, we also expect information to travel through the system at a finite speed, which is why we looked at the system in position space, the results of which are shown in Fig. 5.2. The ballistic spreading of information can be observed, as the arrival time scales linearly with the distance. We did choose open boundary conditions because this allows for longer distances between the subsystems and do not expect any significant effects on our results apart from the obvious observation that the spreading in the periodic system is happening in both directions. The data for the periodic case is shown in Fig. 5.3 (not published), where we see qualitatively the same behaviour, as well as matching butterfly velocities (1.97 ± 0.02 and 1.96 ± 0.06).

It is known from OTOCs (which were introduced in Section 3.4) that the spreading of correlations is not purely ballistic as described by a step function $\Theta(x_0 - v_B \cdot t)$ but that there is a diffusive broadening of the wavefront proportional to $\sqrt{t}$ [vKey+18; RPvK18; KHN18; SXS19; Kna18]. The broadening is clearly visible in Fig. 5.2, and the correct functional

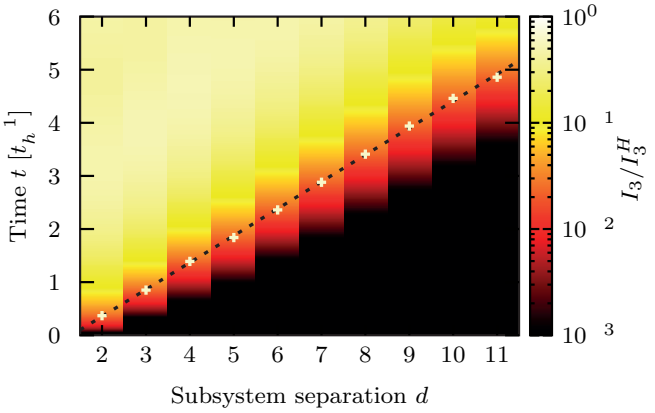

Figure 5.2: Dynamics of tripartite information in the space-time plane. The plot shows the time evolution of the tripartite information with varying distances between the subsystems A and D for a system of $N = 12$ lattice sites in the non-integrable regime, $\lambda = 0.5$ and $V = 0.5$. The crosses mark the points at which $-I_3 = 0.031$ and the dashed line is a linear fit to these points yielding a butterfly velocity of $v_B \approx 1.97$. Figure 3 from Schnaack et al. [Sch+19].

form has been verified in Fig. 5.4, consistent with the previous results.

One striking feature of the tripartite information as a measure for scrambling is how sensitive it is to weak scattering terms in the Hamiltonian, as can be seen in Fig. 5.5. The asymptotic value at large times $I_3(t), t \gg 1$ changes strongly already for very weak interaction strengths V.

As we saw before, the asymptotic value of the tripartite information at late times stays significantly below the HAAR-averaged value for the momentum space partitioning. Notably, the random samples from the unitary group that are used in this average are not dense $2^L \times 2^L$ matrices but have to respect the same symmetries as the Hamiltonian, so they do not mix states from different symmetry subsectors. The local information in the system can be symmetry-protected, which is why symmetry-adapted HAAR unitaries are used (see Section 4.3 for the implementation details).

Two potential explanations for the deviation from the HAAR-averaged value come to mind: the random unitaries are not fully symmetry-adapted and mix some symmetry sectors, artificially inflating the magnitude of the HAAR-averaged value or finite-size effects due to the limited numerically accessible system sizes. In this case, finite-size effects turned out

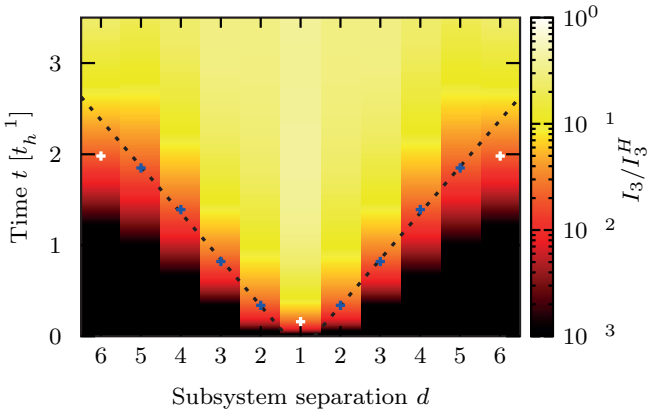

Figure 5.3: Dynamics of tripartite information in the space-time plane. The plot shows the time evolution of the tripartite information with varying distances between the subsystems A and D for a system of $N = 12$ lattice sites in the non-integrable regime, $\lambda = 0.5$ and $V = 0.5$. The crosses mark the points at which $-I_3 = 0.031$ and the dashed line is a linear fit to these points yielding a butterfly velocity of $v_B \approx 1.96$.

to be the most likely explanation, see Fig. 5.6. We first study the other possibility in some detail to verify this.

When calculating the HAAR-averaged value of the tripartite information, the symmetries of the system need to be taken into account instead of using a completely generic unitary operator that mixes all 2^L components of the system state. The block structure of the Hamiltonian in the computational basis is automatically taken into account by a recursive algorithm that finds all basis states $|i\rangle$ and $|j\rangle$ that are coupled together by the Hamiltonian ($\langle i|\hat{H}|j\rangle \neq 0$) and then used to construct the symmetry-adapted random unitary samples. In the fermion system under consideration, this approach takes care of the particle number and momentum conservation automatically. In addition, the Hamiltonian is invariant under the parity transformation T that corresponds to a reflection in real space. For a state in the momentum occupation representation, the parity transformation (which flips the sign of all velocities) will just replace occupied with unoccupied states, i.e. all occupation bits are flipped: $T|01011\rangle = |10100\rangle$. Only in the subspaces with total momentum $k = 0, \pi$ is the parity a good quantum number, because this is the only case in which the parity operator commutes with the momentum operator ($[P, T]\big|_{k=0,\pi} = 0$), or, in other words, the movement of the particles does not have a preferred direction that could be flipped by the reflection [San10]. We generated large Hamiltonian matrices ($L = 18$)

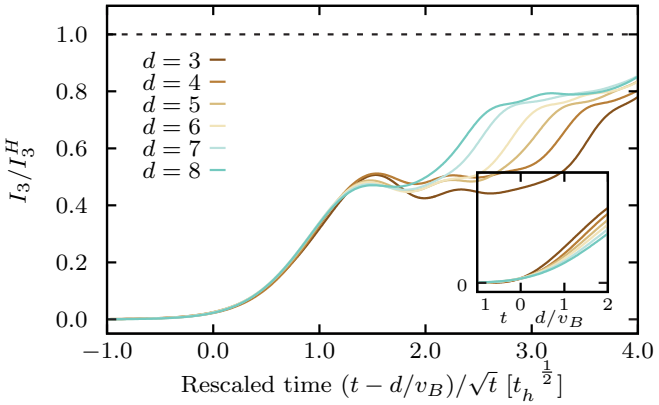

Figure 5.4: Broadening of the wavefront for the same parameters as in Fig. 5.2. The data obtained for the dynamics of the tripartite information with different distances d between subsystems coincide after shifting according to the butterfly velocity v_B and a rescaling by $t^{-1/2}$ to account for *diffusive broadening*. The inset shows the same data without a rescaling of the time axis for comparison. Figure 4 from Schnaack et al. [Sch+19].

and analysed the level statistics with code provided by Nils Abeling for the unfolding of the energy levels [SR10; Bro+81] for the largest blocks of the Hamiltonian with $k = 0, \pi$, which is shown in Fig. 5.7. If the entire block corresponds to a symmetry sector of the system, we should see level repulsion and the level statistics should look Wigner-Dyson like (shown as a solid curve) [Gau61; GMW98]. The probability close to zero level spacing, however, is clearly non-zero, and we fail to see level repulsion. This points us towards the additional parity symmetry, which we implemented by rotating only these blocks into the parity eigenbasis (which has eigenvalues ± 1 and eigenvectors $|n\rangle \pm T|n\rangle$) to split each of them into two smaller blocks with well-defined parity. The level statistics for both the even and odd parity subsectors are shown in Fig. 5.8, where we now clearly see level repulsion. All other blocks of the Hamiltonian that are large enough to analyse already show level repulsion, so we have successfully found a basis that is compatible with all the symmetries of the system. The symmetry-adapted random unitary operator can then be built as a block-diagonal matrix in this basis where each block is randomly sampled from the unitary group of the respective dimensionality (see Section 4.3 for the implementation details) before the operator is rotated back into the computational basis by inverting the rotation described earlier.

Unfortunately, this additional symmetry adaptation does not change the Haar-averaged value of the tripartite information in any meaningful way, so we are left with the explanation that the deviation from the Haar value in momentum space is not due to some ne-

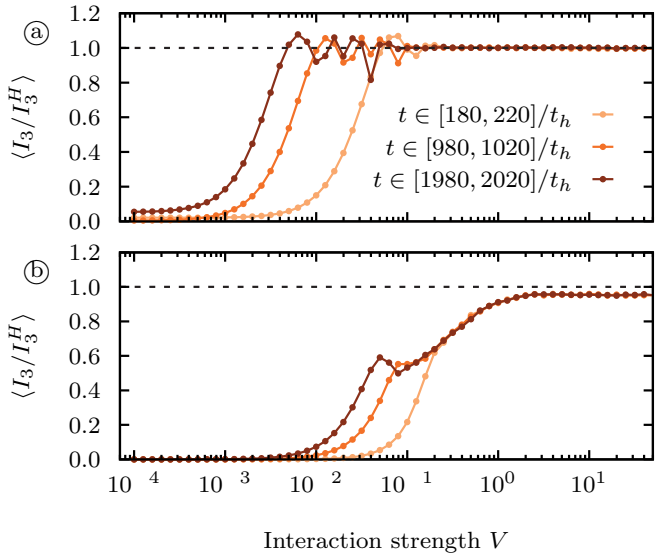

Figure 5.5: Averages of $-I_3$ taken over different intervals $[t_0, t_0 + \Delta t]$ as a function of the interaction parameter V for $\lambda = 0.5$. (a) In real space, where A and D are single-site subsystems on diametrically opposing sides of the ring. (b) In momentum space, where A is the mode $n = 0$ and D is the mode $n = 11$. Here $N = 12$ and the dashed line indicates the HAAR-scrambled value. Figure 5 from Schnaack et al. [Sch+19].

glected symmetry but instead an effect due to the limited system size L available with our numerics.

Finally, as we pointed out at the beginning, the system is BETHE integrable if the next-nearest neighbour hopping is not present ($\lambda = 0$), and we also studied this case, which is shown in Fig. 5.9 [Bet31; YY66b; YY66a]. It turns out that we could not see any significant differences in comparison with the non-integrable case. This is an indication that scrambling is caused by the scattering terms in the Hamiltonian and is separate from integrability. In particular, the scrambling is not necessarily suppressed in the computational basis just because there exists a complicated basis in which the system becomes simple.

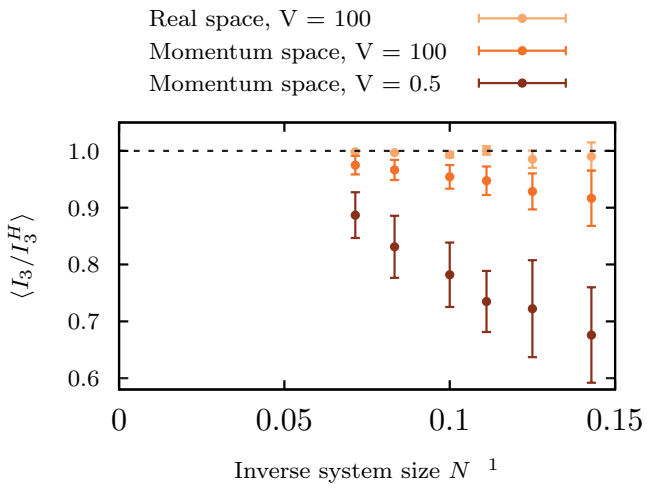

Figure 5.6: Averages of $-I_3$ at late times ($t > 2000$) for different inverse system sizes N^{-1} for $\lambda = 0.5$. The A and D subsystems are of minimal size again but were averaged over all possible choices of sites or momentum modes, which causes larger errors in the momentum data. The dashed line indicates the HAAR-scrambled value. Figure 6 from Schnaack et al. [Sch+19].

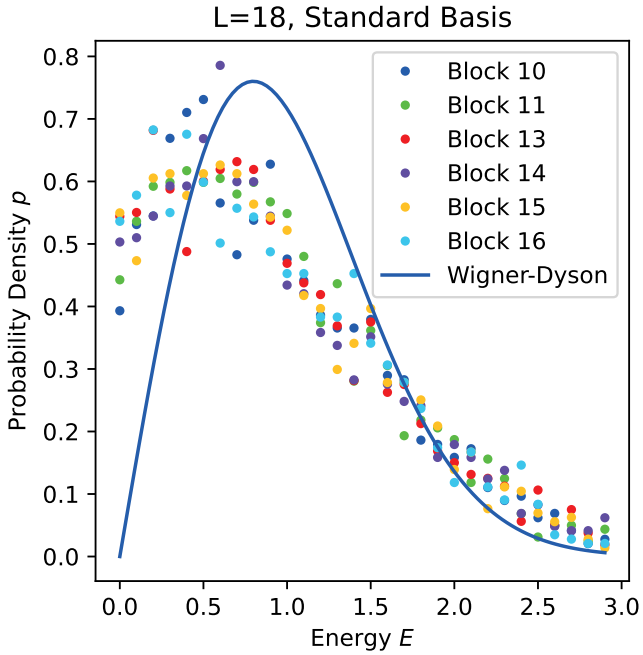

Figure 5.7: Level statistics of the $k = 0, \pi$ blocks of total momentum for the fermionic system with $V = 1$ and system size $L = 18$.

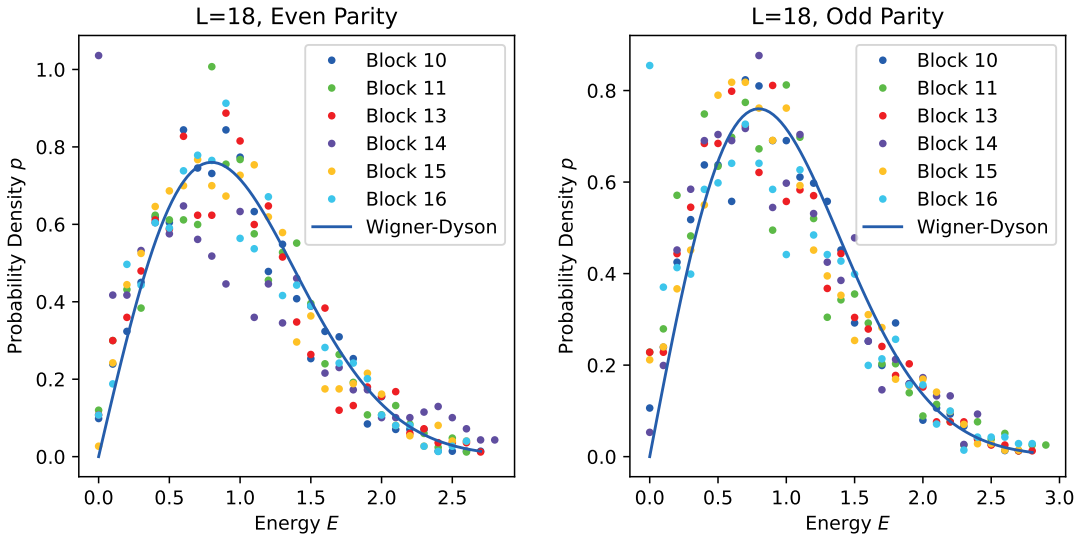

(a) Even parity

(b) Odd parity

Figure 5.8: Level statistics of the $k = 0, \pi$ blocks of total momentum of particular parity for the fermionic system with $V = 1$ and system size $L = 18$.

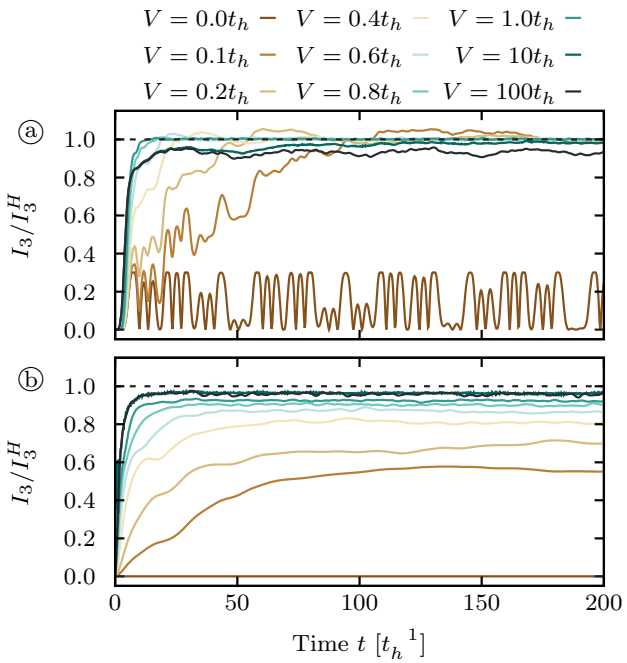

Figure 5.9: Time evolution of the negative tripartite information in a chain of $N = 12$ sites in the integrable regime with $\lambda = 0$ for different values of the interaction V. (a) In real space, where A and D are single-site subsystems on diametrically opposing sides of the ring. (b) In momentum space, where A is the mode $n = 0$ and D is the mode $n = 11$. The dashed lines indicate the HAAR-scrambled value of the tripartite information. Figure 7 from Schnaack et al. [Sch+19].

5.2 Hardcore Bosons, Finite Temperature and Second Rényi Entropy

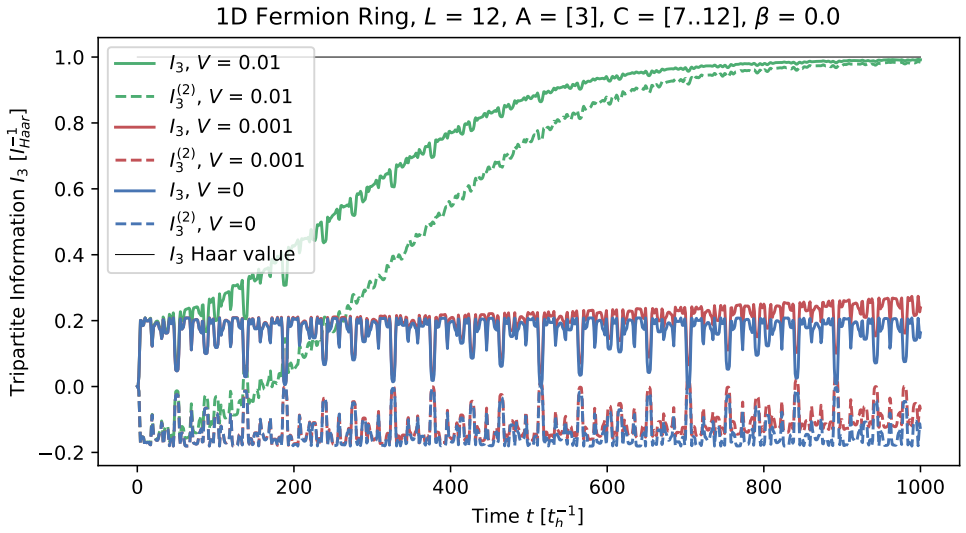

Figure 5.10: Time evolution of the tripartite information in a chain of $L = 12$ sites with subsystem sizes $|A| = 1$ and $|C| = 6$. The input system AB consists of spinless fermions at infinite temperature $\beta = 0$.

We also investigated some additional translation-invariant systems, for example, setups where the input state to the unitary quantum channel is not the maximally mixed state but a thermal state with a finite temperature. This gives rise to the following state to describe the unitary channel:

$$|U(t)\rangle_\beta = \frac{1}{\sqrt{Z}} \sum_n e^{-\beta H/2} |n\rangle_{AB} \otimes e^{-iHt} |n\rangle_{CD}, \tag{5.4}$$

where the input state can be calculated in the usual way and yields the Gibbs state as expected:

$$\mathrm{Tr}_{CD} |U(t)\rangle_\beta \langle U(t)| = \frac{1}{Z} e^{-\beta H}. \tag{5.5}$$

We also considered the tripartite information calculated using the second-order Rényi entropy $S^{(2)} = -\log \mathrm{Tr}\, \rho^2$, which has been linked directly to the decay of Out-of-Time-Order correlation functions (for the details we refer to Section 2.4 on Rényi entropies and Section 3.4 on OTOCs). In addition, we looked at the bosonic equivalent of the spinless fermion system, which is that of the *hard-core bosons* that fulfil bosonic commutation relations but which still have occupation numbers limited to either 0 or 1 like their fermionic counter-

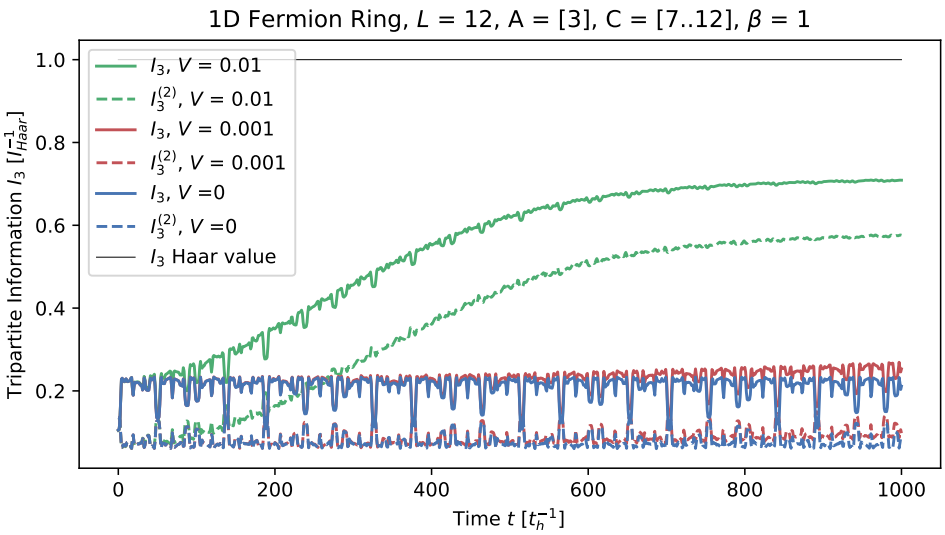

Figure 5.11: Time evolution of the tripartite information in a chain of $L = 12$ sites with subsystem sizes $|A| = 1$ and $|C| = 6$. The input system AB consists of spinless fermions at finite temperature $\beta = 1$.

parts (see Section 5.3 for the exact definition). This limitation causes the local Hilbert space to still be two-dimensional and keeps the interpretation of the lattice sites as qubits valid. In the position representation, the calculation with hard-core bosons is very similar to that of spinless fermions, just that the minus signs from the anti-commutation relations are missing in the Hamiltonian matrix and when the partial trace is calculated.

The case considered in the previous section, spinless fermions at infinite temperature, is shown in Fig. 5.10, where we see that the second-order Rényi tripartite information also converges to its respective HAAR limit in agreement with the results for the VON-NEUMANN or first order Rényi entropy considered before. The main difference is that the free system without interactions now fluctuates at a positive value of the tripartite information, almost mirroring its counterpart with respect to the x-axis. Qualitatively we still have the same behaviour, though: as the information is scrambled, the tripartite information converges to a large negative value that is identical to the tripartite information associated with random unitary operators. The finite-temperature case is shown in Fig. 5.11, where we see similar behaviour in the shape of the curves, but the scrambling is suppressed below the HAAR-averaged value by the lower temperature. To properly diagnose scrambling for this case, a generalization of the HAAR-averaged value to finite temperature would be optimal, which we could not find so far.

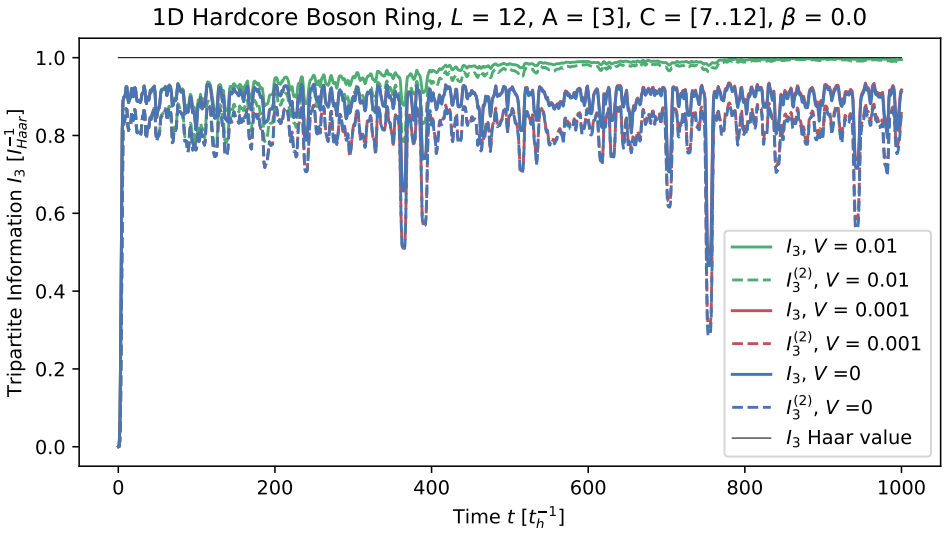

Figure 5.12: Time evolution of the tripartite information in a chain of $L = 12$ sites with subsystem sizes $|A| = 1$ and $|C| = 6$. The input system AB consists of hard-core bosons at infinite temperature $\beta = 0$.

As the temperature is decreased further, the amplitude of the tripartite information signal will continue to shrink as well, vanishing completely if the input state is frozen into the ground state of the model. This is also consistent with the fact that a pure input state always has a vanishing tripartite information, which we already saw in Section 2.2.

Despite the issues, it might still be possible to study the system in an energy-resolved way: the input state could be selected to be an equal mixture of states that lie in a certain energy window, in which case the HAAR-averaged value calculated for the same input would be a valid reference value again, or scrambling could be diagnosed by looking at the decay of fluctuations as the tripartite information equilibrates. If the fraction of participating states divided by the total number of states is small enough, it should be possible to write an optimized program that takes advantage of this and which can use our current implementation for independent validation of the results in lieu of the availability of analytical results. We leave this program as an exercise for the reader.

The situation for hard-core bosons at infinite and finite temperatures is shown in Fig. 5.12 and Fig. 5.13 respectively. Interestingly, the VON-NEUMANN and second-order Rényi tripartite information now behave quite similarly, with both staying negative. The difference between the free and the interacting case in terms of amplitude is strongly reduced, with both showing large jumps initially. The (non-)convergence to the HAAR-averaged value,

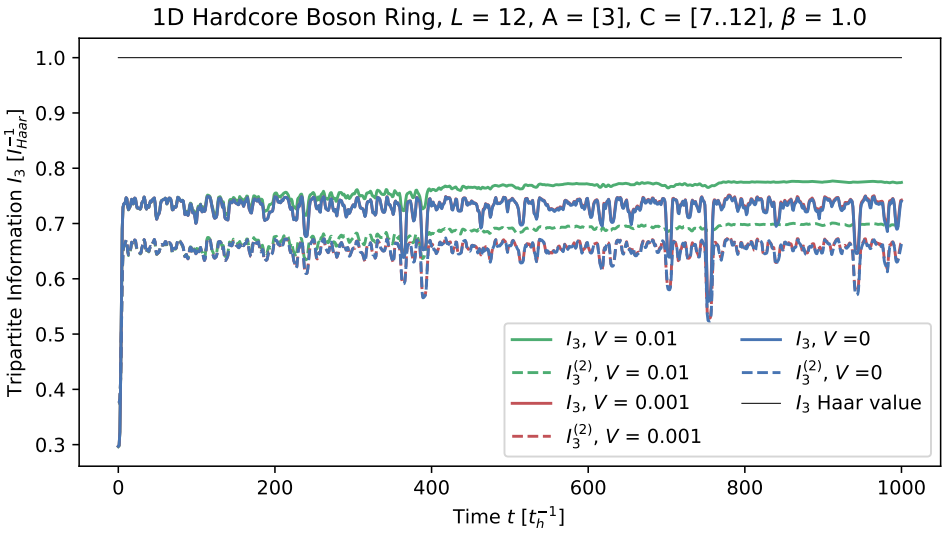

Figure 5.13: Time evolution of the tripartite information in a chain of $L = 12$ sites with subsystem sizes $|A| = 1$ and $|C| = 6$. The input system AB consists of hard-core bosons at finite temperature $\beta = 1$.

however, remains qualitatively the same as for the fermionic case.

It should be added that although there are initial jumps visible in all of the data shown in this section, there is still a delay (given by the distance between the subsystems divided by the butterfly velocity) before the tripartite information deviates from its initial value, even though this cannot be resolved with the naked eye in the figures.

5.3 Analytical Results for the Free Case

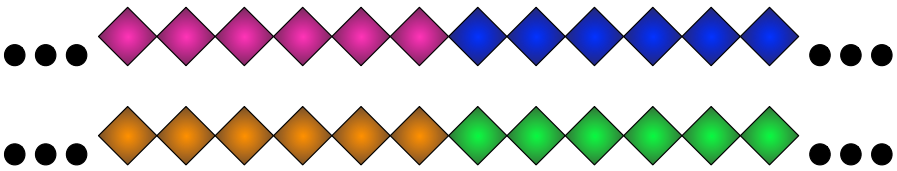

Figure 5.14: System layout for the analytical calculations: both the input and the output systems are partitioned into half-chain subsystems

We also calculated the tripartite information analytically for a simple system of non-interacting qubits for both fermionic and bosonic operators. We used open-boundary conditions, and all subsystems are extended, as shown in Fig.5.14. This simplifies the calculations since the system is only cut in one place, far away from boundaries.

For the fermionic case, we have spinless fermions with creation operators in position representation $\{\hat{c}_i^\dagger\}_{i=1..L}$ that fulfil the usual canonical anti-commutation relations:

$$\{\hat{c}_i, \hat{c}_j^\dagger\} = \delta_{ij}, \quad \{\hat{c}_i, \hat{c}_j\} = 0, \quad \{\hat{c}_i^\dagger, \hat{c}_j^\dagger\} = 0. \tag{5.6}$$

And for the bosonic case, we have hard-core bosons with creation operators in position representation $\{\hat{b}_i^\dagger\}_{i=1..L}$ which anti-commute on-site:

$$\{\hat{b}_i, \hat{b}_i^\dagger\} = 1, \quad \{\hat{b}_i, \hat{b}_i\} = \{\hat{b}_i^\dagger, \hat{b}_i^\dagger\} = 0. \tag{5.7}$$

They commute in all other cases in the usual bosonic way:

$$[\hat{b}_i, \hat{b}_j^\dagger] = [\hat{b}_i, \hat{b}_j] = [\hat{b}_i^\dagger, \hat{b}_j^\dagger] = 0, \quad i \neq j. \tag{5.8}$$

We begin in both cases with the simple quadratic Hamiltonian of particles hopping between neighbouring sites:

$$H = \sum_{i=1}^{L-1} \hat{c}_i^\dagger \hat{c}_{i+1} + \text{H.c.}, \quad H = \sum_{i=1}^{L-1} \hat{b}_i^\dagger \hat{b}_{i+1} + \text{H.c.} \tag{5.9}$$

We will describe the remainder of the calculation using the fermionic notation, where the necessary changes are implied for the bosonic case.

Because the tripartite information is invariant under the exchange of its arguments (see Chapter. 2), it is also independent of the state of any of the four subsystems, so unitary operators that only affect individual subsystems can be applied in addition to the time-evolution operator without changing the result. This motivates a split-up of the Hamiltonian into two parts $H = H_0 + H_\bowtie$, a local part H_0 which only acts on single subsystems and one which couples different subsystems ($H_\bowtie$). The coupling Hamiltonian only has two terms, which will simplify the calculation:

$$H_\bowtie = -\left(\hat{c}_j^\dagger \hat{c}_{j+1} + \hat{c}_{j+1}^\dagger \hat{c}_j\right)\Big|_{j=L/2} \tag{5.10}$$

We can then define an effective time evolution operator $\tilde{U}(t)$, which yields the same tripartite information as the original one and do a short-time expansion using the Baker-

Campbell-Hausdorff formula:

$$\tilde{U}(t) = e^{iH_0 t} e^{-i(H_0+H_{\bowtie})t} = e^{-iH_{\bowtie}t+\frac{1}{2}[H_0,H_{\bowtie}]t^2} + O(t^3) \tag{5.11}$$

$$= 1 - itH_{\bowtie} - \frac{t^2}{2}H_{\bowtie}^2 + \frac{t^2}{2}[H_0, H_{\bowtie}] + O(t^3) \tag{5.12}$$

And after a straightforward calculation (which can be found in Appendix D) we get the early-time behaviour of the tripartite information:

Spinless Fermions

$$\begin{aligned} S_{AC}^{(2)} &= t^2 + O(t^3) \\ S_{AD}^{(2)} &= L - 2t^2 + O(t^3) \\ I_3^{(2)} &= L - (S_{AC}^{(2)} + S_{AD}^{(2)}) = t^2 + O(t^3). \end{aligned}$$

Hardcore Bosons

$$\begin{aligned} S_{AC}^{(2)} &= t^2 + O(t^3) \\ S_{AD}^{(2)} &= L + O(t^3) \\ I_3^{(2)} &= L - (S_{AC}^{(2)} + S_{AD}^{(2)}) = -t^2 + O(t^3). \end{aligned}$$

These analytical results agree with results from our numerical code ($L = 10$), calculating the contributions in the third order in time, however, would require a different approach to prevent a painfully long calculation, which we have been unable to find so far.

Chapter 6

Scrambling in Disordered Systems

6.1 Introduction to Disordered Systems

In this chapter, disorder is introduced to obstruct the flow of information. The main part contains results for the XXZ-model that have also been published in Bölter and Kehrein [BK22b].

A well-established concept in disordered systems is that of *Anderson Localization*, where transport breaks down in disordered non-interacting systems [And58]. In the one-dimensional systems we are studying here, this already happens at arbitrary small values of the disorder strength in the thermodynamic limit [GV59; MT61]. However, since we are studying finite systems, we can only resolve length scales that are smaller than the total system size L. Because of this, we expect to see a transition in the observable effects of localization in our system at a non-vanishing amount of disorder when the localization length becomes comparable to the system size.

We will primarily focus on a related concept that has attracted more attention recently, which is the *many-body localization* (MBL) associated with disordered interacting systems [OH07; GMP05; BAA06]. In this case, there is a transition at finite disorder strength where the eigenstates of the system become localized, at least for the system sizes that are numerically accessible. However, there is currently no consensus on what would happen in the thermodynamic limit and what the exact nature (or existence) of the MBL transition is, as some authors argue that the critical disorder strength W^* scales with the system size and no transition exists at finite disorder in the thermodynamic limit [Šun+20; Kie+20; SP21].

In order to calculate the tripartite information, we need to deal with the doubled system $ABCD$ as described in Chapter 4. Hence the accessible system sizes are below those of other works, and we do not want to contribute to that ongoing debate and instead focus on the flow of information in finite systems. This more mesoscopic point of view might also be the more appropriate one when studying experimental realizations like quantum simulators and optical lattices or potential applications like qubit storage devices, which turns this bug into a feature.

The broader context of MBL is the thermalization of closed quantum systems, which is a concept that has garnered more interest recently because well-isolated quantum systems have become experimentally accessible, for example, in ultracold gas experiments, quantum simulators or nitrogen-vacancy centres in diamond [BR12; BDZ08; Doh+13; DM10; Dum+19; Kel+15; Lei+03; Sch+14; LGS15; Aba+19]. In contrast to open quantum systems, where a system coupled to a bath will usually thermalize to a GIBBS ensemble, closed quantum systems that are initialized in a pure state will stay pure under the unitary time evolution. Instead, large closed quantum systems are expected to serve as baths for their own subsystems, such that the expectation values of local observables approach the thermal expectation values of GIBBS states with the same energy density. The important *Eigenstate Thermalization Hypothesis* (ETH) predicts that even the eigenstates of the Hamiltonian can serve in this way [Deu91; Sre94; DAl+16], and in this sense, many closed quantum systems are expected to thermalize.

This rule does not apply to *integrable* systems that are instead expected to equilibrate – in the above sense – to *generalized Gibbs ensembles* that depend explicitly on the system's large number of integrals of motion. These systems tend not to be very robust as the integrability is often broken by small perturbations, at least when looking at the level statistics [Žni20].

The already mentioned systems with many-body localization are also claimed to fail to thermalize. Although there is interest in MBL in translation-invariant systems [MC17; PSA15; Smi+17; Yao+16], we will only consider disordered systems. In comparison to the systems where integrability is broken by small perturbations, MBL in these systems is also naturally robust against additional disorder.

One example of a model that has been well-studied numerically is the HEISENBERG chain, see Fig. 6.1, which is reprinted from Luitz, Laflorencie, and Alet [LLA15]. As the disorder strength increases, all eigenstates will eventually become localized, with a localization edge, where the localization depends on the energy density of the eigenstate, visible at intermediate values. The transition towards MBL can be seen in the energy levels of the

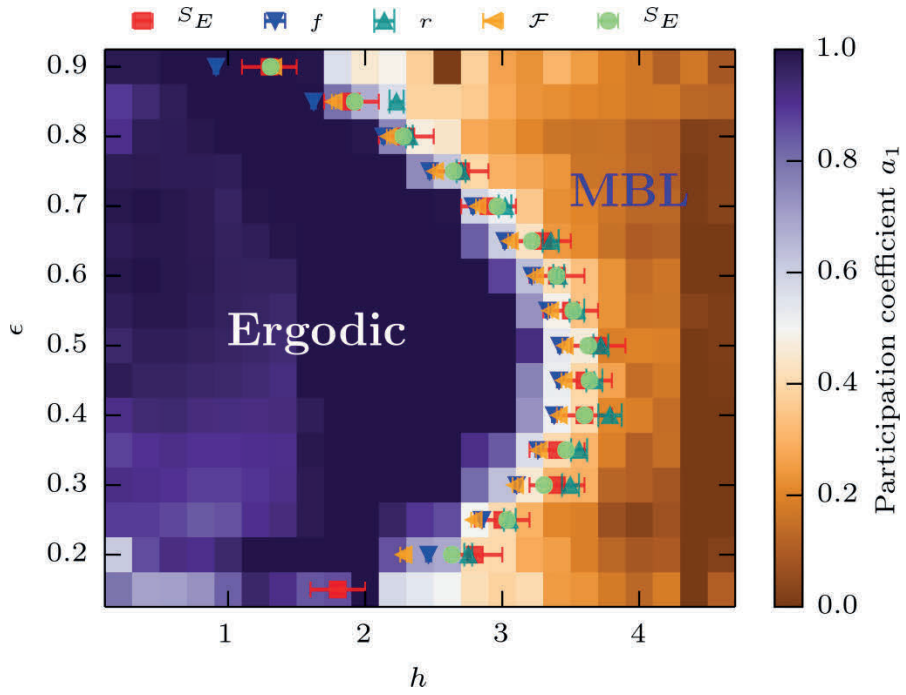

Figure 6.1: Many-body localization edge in the random-field Heisenberg chain. The phase diagram shows the energy density of the eigenstates ϵ against the disorder strength h, with the localization of the MBL transition extracted from finite-size scaling of systems up to $L = 22$. Taken from Luitz, Laflorencie, and Alet [LLA15], reprinted with permission from APS.

system, where level repulsion is replaced by a POISSON distribution, in the entanglement entropy, which changes from volume to area law, and in the Hilbert-space localization of eigenstates, where the scaling of the participation entropy changes its behaviour. We will use the same ratio of consecutive level spacings r as in the reference to compare to the tripartite information results.

There are also some experimental results, for example, in a one-dimensional optical lattice with quasi-random disorder, see Fig. 6.2 from Schreiber et al. [Sch+15]. The system is initialized with atoms only in the even-numbered sites of the optical lattice, and then the imbalance $I = \frac{N_e - N_o}{N_e + N_o}$ between the occupations N_e, N_o of the even and odd sites is used as an observable indicator for the presence of many-body localization: in the ergodic regime, the imbalance will relax from its large initial value to zero, while some signal of the initial state will remain in the localized regime.

From a more information-theoretic point of view, a smoking gun for the presence of MBL is

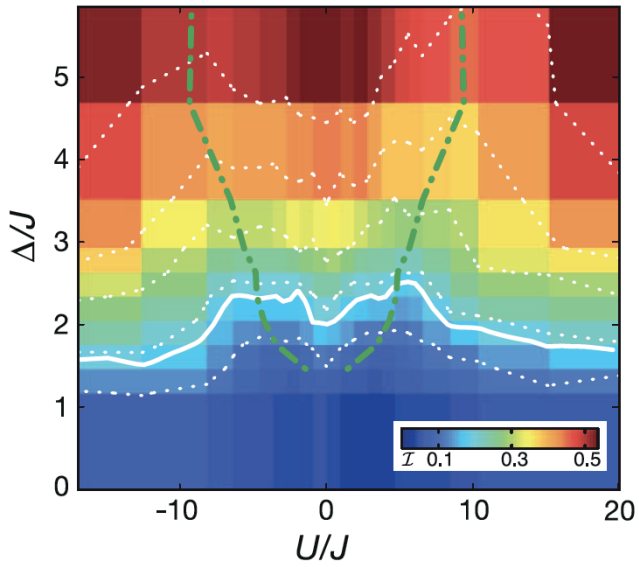

Figure 6.2: Static imbalance $\mathcal{I}$ as a diagnostic for localization in a plot of disorder strength Δ/J vs interaction strength U/J, taken from Schreiber et al. [Sch+15]. Reprinted with permission from AAAS.

the logarithmic growth of entanglement entropy after a quantum quench [ŽPP08; BPM12; SPA13; AES14; HHA21; Hua21]. Some of the results from the literature are shown in Fig. 6.3. Different entanglement witnesses have been used for these studies in addition to the venerable VON-NEUMANN entropy: the *quantum Fisher information* [BC94], the min-entropy of the one-particle reduced density matrix as well as a configurational correlator that measures the distance to a separable state $\rho_1 \otimes \rho_2$ [Luk+19].

We will be using the tripartite information to study how scrambling and MBL are connected. Both the input and output of our quantum channel are split into two subsystems, one of which is contiguous and rather small (between 1-3 lattice sites). The two small subsystems are called A and C, and their distance d is as shown in Fig. 6.4. Because the entanglement entropy after a quench only grows logarithmically in time, we expect that information travels very slowly in the MBL regime and should be able to see this explicitly using the tripartite information if we compare the timescale of information transport with the distance between the subsystems.

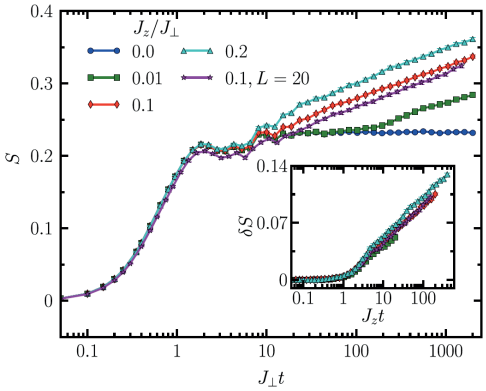

(a) Bardarson, Pollmann, and Moore [BPM12]

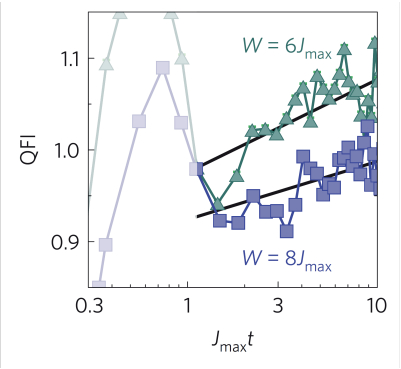

(b) Smith et al. [Smi+16]

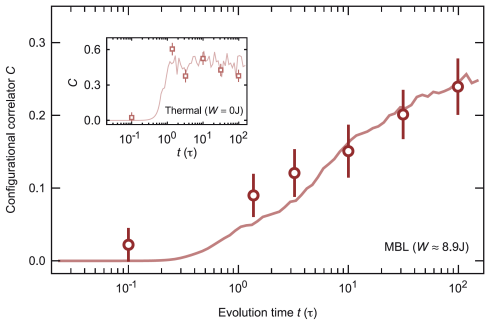

(c) Lukin et al. [Luk+19]

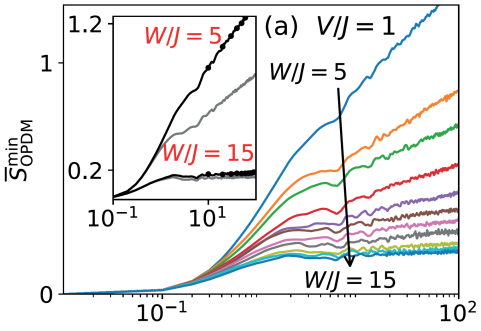

(d) Hopjan, Heidrich-Meisner, and Alba [HHA21]

Figure 6.3: Logarithmic growth of entanglement after a quench, taken from the source indicated below the image. Reprinted with permission from AAAS, APS and Springer Nature.

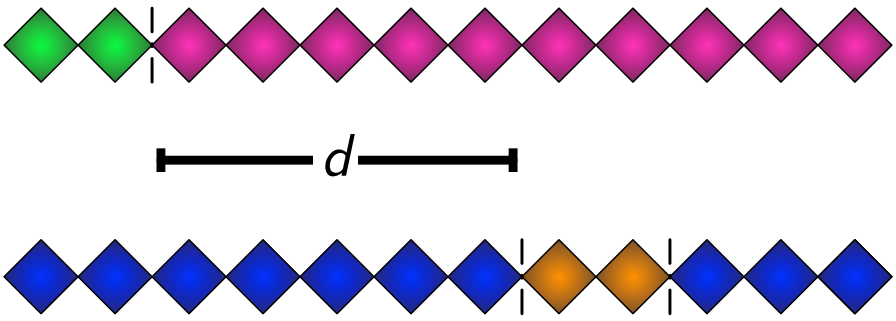

Figure 6.4: Illustration of the distance d between subsystems A and C. Figure 4 from Bölter and Kehrein [BK22b].

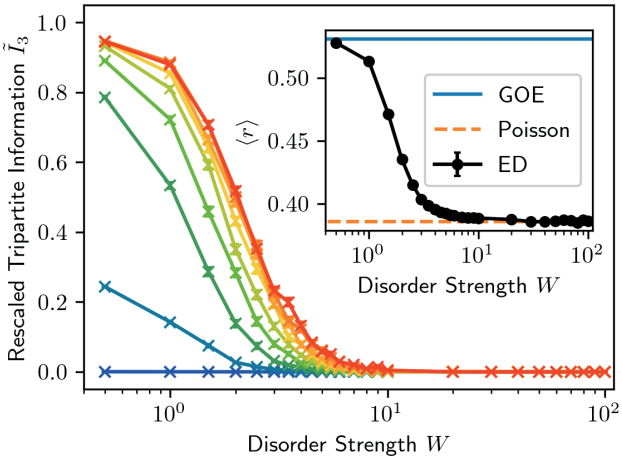

Figure 6.5: Comparison of the tripartite information between subsystems of size $\ell = 2$ at the opposite ends (cf. Fig. 6.4) of the isotropic Heisenberg chain ($\Delta = 1, L = 12$). The tripartite information is shown for different times $t = 4, 8, 16, 32, 64, 128, 256, 512, 1024$ from the bottom (blue) to the top (red). The inset shows the mean consecutive level spacing ratio $\langle r \rangle$ of the system's energy spectrum, which has been extensively studied in previous works and tracks the late-time behaviour of the tripartite information. Figure 5 from Bölter and Kehrein [BK22b].

6.2 Scrambling in the XXZ Chain

Our model system is the XXZ spin chain with open boundary conditions, which is described by the following Hamiltonian:

$$H = J\left(\sum_{i=1}^{L-1}\left(S_i^x S_{i+1}^x + S_i^y S_{i+1}^y + \Delta S_i^z S_{i+1}^z\right) - \sum_{i=1}^{L} h_i S_i^z\right) \tag{6.1}$$

As is tradition, we measure energy in units of J and introduce natural units by setting $J = 1$. The first sum in the equation for the Hamiltonian is – apart from the boundaries – a translation-invariant spin chain, which can be tuned to the non-interacting XX chain by setting $\Delta = 0$ and to the isotropic HEISENBERG point by setting $\Delta = 1$. The disorder is introduced by the second term, which is a static magnetic field in the z-direction that is different for every lattice site. The values h_i are independently and uniformly sampled from the box distribution $[-W, W]$. Because the limit $W = 0$ corresponds to the clean system and higher values increase the average difference between the magnetic field strength on neighbouring sites, we call W the *disorder strength*.

Following the literature, we restrict the Hilbert space from the full 2^L dimensional one to only the states with no net magnetization. This causes initial correlations in our system, as each microstate must have the magnetizations in the subsystems cancel exactly (e.g. if one partition of a bipartite system has a net magnetization of $-\frac{1}{2}$, the other one must have $+\frac{1}{2}$). Since the allowed states will still have identical probabilities, the initial subsystem entropies can simply be calculated by counting the states and some straightforward combinatorics, which yields the following equations:

$$\begin{aligned} S(L,\ell)_{t=0} &= -\sum_{n=0}^{\ell}\binom{\ell}{n} p(L,l,n)\log_2 p(L,l,n), \\ p(L,l,n) &= \binom{L-\ell}{L/2-n}\binom{L}{L/2}^{-1}, \end{aligned}$$

where $S(L,\ell)$ is the initial entropy of a subsystem of size ℓ in a system of total size L, with the size defined as the number of spins contained as before. We subtract these initial correlations – that are not due to the scrambling dynamics – from our results before plotting them, using the following equation:

$$\tilde{I}_3(t) = \frac{I_3(t) - I_3(0)}{I_3^{\text{Haar}} - I_3(0)}. \tag{6.2}$$

We are now ready to look at the behaviour of the rescaled tripartite information $\tilde{I}_3(t)$.

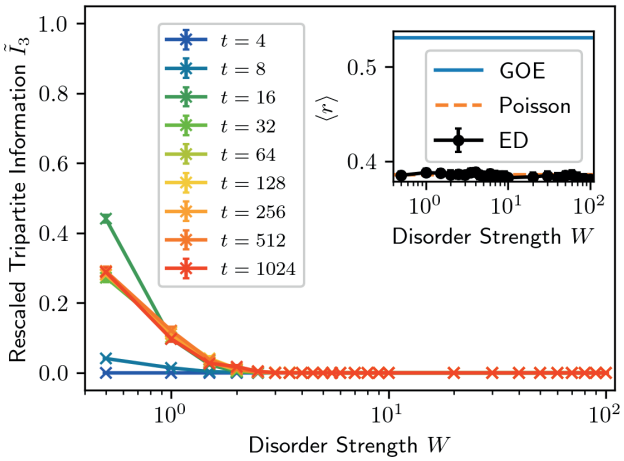

Figure 6.6: Comparison of the tripartite information in the non-interacting XX chain ($\Delta = 0, L = 12$) between subsystems of size $\ell = 2$ at the opposite ends (cf. Fig. 6.4). The value of $\tilde{I}_3$ is only above 0.4 for $t = 16$ at low disorder. The inset shows the mean consecutive level spacing ratio $\langle r \rangle$ of the system's energy spectrum. Figure 6 from Bölter and Kehrein [BK22b].

Before focussing on scrambling, we first compared the value of the tripartite information to an indirect measure of MBL already established in the literature, the mean consecutive level spacing ratio $\langle r \rangle$ [OH07; AL18], see Fig. 6.5. As the disorder is increased, the level statistics change from Wigner-Dyson to Poissonian together with the rescaled tripartite information at intermediate times up to $t = 1024$ that transitions in a similar fashion from close to the Haar scrambling value of unity to zero at the later times. For very short times, the information did not yet travel even through the clean system, so the scrambling cannot be seen yet. At these timescales, it looks like no information is transported at all at large disorder strengths ($W > 10$), however, since we expect very slow transport, we will study much later times as well.

We again need to consider the finite-size effects in our results, particularly as we have seen in the previous chapter how the tripartite information can converge to a value below the HAAR-averaged value for smaller systems. The finite-size data is shown in Fig. 6.8, where the converged late values of the tripartite information in systems with low disorder – where we expect effective scrambling to occur – are shown as a function of the inverse system size. The finite-size effects seem to become much stronger as the subsystem size is increased, so we used small subsystem sizes ℓ to get accurate results. It is worth noting

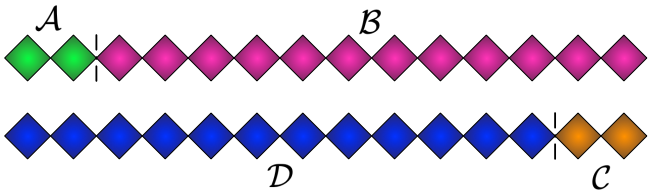

Figure 6.7: Subsystems at initial (top) and final (bottom) time. Each rhombus represents a spin-1/2 degree of freedom. Figure 2 from Bölter and Kehrein [BK22b].

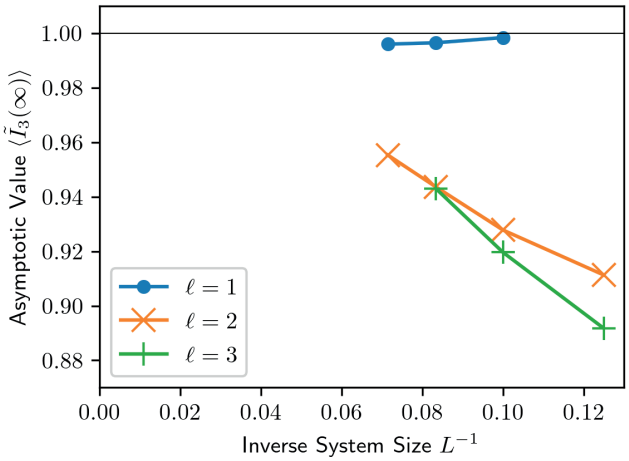

Figure 6.8: Highest asymptotic value of the rescaled tripartite information reached at late times for different system sizes L. The highest value is reached for low disorder strength W (cf. Fig. 6.5). Figure 7 from Bölter and Kehrein [BK22b].

that we additionally tested with subsystems A and C of unequal sizes, which also yields small finite-size effects in some cases. However, since we are interested in information transport, we choose very small subsystems such that the subsystem distance can be varied over a larger range (cf. Fig. 6.4), and more data can be collected on the spatial dependence. The data shows, though, as with the translation invariant system in Chapter 5, that the deviations from the HAAR-averaged value are consistent with finite-size effects.

We produced a movie showing the spreading of information in both the non-interacting XX chain with ANDERSON localization and the interacting Heisenberg chain with MBL, from which a screen capture can be seen in Fig. 6.9. The movies can be found in the supplemental material of Bölter and Kehrein [BK22b]. For low disorder strength, information

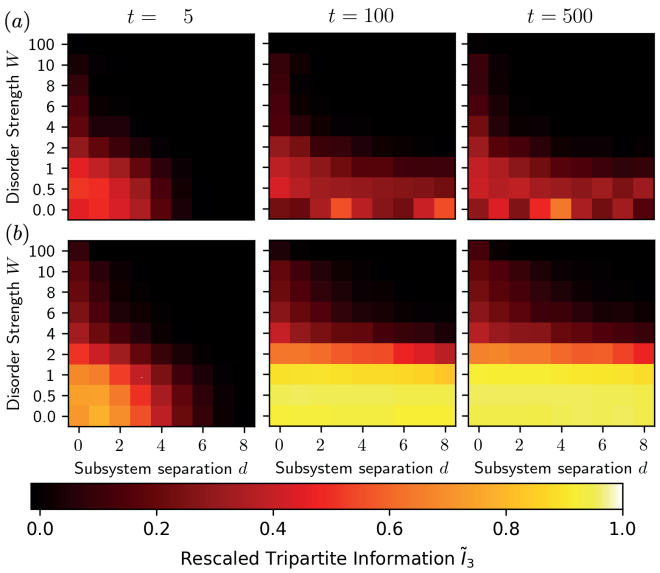

Figure 6.9: Spreading of information through (a) the XX chain ($\Delta = 0$) and (b) the isotropic Heisenberg chain ($\Delta = 1$) for different disorder strengths W at early and late times of the ballistic spreading. Here the small subsystems $\mathcal{A}$ and $\mathcal{C}$ are of size $\ell = 2$ and the system size is $L = 12$. Figure 8 from Bölter and Kehrein [BK22b].

is spreading in the non-interacting system, even though it should be entirely suppressed by Anderson localization. This is because the localization length scale in these cases is too large for our finite system size to capture. At stronger disorder strength, however, no information spreading can be observed. The non-interacting system is also not scrambling as even with low disorder strength, the tripartite information stays well below the Haar-averaged value, even if we consider the previously discussed finite-size effects. This is consistent with our previous results on translation-invariant systems in Section 5.1, where the tripartite information was fluctuating far below the Haar-averaged value in the non-interacting case.

For the interacting system, on the other hand, information is scrambled for low disorder strength, again consistent with our results in the previous chapter. For higher disorder strength the information seems to be spreading at a very slow speed through the system. However, data for much later times is required to confirm this.

To verify that information transport breaks down in the Anderson localized system, we plotted the tripartite information over a logarithmic timescale in Fig. 6.10. As the disorder strength is increased, the tripartite information stays at its initial value even for very long times of $t = 10^{12}$, indicating a complete breakdown of information transport. Because

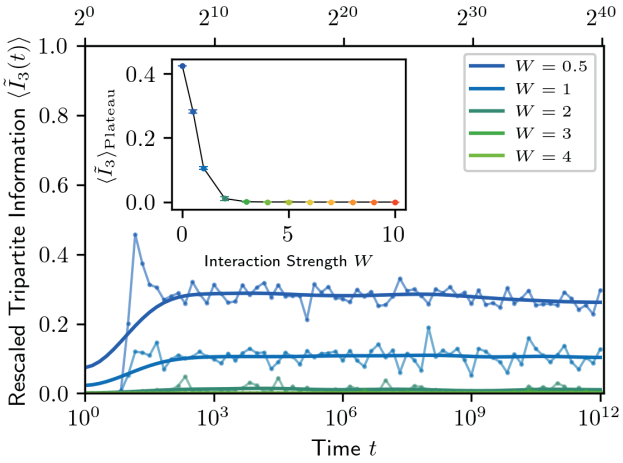

Figure 6.10: Spreading of information through the XX chain ($\Delta = 0, L = 12$) between two subsystems of size $\ell = 2$ at opposite ends. Because of the strong fluctuations a moving average (thick line) was added by convolution with a gaussian. The subset shows the height of the plateau, which was calculated by averaging data for intermediate times $10^3 \leq t \leq 10^{10}$. Figure 9 from Bölter and Kehrein [BK22b].

of the numerical precision used[1], the calculation must break down before $t = 2^{52}$, as the finite numerical precision of the energy eigenvalues E_n will start to cause large errors in the time evolution factor e^{-itE_n}. Accordingly, a sudden rise in the tripartite information to its HAAR value independent of disorder strength for very late times can be observed, which we deem to be a highly unphysical effect of the finite numerical precision. Hence we are cutting off the data well before this regime at about $t = 2^{40}$. This behaviour was not observed in the interacting system until much later times, but we still used the same cutoff to ensure the data is reliable. The complete breakdown of scrambling in the data is an indicator of ANDERSON localization as expected.

We now switch to the interacting system – the Heisenberg chain – which is known to show indications of MBL [AL18]. The corresponding plot is shown in Fig. 6.11, where it is clear that the tripartite information now reaches a non-vanishing plateau value even for large disorder strength, on a timescale that becomes exponentially large in the travel distance for higher disorder strength. We fitted logistic functions to the data to find out the timescale T and the plateau value $I_3(\infty)$, which will be analysed in the following.

In Fig. 6.12, we see how the plateau value that the tripartite information reaches after a

[1] A 64 bit IEEE 754 floating point number with 52 mantissa bits [IEEE19].

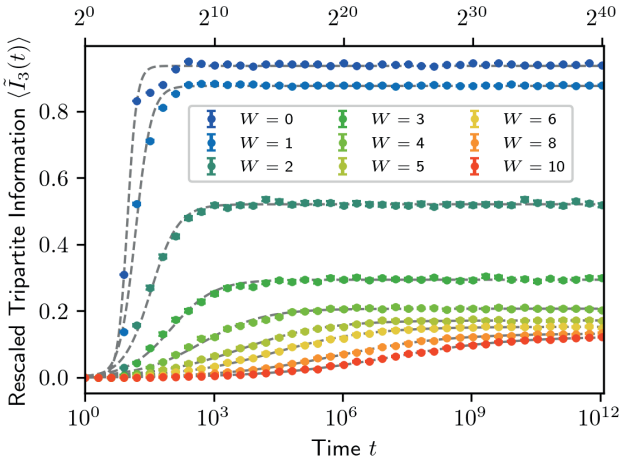

Figure 6.11: Spreading of information through the isotropic Heisenberg chain ($\Delta = 1, L = 12$) between two subsystems of size $\ell = 2$ at opposite ends. The dashed lines are fits against a logistic function, see main text. Figure 10 from Bölter and Kehrein [BK22b].

very long time is suppressed by the disorder. Not only the speed but also the amplitude of the information signal is affected by the disorder.

In Fig. 6.13, we additionally see how information is getting stuck in the system, as the amplitude is reduced with larger subsystem separation.

Next, we look at the timescale on which the signal arrives, which we estimate by the arrival time T at which I_3 has reached half of its plateau value. The signal is travelling inside a lightcone that is growing logarithmically slowly. A picture of the lightcone can be seen in Fig. 6.14.

The arrival time itself is shown in Figs. 6.15 & 6.16, where we see that it depends exponentially on both the distance and the disorder strength. In Fig. 6.16, it is noticeable that the lightcone spreads on very similar timescales for different system sizes, apart from when it hits the boundary of the system, where it seems to speed up as the last data points on the lines are shifted downward. This can be intuitively understood, as the information signal is reflected at the boundary, which will cause the tripartite information to grow more quickly for the system layout where the subsystem C is at the edge of the system.

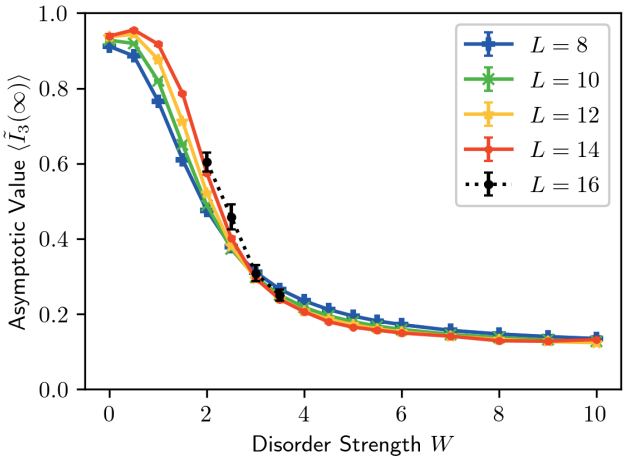

Figure 6.12: Asymptotic value at late times of the rescaled tripartite information $\tilde{I}_3(t)$ between two subsystems of size $\ell = 2$ at opposite ends of the isotropic Heisenberg chain ($\Delta = 1$). Here the system size is varied while d is fixed at the maximum value $d = L - 2\ell$. See Fig. 6.13 for results with varying subsystem separation. Figure 11 from Bölter and Kehrein [BK22b].

6.2.1 Different Subsystem Sizes

We also changed the subsystem size to $\ell = 1$ or $\ell = 3$, where the results are very similar to those in the main part with the subsystem size $\ell = 2$. The tripartite information still reaches a plateau value on some timescale (cf Fig. 6.17), where the asymptotic value is suppressed by disorder (cf Fig. 6.18), and the arrival time is still exponentially large in the distance and the disorder strength (cf. Fig. 6.19).

As we had alluded to earlier, the finite-size effects are smaller when the subsystem size ℓ is decreased since the value of the tripartite information actually gets much closer to both the Haar limit and zero in the limit of high or low disorder strength for the case of the subsystem C only containing one lattice site. In order to suppress the finite fize effects, it seems reasonable that not only should the smaller subsystem be much smaller than the total system, but also much smaller than the remainder of the system, i.e. $\ell \ll L - \ell$.

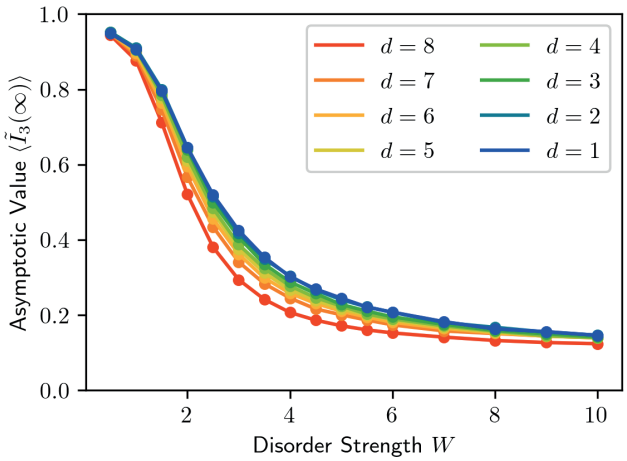

Figure 6.13: Asymptotic value at late times of the rescaled tripartite information $\tilde{I}_3(t)$ between two subsystems of size $\ell = 2$ of the isotropic Heisenberg chain ($\Delta = 1$). Here the subsystem separation is varied with $L = 12$ fixed, in contrast to the previous figure. Figure 12 from Bölter and Kehrein [BK22b].

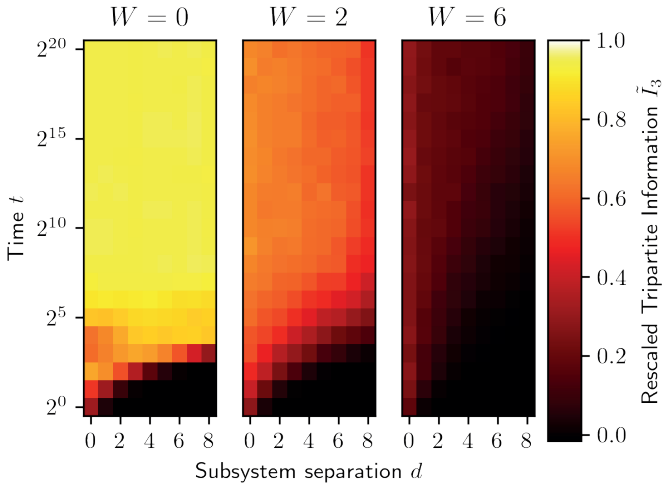

Figure 6.14: Dynamics of the tripartite information I_3 in the space-time plane with subsystems of size $\ell = 2$ in the isotropic Heisenberg chain ($\Delta = 1, \ell = 12$). In the strongly disordered system ($W = 6$), the spreading of information takes an exponentially long time. Figure 13 from Bölter and Kehrein [BK22b].

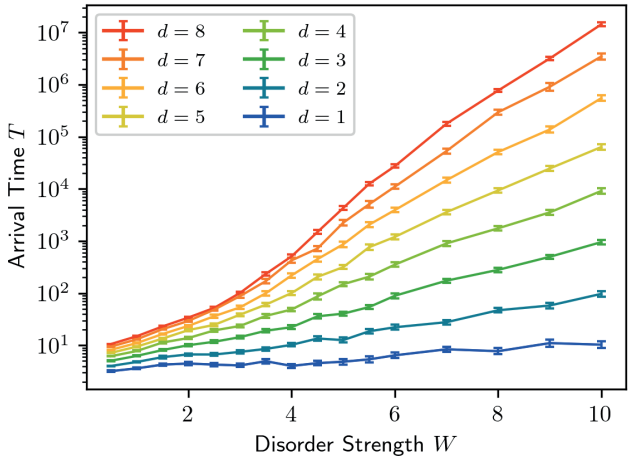

Figure 6.15: Arrival time of the information between two subsystems of size $\ell = 2$ of the isotropic Heisenberg chain ($\Delta = 1$) across a distance of d spins. We again vary the subsystem separation d for a fixed system size $L = 12$, a comparison of different system sizes can be found in Fig. 6.16. Figure 14 from Bölter and Kehrein [BK22b].

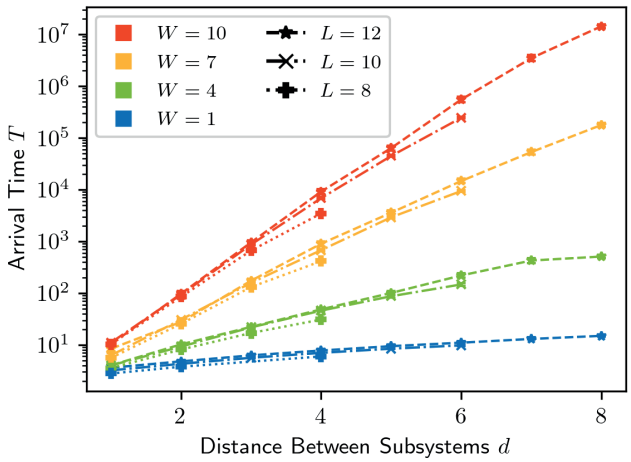

Figure 6.16: Arrival time of the information between two subsystems of size $\ell = 2$ of the isotropic Heisenberg chain ($\Delta = 1$) across a distance of d spins. Figure 15 from Bölter and Kehrein [BK22b].

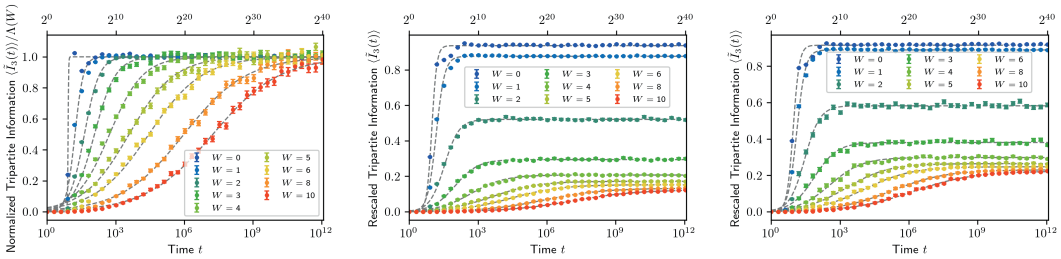

(a) $\ell = 1$ **(b)** $\ell = 2$ **(c)** $\ell = 3$

Figure 6.17: Spreading of information through the isotropic Heisenberg chain ($\Delta = 1, L = 12$) between two subsystems at opposite ends. The values in Fig. 6.17a were normalized because the step becomes very small for higher disorder strength W and is hard to see otherwise. Figure 16 from Bölter and Kehrein [BK22b].

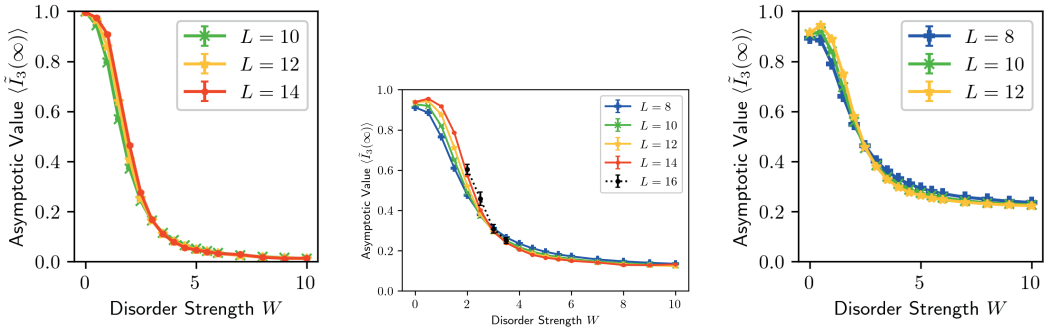

(a) $\ell = 1$ **(b)** $\ell = 2$ **(c)** $\ell = 3$

Figure 6.18: Asymptotic value of tripartite information between two subsystems at opposite ends of the isotropic Heisenberg chain ($\Delta = 1$). Figure 17 from Bölter and Kehrein [BK22b].

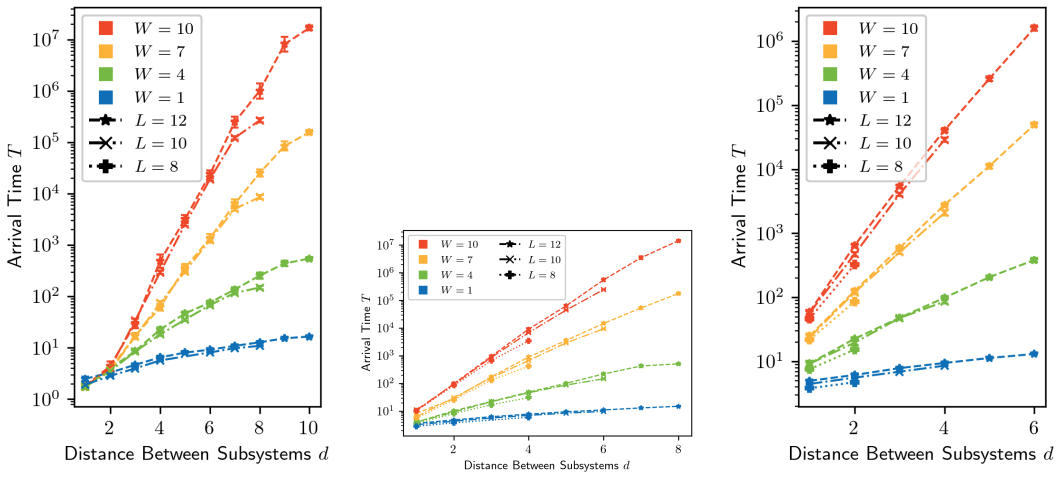

(a) $\ell = 1$ **(b)** $\ell = 2$ **(c)** $\ell = 3$

Figure 6.19: Arrival time of the information between two subsystems of the isotropic Heisenberg chain ($\Delta = 1$) across a distance of d spins. Figure 18 from Bölter and Kehrein [BK22b].

6.3 Transverse Field Ising Model

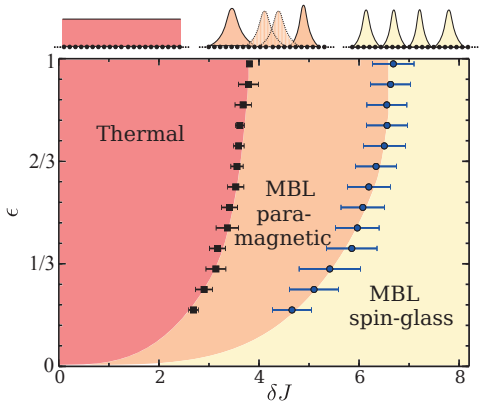

Figure 6.20: Phase diagram of the disordered Ising chain where ϵ is the energy density compared to the total bandwidth ($\epsilon = 1$ in the exact centre of the band) and δJ the disorder strength. Taken from Kjäll, Bardarson, and Pollmann [KBP14]. Reprinted with permission from APS.

We also studied another MBL model, the disordered transverse field Ising chain, which had already been studied in Kjäll, Bardarson, and Pollmann [KBP14]. There it was found that, as the disorder is increased, it first undergoes the MBL transition and then another transition from paramagnetic to spin-glass, as shown in Fig. 6.20. In the spin-glass phase, the order parameter

$$\chi_n^{\mathrm{SG}} = \frac{1}{L}\sum_{i,j=1}^{L} \langle n|\sigma_i^z\sigma_j^z|n\rangle^2 \tag{6.3}$$

diverges proportional to the system size in the thermodynamic limit [KBP14].

The Hamiltonian of the model is the following:

$$H = -\sum_{i=1}^{L-1} J_i\sigma_i^z\sigma_{i+1}^z + J_2\sum_{i=1}^{L-2}\sigma_i^z\sigma_{i+2}^z + h\sum_{i=1}^{L}\sigma_i^x, \tag{6.4}$$

where the nearest neighbour couplings J_i are now randomly selected from $[J-W, J+W]$. We also set $J = 1, J_2 = h/2 = 0.3$ in agreement with Kjäll, Bardarson, and Pollmann [KBP14]. In the previous section, we had a random magnetic field that only affected individual sites, but the disorder, in this case, is in the couplings between neighbouring sites, which will have significant consequences. Unlike the previous spin chain, the Ising model does not have conservation of net magnetization, so this time we are using the full 2^L dimensional Hilbert space, and the tripartite information vanishes initially (see Section 3.2).

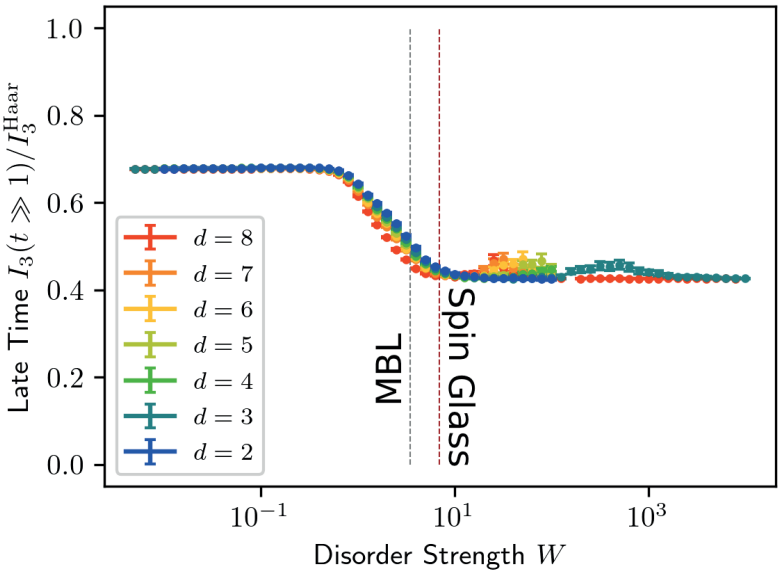

Figure 6.21: Asymptotic value at late times of the rescaled tripartite information $\tilde{I}_3(t)$ between two subsystems of size $\ell = 2$ at opposite ends of the transverse field ISING model. The dashed lines correspond approximately to the two transitions shown in the phase diagram in Fig. 6.20.

The value of the tripartite information at late times is shown in Fig. 6.21, where we can clearly distinguish two plateaus at low and high disorder strength. Unlike in the previous case, the spins in the system do not freeze out completely in the limit of infinite disorder, as the disorder is now in the couplings. Strongly coupled spins can flip synchronously without paying the associated large energy cost, which leaves open degrees of freedom that can transport information through the system. This could explain how the tripartite information converges to a value much higher than its initial value even for strong disorder, in contrast to the previously studied XXZ-chain. Unfortunately, the transition of the asymptotic value is quite broad, and it is impossible to identify two separate phase transitions. To get data with a sharper transition that could be more clearly associated with one or both of the phase transitions, it would be beneficial to restrict the system to a small energy window and access larger system sizes, which we have not done so far.

In Fig. 6.22, the arrival time of the information signal is shown, where we see that we get similar behaviour to the Heisenberg spin chain as the transport is exponentially slowed down when the disorder is increased, which is a signal of the MBL transition.

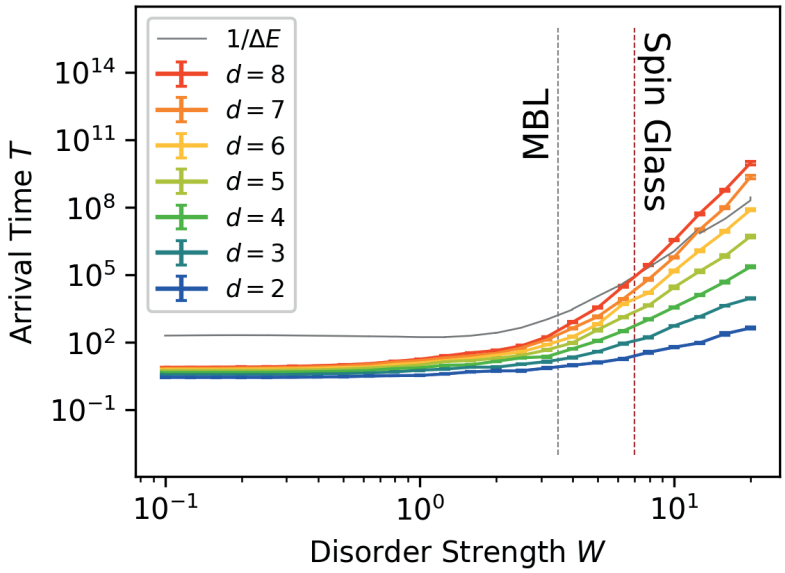

Figure 6.22: Arrival time of the information between two subsystems of size $\ell = 2$ at opposite ends of the transverse field Ising model. The dashed lines correspond approximately to the two transitions shown in the phase diagram in Fig. 6.20.

As seen in Huse et al. [Hus+13], there is supposedly an additional spectral transition at high disorder strength, where a paired spectrum emerges. We rather optimistically calculated data up to very large disorder strengths to investigate this and ran into the problem that the energy differences $\Delta E_n = (E_{n+1} - E_n)$ between the paired states became too small for the numerical precision, with the spurious effect that it eventually became independent of the disorder strength. This, however, is just a numerical artefact and is not shown in the data, which has been cut off at reasonable values of the disorder strength that do not cause this problem.

The results in this section are currently in preparation for publication.

Chapter 7

Discussion

The topic of this thesis is the transport of information in one-dimensional quantum many-body systems. For that purpose we studied scrambling, that is the delocalization of initially localized information, in closed quantum systems undergoing unitary time evolution, using the observable-independent tripartite information I_3. Because of the required purification of the quantum state and its associated doubling of the effective system size our studies were limited to a total number of 16 qubits. We also performed an analytical calculation of the tripartite information in qubit systems, which, however, yielded only limited results since we could only calculate the early-time behaviour of the tripartite information in second order in time for non-interacting spinless fermions and hard-core bosons.

On the numerical side of the project, we could successfully observe the transport of information in disorder-free systems in Chapter 5, which is akin to the hydrodynamic spreading of out-of-time-order correlation functions, that is a wavefront that spreads through the system ballistically with a butterfly velocity v_B. The wavefront is initially very steep, but then over time t gets diffusively broadened proportional to $\sqrt{t}$.

We then looked at disordered systems in Chapter 6, specifically systems that have a localization transition when disorder is introduced. For the non-interacting XX chain, we could see the Anderson localization as the information transport is completely suppressed. For the interacting Heisenberg chain the transition from ergodic to many-body-localized could also clearly be observed since after the transition, the information transport is partially suppressed in amplitude and becomes exponentially slow, as the information signal spreads inside a lightcone that is now only growing logarithmically in time.

There are also related works that use the tripartite information, for example, Sun, Cui,

and Fan [SCF21] that has a very different system layout in which all but one of the qubits are time evolved [IS18], but stresses the potential experimental realization using quantum state tomography. Also, there are some interesting analytical results in Sünderhauf et al. [Sün+19] where they found the tripartite information of the second Rényi order for the so-called *Brownian SYK Model*, which is a simplification of the SYK model that allows the calculation to be done at finite values of N [SY93; SSS19]. Much more closely aligned with our approach are the works Kuno, Orito, and Ichinose [KOI22] and Orito, Kuno, and Ichinose [OKI22] since they use the same layout of the partitions A, B, C, and D, for example, studying disorder-free spin chains with multiple-spin interactions and finding a phase-transition-like behaviour in the late-time value of the tripartite information as integrability is broken. This nicely complements our earlier results on the same observable in spinless fermion systems in Chapter 5.

In the introduction, we presented the tripartite information together with two other methods of diagnosing information transport, namely the entanglement entropy after a quantum quench and the out-of-time-order correlation functions. The advantage of the tripartite information is that it has a spatial resolution similar to the correlation functions, where the spreading of the signal, for example, over individual lattice sites can be studied, but is also observable-independent, similar to the entanglement entropy and other information-theoretic quantities. However, there are also some clear disadvantages to this approach: because the method fundamentally relies on describing the physical system AB using an infinite-temperature state, the effective system size compared to a pure-state description doubles, which wreaks havoc with the numerically accessible system sizes, as the space and time complexity of the numerical calculation depends exponentially on the now doubled effective system size $2L$. Furthermore, we could not find any analytical results for the tripartite information beyond the short-time limit, which would be outright required to diagnose scrambling behaviour analytically. Maybe a conformal field theory approach, which has been successfull already to calculate entanglement entropies in one spatial dimension [CC09], could be used.

Key factors for our results were the independent implementations by Oskar Schnaack and Sebastian Paeckel for the calculation of the tripartite information that were used to verify the numerical results. It should be pointed out that the code we created is quite generic and can calculate the tripartite information (and its Haar-averaged value) for arbitrary Hamiltonians and system partitionings in terms of size, position, and contiguity of both the input and the output subsystems, and the state can also be constructed using arbitrary temperature or chemical potential. Because of this it can also serve in future research projects and

for this purpose we provided a comprehensive overview of the numerical implementation in Chapter 4. The output data is optimized for high-throughput data aggregation on high-performance compute clusters, and all generated cached or raw data are checksummed to prevent data corruption.

As we have used it so far, the tripartite information has no energy resolution, as we used the maximally entangled state that corresponds to an infinite temperature in the physical subsystems AB and CD throughout. This was caused by the unavailability of a replacement for the HAAR-averaged value at finite temperatures. Without energy resolution, only transitions that affect all the eigenstates at a similar parameter range can be sharply observed in the tripartite information, while transitions depending on a small selection of states are washed out. Future work could definitely look at intermediate and low-temperature scrambling if such a comparison value could be established. In particular an efficient implementation of the method that includes a restriction to a finite window of the system's spectrum could greatly improve the situation in terms of the energy resolution. A further direction of interest is the analytical calculation of the tripartite information and also the generalization to two- and three-dimensional systems. Exciting new physics – akin to the fractional quantum hall effect [KDP80; TSG82; Lau83] – might be lurking in higher dimensions!

Bibliography

[AB08] Dorit Aharonov and Michael Ben-Or. "Fault-Tolerant Quantum Computation with Constant Error Rate." In: *SIAM Journal on Computing* 38.4 (Jan. 2008), pp. 1207–1282. ISSN: 0097-5397. https://doi.org/10.1137/S0097539799359385.

[Aba+19] Dmitry A. Abanin et al. "Colloquium: Many-body Localization, Thermalization, and Entanglement." In: *Reviews of Modern Physics* 91.2 (May 22, 2019), p. 021001. https://doi.org/10.1103/RevModPhys.91.021001.

[AES14] Felix Andraschko, Tilman Enss, and Jesko Sirker. "Purification and Many-Body Localization in Cold Atomic Gases." In: *Physical Review Letters* 113.21 (Nov. 17, 2014), p. 217201. https://doi.org/10.1103/PhysRevLett.113.217201.

[AGS12] Gerardo Adesso, Davide Girolami, and Alessio Serafini. "Measuring Gaussian Quantum Information and Correlations Using the Rényi Entropy of Order 2." In: *Physical Review Letters* 109.19 (Nov. 9, 2012), p. 190502. https://doi.org/10.1103/PhysRevLett.109.190502.

[AL18] Fabien Alet and Nicolas Laflorencie. "Many-Body Localization: An Introduction and Selected Topics." In: *Comptes Rendus Physique* 19.6 (Sept. 2018), pp. 498–525. ISSN: 16310705. https://doi.org/10.1016/j.crhy.2018.03.003.

[AMD20] AMD. *Software Optimization Guide for AMD EPYC™ 7003 Processors*. Oct. 2020. URL: https://www.amd.com/system/files/TechDocs/56665.zip.

[And+99] E. Anderson et al. *LAPACK Users' Guide*. 3rd ed. Philadelphia, PA: Society for Industrial and Applied Mathematics, 1999. ISBN: 0-89871-447-8 (paperback).

[And58] P. W. Anderson. “Absence of Diffusion in Certain Random Lattices.” In: *Physical Review* 109.5 (Mar. 1, 1958), pp. 1492–1505. https://doi.org/10.1103/PhysRev.109.1492.

[BAA06] D. M. Basko, I. L. Aleiner, and B. L. Altshuler. “Metal–Insulator Transition in a Weakly Interacting Many-Electron System with Localized Single-Particle States.” In: *Annals of Physics* 321.5 (May 1, 2006), pp. 1126–1205. ISSN: 0003-4916. https://doi.org/10.1016/j.aop.2005.11.014.

[BB84] CH Bennett and Gilles Brassard. “Quantum Cryptography: Public Key Distribution and Coin Tossing Int.” In: *Conf. on Computers, Systems and Signal Processing (Bangalore, India)*. Vol. 175. 1984. https://doi.org/10.1016/j.tcs.2014.05.025.

[BC94] Samuel L. Braunstein and Carlton M. Caves. “Statistical Distance and the Geometry of Quantum States.” In: *Physical Review Letters* 72.22 (May 30, 1994), pp. 3439–3443. https://doi.org/10.1103/PhysRevLett.72.3439.

[BDZ08] Immanuel Bloch, Jean Dalibard, and Wilhelm Zwerger. “Many-Body Physics with Ultracold Gases.” In: *Reviews of Modern Physics* 80.3 (July 18, 2008), pp. 885–964. https://doi.org/10.1103/RevModPhys.80.885.

[Bel11] Steven M. Bellovin. “Frank Miller: Inventor of the One-Time Pad.” In: *Cryptologia* 35.3 (July 1, 2011), pp. 203–222. ISSN: 0161-1194. https://doi.org/10.1080/01611194.2011.583711.

[Bel64] J. S. Bell. “On the Einstein Podolsky Rosen Paradox.” In: *Physics Physique Fizika* 1.3 (Nov. 1, 1964), pp. 195–200. https://doi.org/10.1103/PhysicsPhysiqueFizika.1.195.

[Ben80] Paul Benioff. “The Computer as a Physical System: A Microscopic Quantum Mechanical Hamiltonian Model of Computers as Represented by Turing Machines.” In: *Journal of Statistical Physics* 22.5 (1980), pp. 563–591. https://doi.org/10.1007/BF01011339.

[Ber+17] Daniel J. Bernstein et al. *Post-Quantum RSA*. Cryptology ePrint Archive, Paper 2017/351. 2017. URL: https://eprint.iacr.org/2017/351.

[Bet31] H. Bethe. “Zur Theorie der Metalle.” In: *Zeitschrift für Physik* 71.3 (Mar. 1, 1931), pp. 205–226. ISSN: 0044-3328. https://doi.org/10.1007/BF01341708.

[BK22a] Niklas Bölter and Stefan Kehrein. *Replication Data for: Phys. Rev. B 105, 104202*. Version V1. GRO.data, 2022. https://doi.org/10.25625/D76S79.

[BK22b] Niklas Bölter and Stefan Kehrein. “Scrambling and Many-Body Localization in the XXZ Chain.” In: *Physical Review B* 105.10 (Mar. 8, 2022), p. 104202. https://doi.org/10.1103/PhysRevB.105.104202.

[Blo29] Felix Bloch. “Über die Quantenmechanik der Elektronen in Kristallgittern.” In: *Zeitschrift für Physik* 52.7 (July 1, 1929), pp. 555–600. ISSN: 0044-3328. https://doi.org/10.1007/BF01339455.

[BM58] G. E. P. Box and Mervin E. Muller. “A Note on the Generation of Random Normal Deviates.” In: *The Annals of Mathematical Statistics* 29.2 (June 1958), pp. 610–611. ISSN: 0003-4851, 2168-8990. https://doi.org/10.1214/aoms/1177706645.

[BPM12] Jens H. Bardarson, Frank Pollmann, and Joel E. Moore. “Unbounded Growth of Entanglement in Models of Many-Body Localization.” In: *Physical Review Letters* 109.1 (July 3, 2012), p. 017202. https://doi.org/10.1103/PhysRevLett.109.017202.

[BR12] R. Blatt and C. F. Roos. “Quantum Simulations with Trapped Ions.” In: *Nature Physics* 8.4 (4 Apr. 2012), pp. 277–284. ISSN: 1745-2481. https://doi.org/10.1038/nphys2252.

[Bro+81] T. A. Brody et al. “Random-Matrix Physics: Spectrum and Strength Fluctuations.” In: *Reviews of Modern Physics* 53.3 (July 1, 1981), pp. 385–479. https://doi.org/10.1103/RevModPhys.53.385.

[BSW15] Mario Berta, Kaushik P. Seshadreesan, and Mark M. Wilde. “Rényi Generalizations of the Conditional Quantum Mutual Information.” In: *Journal of Mathematical Physics* 56.2 (Feb. 23, 2015), p. 022205. ISSN: 0022-2488. https://doi.org/10.1063/1.4908102.

[CC09] Pasquale Calabrese and John Cardy. “Entanglement Entropy and Conformal Field Theory.” In: *Journal of Physics A: Mathematical and Theoretical* 42.50 (Dec. 18,

2009), p. 504005. ISSN: 1751-8113, 1751-8121. https://doi.org/10.1088/1751-8113/42/50/504005.

[Chi+22] B. Chiaro et al. “Direct Measurement of Nonlocal Interactions in the Many-Body Localized Phase.” In: *Physical Review Research* 4.1 (Feb. 22, 2022), p. 013148. https://doi.org/10.1103/PhysRevResearch.4.013148.

[CKW00] Valerie Coffman, Joydip Kundu, and William K. Wootters. “Distributed Entanglement.” In: *Physical Review A* 61.5 (Apr. 10, 2000), p. 052306. https://doi.org/10.1103/PhysRevA.61.052306.

[CP22] Shira Chapman and Giuseppe Policastro. “Quantum Computational Complexity from Quantum Information to Black Holes and Back.” In: *The European Physical Journal C* 82.2 (Feb. 10, 2022), p. 128. ISSN: 1434-6052. https://doi.org/10.1140/epjc/s10052-022-10037-1.

[CS14] Scott Chacon and Ben Straub. *Pro Git*. 2nd ed. USA: Apress, 2014. ISBN: 1-4842-0077-2. https://doi.org/10.1007/978-1-4842-0076-6.

[CST12] U.S. Department of Commerce, National Institute of Standards, and Technology. *Secure Hash Standard - SHS: Federal Information Processing Standards Publication 180-4*. North Charleston, SC, USA: National Institute of Standards and Technology, 2012. ISBN: 1-4781-7807-8. https://doi.org/10.6028/NIST.FIPS.180-4.

[DAl+16] Luca D’Alessio et al. “From Quantum Chaos and Eigenstate Thermalization to Statistical Mechanics and Thermodynamics.” In: *Advances in Physics* 65.3 (May 3, 2016), pp. 239–362. ISSN: 0001-8732, 1460-6976. https://doi.org/10.1080/00018732.2016.1198134.

[Dal+22] Andrew J. Daley et al. “Practical Quantum Advantage in Quantum Simulation.” In: *Nature* 607.7920 (7920 July 2022), pp. 667–676. ISSN: 1476-4687. https://doi.org/10.1038/s41586-022-04940-6.

[Das+06] Arnab Das et al. “Infinite-Range Ising Ferromagnet in a Time-Dependent Transverse Magnetic Field: Quench and Ac Dynamics near the Quantum Critical Point.” In: *Physical Review B* 74.14 (Oct. 24, 2006). ISSN: 1098-0121, 1550-235X. https://doi.org/10.1103/PhysRevB.74.144423.

[Deu91] J. M. Deutsch. “Quantum Statistical Mechanics in a Closed System.” In: *Physical Review A* 43.4 (Feb. 1, 1991), pp. 2046–2049. https://doi.org/10.1103/PhysRevA.43.2046.

[DM10] L.-M. Duan and C. Monroe. “Colloquium: Quantum Networks with Trapped Ions.” In: *Reviews of Modern Physics* 82.2 (Apr. 28, 2010), pp. 1209–1224. https://doi.org/10.1103/RevModPhys.82.1209.

[Doh+13] Marcus W. Doherty et al. “The Nitrogen-Vacancy Colour Centre in Diamond.” In: *Physics Reports* 528.1 (July 1, 2013), pp. 1–45. ISSN: 0370-1573. https://doi.org/10.1016/j.physrep.2013.02.001.

[DR02] Joan Daemen and Vincent Rijmen. *The Design of Rijndael: AES — the Advanced Encryption Standard*. Springer-Verlag, 2002, p. 238. ISBN: 3-540-42580-2. https://doi.org/10.1007/978-3-662-04722-4.

[Dum+19] Philipp T. Dumitrescu et al. “Kosterlitz-Thouless Scaling at Many-Body Localization Phase Transitions.” In: *Physical Review B* 99.9 (Mar. 22, 2019), p. 094205. https://doi.org/10.1103/PhysRevB.99.094205.

[Eke91] Artur K. Ekert. “Quantum Cryptography Based on Bell’s Theorem.” In: *Physical Review Letters* 67.6 (Aug. 5, 1991), pp. 661–663. ISSN: 0031-9007. https://doi.org/10.1103/PhysRevLett.67.661.

[Fey82] Richard P. Feynman. “Simulating Physics with Computers.” In: *International Journal of Theoretical Physics* 21.6 (June 1, 1982), pp. 467–488. ISSN: 1572-9575. https://doi.org/10.1007/BF02650179.

[Gau61] Michel Gaudin. “Sur La Loi Limite de l’espacement Des Valeurs Propres d’une Matrice Ale′atoire.” In: *Nuclear Physics* 25 (May 1, 1961), pp. 447–458. ISSN: 0029-5582. https://doi.org/10.1016/0029-5582(61)90176-6.

[GMP05] I. V. Gornyi, A. D. Mirlin, and D. G. Polyakov. “Interacting Electrons in Disordered Wires: Anderson Localization and Low-T Transport.” In: *Physical Review Letters* 95.20 (Nov. 8, 2005), p. 206603. https://doi.org/10.1103/PhysRevLett.95.206603.

[GMW98] Thomas Guhr, Axel Müller–Groeling, and Hans A. Weidenmüller. “Random Matrix Theories in Quantum Physics: Common Concepts.” In: *Physics Reports*

299.4 (June 1, 1998), pp. 189–425. ISSN: 0370-1573. https://doi.org/10.1016/S0370-1573(97)00088-4.

[GoeGrid] *The Grid Resource Centre in Göttingen: GoeGrid.* URL: http://goegrid.de/.

[Got98] Daniel Gottesman. "Theory of Fault-Tolerant Quantum Computation." In: *Physical Review A* 57.1 (Jan. 1, 1998), pp. 127–137. https://doi.org/10.1103/PhysRevA.57.127.

[Gro01] Lov K. Grover. "From Schrödinger's Equation to the Quantum Search Algorithm." In: *Pramana* 56.2-3 (Feb. 2001), pp. 333–348. ISSN: 0304-4289, 0973-7111. https://doi.org/10.1007/s12043-001-0128-3.

[Gro96] Lov K. Grover. *A Fast Quantum Mechanical Algorithm for Database Search.* Nov. 19, 1996. https://doi.org/10.48550/arXiv.quant-ph/9605043. preprint.

[GV59] M. E. Gertsenshtein and V. B. Vasil'ev. "Waveguides with Random Inhomogeneities and Brownian Motion In the Lobachevsky Plane." In: *Theory of Probability & Its Applications* 4.4 (Jan. 1959), pp. 391–398. ISSN: 0040-585X. https://doi.org/10.1137/1104038.

[GW14] Geoffrey Grimmett and D. J. A. Welsh. *Probability: An Introduction.* Second edition. Oxford: Oxford University, 2014. 270 pp. ISBN: 978-0-19-870997-8.

[Har28] R. V. L. Hartley. "Transmission of Information." In: *Bell System Technical Journal* 7.3 (1928), pp. 535–563. ISSN: 1538-7305. https://doi.org/10.1002/j.1538-7305.1928.tb01236.x.

[Haw74] S. W. Hawking. "Black Hole Explosions?" In: *Nature* 248.5443 (5443 Mar. 1974), pp. 30–31. ISSN: 1476-4687. https://doi.org/10.1038/248030a0.

[Haw75] S. W. Hawking. "Particle Creation by Black Holes." In: *Communications in Mathematical Physics* 43.3 (Aug. 1, 1975), pp. 199–220. ISSN: 1432-0916. https://doi.org/10.1007/BF02345020.

[HHA21] Miroslav Hopjan, Fabian Heidrich-Meisner, and Vincenzo Alba. "Scaling Properties of a Spatial One-Particle Density-Matrix Entropy in Many-Body Localized Systems." In: *Physical Review B* 104.3 (July 15, 2021), p. 035129. https://doi.org/10.1103/PhysRevB.104.035129.

[HK19] Ingo Homrighausen and Stefan Kehrein. “Out of Equilibrium Mean Field Dynamics in the Transverse Field Ising Model.” In: (Oct. 23, 2019). https://doi.org/10.48550/arXiv.1908.02596.

[Hos+16] Pavan Hosur et al. “Chaos in Quantum Channels.” In: *Journal of High Energy Physics* 2016.2 (Feb. 2016), p. 4. ISSN: 1029-8479. https://doi.org/10.1007/JHEP02(2016)004.

[HP07] Patrick Hayden and John Preskill. “Black Holes as Mirrors: Quantum Information in Random Subsystems.” In: *Journal of High Energy Physics* 2007.09 (Sept. 2007), pp. 120–120. ISSN: 1126-6708. https://doi.org/10.1088/1126-6708/2007/09/120.

[Hua21] Yichen Huang. *Extensive Entropy from Unitary Evolution*. Apr. 5, 2021. https://doi.org/10.48550/arXiv.2104.02053. preprint.

[Hus+13] David A. Huse et al. “Localization-Protected Quantum Order.” In: *Physical Review B* 88.1 (July 22, 2013), p. 014206. https://doi.org/10.1103/PhysRevB.88.014206.

[IEEE19] “IEEE Standard for Floating-Point Arithmetic.” In: *IEEE Std 754-2019 (Revision of IEEE 754-2008)* (July 2019), pp. 1–84. https://doi.org/10.1109/IEEESTD.2019.8766229.

[IS18] Eiki Iyoda and Takahiro Sagawa. “Scrambling of Quantum Information in Quantum Many-Body Systems.” In: *Physical Review A* 97.4 (Apr. 18, 2018). ISSN: 2469-9926, 2469-9934. https://doi.org/10.1103/PhysRevA.97.042330.

[Jur+17] P. Jurcevic et al. “Direct Observation of Dynamical Quantum Phase Transitions in an Interacting Many-Body System.” In: *Physical Review Letters* 119.8 (Aug. 21, 2017), p. 080501. https://doi.org/10.1103/PhysRevLett.119.080501.

[Kah96] D. Kahn. *The Codebreakers: The Comprehensive History of Secret Communication from Ancient Times to the Internet*. Scribner, 1996. ISBN: 978-1-4391-0355-5.

[KBP14] Jonas A. Kjäll, Jens H. Bardarson, and Frank Pollmann. “Many-Body Localization in a Disordered Quantum Ising Chain.” In: *Physical Review Letters* 113.10

(Sept. 4, 2014), p. 107204. https://doi.org/10.1103/PhysRevLett.113.107204.

[KDP80] K. v. Klitzing, G. Dorda, and M. Pepper. "New Method for High-Accuracy Determination of the Fine-Structure Constant Based on Quantized Hall Resistance." In: *Physical Review Letters* 45.6 (Aug. 11, 1980), pp. 494–497. ISSN: 0031-9007. https://doi.org/10.1103/PhysRevLett.45.494.

[Kel+15] J. Kelly et al. "State Preservation by Repetitive Error Detection in a Superconducting Quantum Circuit." In: *Nature* 519.7541 (7541 Mar. 2015), pp. 66–69. ISSN: 1476-4687. https://doi.org/10.1038/nature14270.

[Ker83] Auguste Kerckhoffs. *La Cryptographie Militaire, Ou, Des Chiffres Usités En Temps de Guerre: Avec Un Nouveau Procédé de Déchiffrement Applicable Aux Systèmes à Double Clef*. Librairie militaire de L. Baudoin, 1883.

[KHN18] Vedika Khemani, David A. Huse, and Adam Nahum. "Velocity-Dependent Lyapunov Exponents in Many-Body Quantum, Semiclassical, and Classical Chaos." In: *Physical Review B* 98.14 (Oct. 16, 2018), p. 144304. https://doi.org/10.1103/PhysRevB.98.144304.

[Kie+20] Maximilian Kiefer-Emmanouilidis et al. "Evidence for Unbounded Growth of the Number Entropy in Many-Body Localized Phases." In: *Physical Review Letters* 124.24 (June 16, 2020), p. 243601. https://doi.org/10.1103/PhysRevLett.124.243601.

[Kit03] A. Yu. Kitaev. "Fault-Tolerant Quantum Computation by Anyons." In: *Annals of Physics* 303.1 (Jan. 1, 2003), pp. 2–30. ISSN: 0003-4916. https://doi.org/10.1016/S0003-4916(02)00018-0.

[KLZ98] Emanuel Knill, Raymond Laflamme, and Wojciech H. Zurek. "Resilient Quantum Computation." In: *Science* 279.5349 (Jan. 16, 1998), pp. 342–345. https://doi.org/10.1126/science.279.5349.342.

[Kna18] Michael Knap. "Entanglement Production and Information Scrambling in a Noisy Spin System." In: *Physical Review B* 98.18 (Nov. 15, 2018), p. 184416. ISSN: 2469-9950, 2469-9969. https://doi.org/10.1103/PhysRevB.98.184416.

[KOI22] Yoshihito Kuno, Takahiro Orito, and Ikuo Ichinose. “Information Spreading and Scrambling in Disorder-Free Multiple-Spin-Interaction Models.” In: *Physical Review A* 106.1 (July 27, 2022), p. 012435. https://doi.org/10.1103/PhysRevA.106.012435.

[KP06] Alexei Kitaev and John Preskill. “Topological Entanglement Entropy.” In: *Physical Review Letters* 96.11 (Mar. 24, 2006). ISSN: 0031-9007, 1079-7114. https://doi.org/10.1103/PhysRevLett.96.110404.

[Lan91] Rolf Landauer. “Information Is Physical.” In: *Physics Today* 44.5 (May 1, 1991), pp. 23–29. ISSN: 0031-9228. https://doi.org/10.1063/1.881299.

[Lau83] R. B. Laughlin. “Anomalous Quantum Hall Effect: An Incompressible Quantum Fluid with Fractionally Charged Excitations.” In: *Physical Review Letters* 50.18 (May 2, 1983), pp. 1395–1398. ISSN: 0031-9007. https://doi.org/10.1103/PhysRevLett.50.1395.

[Lei+03] D. Leibfried et al. “Quantum Dynamics of Single Trapped Ions.” In: *Reviews of Modern Physics* 75.1 (Mar. 10, 2003), pp. 281–324. https://doi.org/10.1103/RevModPhys.75.281.

[LGS15] Tim Langen, Remi Geiger, and Jörg Schmiedmayer. “Ultracold Atoms Out of Equilibrium.” In: *Annual Review of Condensed Matter Physics* 6.1 (Mar. 1, 2015), pp. 201–217. ISSN: 1947-5454. https://doi.org/10.1146/annurev-conmatphys-031214-014548.

[Li+19] Keren Li et al. “Measuring Holographic Entanglement Entropy on a Quantum Simulator.” In: *npj Quantum Information* 5.1 (1 Apr. 23, 2019), pp. 1–6. ISSN: 2056-6387. https://doi.org/10.1038/s41534-019-0145-z.

[LLA15] David J. Luitz, Nicolas Laflorencie, and Fabien Alet. “Many-Body Localization Edge in the Random-Field Heisenberg Chain.” In: *Physical Review B* 91.8 (Feb. 9, 2015), p. 081103. https://doi.org/10.1103/PhysRevB.91.081103.

[Llo96] Seth Lloyd. “Universal Quantum Simulators.” In: *Science* 273.5278 (Aug. 23, 1996), p. 1073. https://doi.org/10.1126/science.273.5278.1073.

[LMG65] H. J. Lipkin, N. Meshkov, and A. J. Glick. “Validity of Many-Body Approximation Methods for a Solvable Model: (I). Exact Solutions and Perturbation The-

ory." In: *Nuclear Physics* 62.2 (Feb. 1, 1965), pp. 188–198. ISSN: 0029-5582. https://doi.org/10.1016/0029-5582(65)90862-X.

[Luk+19] Alexander Lukin et al. "Probing Entanglement in a Many-Body–Localized System." In: *Science* 364.6437 (Apr. 19, 2019), pp. 256–260. https://doi.org/10.1126/science.aau0818.

[Make] *Make - GNU Project - Free Software Foundation*. URL: https://www.gnu.org/software/make/.

[Man80] Yuri Manin. "Computable and Uncomputable." In: *Sovetskoye Radio, Moscow* 128 (1980).

[MC17] Rubem Mondaini and Zi Cai. "Many-Body Self-Localization in a Translation-Invariant Hamiltonian." In: *Physical Review B* 96.3 (July 31, 2017), p. 035153. https://doi.org/10.1103/PhysRevB.96.035153.

[Mez07] Francesco Mezzadri. "How to Generate Random Matrices from the Classical Compact Groups." In: *Notices of the American Mathematical Society* 54.5 (2007), pp. 592–604. https://doi.org/10.48550/arXiv.math-ph/0609050.

[MKP03] D.J.C. MacKay, D.J.C.M. Kay, and Cambridge University Press. *Information Theory, Inference, and Learning Algorithms*. Cambridge University Press, 2003. ISBN: 978-0-521-64298-9. URL: https://www.inference.org.uk/mackay/itila/.

[MSS16] Juan Maldacena, Stephen H. Shenker, and Douglas Stanford. "A Bound on Chaos." In: *Journal of High Energy Physics* 2016.8 (Aug. 1, 2016), p. 106. ISSN: 1029-8479. https://doi.org/10.1007/JHEP08(2016)106.

[MT61] N.F. Mott and W.D. Twose. "The Theory of Impurity Conduction." In: *Advances in Physics* 10.38 (Apr. 1961), pp. 107–163. ISSN: 0001-8732, 1460-6976. https://doi.org/10.1080/00018736100101271.

[N22] "40 Years of Quantum Computing." In: *Nature Reviews Physics* 4.1 (1 Jan. 2022), pp. 1–1. ISSN: 2522-5820. https://doi.org/10.1038/s42254-021-00410-6.

[NC00] M.A. Nielsen and I.L. Chuang. *Quantum Computation and Quantum Information*. Cambridge Series on Information and the Natural Sciences. Cambridge University Press, 2000. ISBN: 978-0-521-63503-5. https://doi.org/doi:10.1017/CBO9780511976667.

[NH15] Rahul Nandkishore and David A. Huse. “Many Body Localization and Thermalization in Quantum Statistical Mechanics.” In: *Annual Review of Condensed Matter Physics* 6.1 (Mar. 2015), pp. 15–38. ISSN: 1947-5454, 1947-5462. https://doi.org/10.1146/annurev-conmatphys-031214-014726.

[OH07] Vadim Oganesyan and David A. Huse. “Localization of Interacting Fermions at High Temperature.” In: *Physical Review B* 75.15 (Apr. 23, 2007), p. 155111. https://doi.org/10.1103/PhysRevB.75.155111.

[OKI22] Takahiro Orito, Yoshihito Kuno, and Ikuo Ichinose. “Quantum Information Spreading in Random Spin Chains with Topological Order.” In: *Physical Review B* 106.10 (Sept. 21, 2022), p. 104204. https://doi.org/10.1103/PhysRevB.106.104204.

[OV06] Tobias J. Osborne and Frank Verstraete. “General Monogamy Inequality for Bipartite Qubit Entanglement.” In: *Physical Review Letters* 96.22 (June 7, 2006), p. 220503. https://doi.org/10.1103/PhysRevLett.96.220503.

[Pae+19] Sebastian Paeckel et al. “Time-Evolution Methods for Matrix-Product States.” In: *Annals of Physics* 411 (Dec. 1, 2019), p. 167998. ISSN: 0003-4916. https://doi.org/10.1016/j.aop.2019.167998.

[Pag93] Don N. Page. “Average Entropy of a Subsystem.” In: *Physical Review Letters* 71.9 (Aug. 30, 1993), pp. 1291–1294. ISSN: 0031-9007. https://doi.org/10.1103/PhysRevLett.71.1291.

[Pag95] Don N. Page. *Black Hole Information.* Feb. 25, 1995. https://doi.org/10.48550/arXiv.hep-th/9305040. preprint.

[Pre+07] William H. Press et al. *Numerical Recipes 3rd Edition: The Art of Scientific Computing*. 3rd ed. USA: Cambridge University Press, 2007. ISBN: 0-521-88068-8. URL: http://numerical.recipes/.

[PSA15] Z. Papić, E. Miles Stoudenmire, and Dmitry A. Abanin. “Many-Body Localization in Disorder-Free Systems: The Importance of Finite-Size Constraints.” In: *Annals of Physics* 362 (Nov. 1, 2015), pp. 714–725. ISSN: 0003-4916. https://doi.org/10.1016/j.aop.2015.08.024.

[Rén61] Alfréd Rényi. “On Measures of Entropy and Information.” In: *Proceedings of the Fourth Berkeley Symposium on Mathematical Statistics and Probability, Vol-*

ume 1: Contributions to the Theory of Statistics. Vol. 4. University of California Press. 1961, pp. 547–562.

[RPvK18] Tibor Rakovszky, Frank Pollmann, and C. W. von Keyserlingk. "Diffusive Hydrodynamics of Out-of-Time-Ordered Correlators with Charge Conservation." In: *Physical Review X* 8.3 (Sept. 7, 2018), p. 031058. https://doi.org/10.1103/PhysRevX.8.031058.

[RS15] Daniel A. Roberts and Douglas Stanford. "Diagnosing Chaos Using Four-Point Functions in Two-Dimensional Conformal Field Theory." In: *Physical Review Letters* 115.13 (Sept. 22, 2015), p. 131603. https://doi.org/10.1103/PhysRevLett.115.131603.

[RSA78] R L Rivest, A Shamir, and L Adleman. "A Method for Obtaining Digital Signatures and Public-Key Cryptosystems." In: 21.2 (1978). https://doi.org/10.1145/359340.359342.

[RSS15] Daniel A. Roberts, Douglas Stanford, and Leonard Susskind. "Localized Shocks." In: *Journal of High Energy Physics* 2015.3 (Mar. 10, 2015), p. 51. ISSN: 1029-8479. https://doi.org/10.1007/JHEP03(2015)051.

[San10] Anders W. Sandvik. "Computational Studies of Quantum Spin Systems." In: *AIP Conference Proceedings* 1297.1 (Nov. 3, 2010), pp. 135–338. ISSN: 0094-243X. https://doi.org/10.1063/1.3518900.

[SB11] Bruno Sciolla and Giulio Biroli. "Dynamical Transitions and Quantum Quenches in Mean-Field Models." In: *Journal of Statistical Mechanics: Theory and Experiment* 2011.11 (Nov. 2, 2011), P11003. ISSN: 1742-5468. https://doi.org/10.1088/1742-5468/2011/11/P11003.

[SC16] Conrad Sanderson and Ryan Curtin. "Armadillo: A Template-Based C++ Library for Linear Algebra." In: *The Journal of Open Source Software* 1.2 (June 10, 2016), p. 26. ISSN: 2475-9066. https://doi.org/10.21105/joss.00026.

[SC18] Conrad Sanderson and Ryan Curtin. "A User-Friendly Hybrid Sparse Matrix Class in C++." In: *Mathematical Software – ICMS 2018*. Ed. by James H. Davenport et al. Vol. 10931. Lecture Notes in Computer Science. Cham: Springer International Publishing, 2018, pp. 422–430. ISBN: 978-3-319-96417-1. https://doi.org/10.1007/978-3-319-96418-8_50. (Visited on 01/13/2023).

[SCF21] Zheng-Hang Sun, Jian Cui, and Heng Fan. “Quantum Information Scrambling in the Presence of Weak and Strong Thermalization.” In: *Physical Review A* 104.2 (Aug. 5, 2021), p. 022405. https://doi.org/10.1103/PhysRevA.104.022405.

[Sch+14] Romana Schirhagl et al. “Nitrogen-Vacancy Centers in Diamond: Nanoscale Sensors for Physics and Biology.” In: *Annual Review of Physical Chemistry* 65.1 (Apr. 1, 2014), pp. 83–105. ISSN: 0066-426X. https://doi.org/10.1146/annurev-physchem-040513-103659.

[Sch+15] Michael Schreiber et al. “Observation of Many-Body Localization of Interacting Fermions in a Quasirandom Optical Lattice.” In: *Science* 349.6250 (Aug. 21, 2015), pp. 842–845. ISSN: 0036-8075, 1095-9203. https://doi.org/10.1126/science.aaa7432.

[Sch+19] Oskar Schnaack et al. “Tripartite Information, Scrambling, and the Role of Hilbert Space Partitioning in Quantum Lattice Models.” In: *Physical Review B* 100.22 (Dec. 11, 2019), p. 224302. https://doi.org/10.1103/PhysRevB.100.224302.

[Sch+21] Oskar Schnaack et al. *Replication Data for: Phys. Rev. B 100, 224302*. Version V1. GRO.data, 2021. https://doi.org/10.25625/E3UZ7I.

[Sch17] Oskar H Schnaack. “Dynamics of the Tripartite Information in Quantum Many Body Systems.” MA thesis. Göttingen: Georg-August-Universität Göttingen, Dec. 22, 2017.

[Sha48] C. E. Shannon. “A Mathematical Theory of Communication.” In: *The Bell System Technical Journal* 27.3 (July 1948), pp. 379–423. ISSN: 0005-8580. https://doi.org/10.1002/j.1538-7305.1948.tb01338.x.

[Sha49a] C. E. Shannon. “Communication Theory of Secrecy Systems.” In: *The Bell System Technical Journal* 28.4 (Oct. 1949), pp. 656–715. ISSN: 0005-8580. https://doi.org/10.1002/j.1538-7305.1949.tb00928.x.

[Sha49b] C.E. Shannon. “Communication in the Presence of Noise.” In: *Proceedings of the IRE* 37.1 (Jan. 1949), pp. 10–21. ISSN: 2162-6634. https://doi.org/10.1109/JRPROC.1949.232969.

[Sho94] P.W. Shor. “Algorithms for Quantum Computation: Discrete Logarithms and Factoring.” In: *Proceedings 35th Annual Symposium on Foundations of Computer Science*. 35th Annual Symposium on Foundations of Computer Science. Santa Fe, NM, USA: IEEE Comput. Soc. Press, 1994, pp. 124–134. ISBN: 978-0-8186-6580-6. https://doi.org/10.1109/SFCS.1994.365700.

[Sho96] P.W. Shor. “Fault-Tolerant Quantum Computation.” In: *Proceedings of 37th Conference on Foundations of Computer Science*. Proceedings of 37th Conference on Foundations of Computer Science. Oct. 1996, pp. 56–65. https://doi.org/10.1109/SFCS.1996.548464.

[SJ05] Heinz Georg Schuster and Wolfram Just. *Deterministic Chaos: An Introduction*. 4., rev. and enl. ed. Weinheim: Wiley-VCH, 2005. 287 pp. ISBN: 978-3-527-40415-5. https://doi.org/10.1002/3527604804.

[Smi+16] J. Smith et al. “Many-Body Localization in a Quantum Simulator with Programmable Random Disorder.” In: *Nature Physics* 12.10 (10 Oct. 2016), pp. 907–911. ISSN: 1745-2481. https://doi.org/10.1038/nphys3783.

[Smi+17] A. Smith et al. “Disorder-Free Localization.” In: *Physical Review Letters* 118.26 (June 27, 2017), p. 266601. https://doi.org/10.1103/PhysRevLett.118.266601.

[SN21] J. J Sakurai and Jim Napolitano. *Modern Quantum Mechanics*. Cambridge: Cambridge University Press, 2021. ISBN: 978-1-108-47322-4. https://doi.org/10.1017/9781108499996.

[SP21] Dries Sels and Anatoli Polkovnikov. “Dynamical Obstruction to Localization in a Disordered Spin Chain.” In: *Physical Review E* 104.5 (Nov. 8, 2021), p. 054105. https://doi.org/10.1103/PhysRevE.104.054105.

[SPA13] Maksym Serbyn, Z. Papić, and Dmitry A. Abanin. “Universal Slow Growth of Entanglement in Interacting Strongly Disordered Systems.” In: *Physical Review Letters* 110.26 (June 28, 2013), p. 260601. https://doi.org/10.1103/PhysRevLett.110.260601.

[SR10] Lea F. Santos and Marcos Rigol. “Onset of Quantum Chaos in One-Dimensional Bosonic and Fermionic Systems and Its Relation to Thermalization.” In: *Physical Review E* 81.3 (Mar. 5, 2010), p. 036206. https://doi.org/10.1103/PhysRevE.81.036206.

[Sre94] Mark Srednicki. “Chaos and Quantum Thermalization.” In: *Physical Review E* 50.2 (Aug. 1, 1994), pp. 888–901. https://doi.org/10.1103/PhysRevE.50.888.

[SS14a] Stephen H. Shenker and Douglas Stanford. “Black Holes and the Butterfly Effect.” In: *Journal of High Energy Physics* 2014.3 (Mar. 13, 2014), p. 67. ISSN: 1029-8479. https://doi.org/10.1007/JHEP03(2014)067.

[SS14b] Stephen H. Shenker and Douglas Stanford. “Multiple Shocks.” In: *Journal of High Energy Physics* 2014.12 (Dec. 4, 2014), p. 46. ISSN: 1029-8479. https://doi.org/10.1007/JHEP12(2014)046.

[SS15] Stephen H. Shenker and Douglas Stanford. “Stringy Effects in Scrambling.” In: *Journal of High Energy Physics* 2015.5 (May 26, 2015), p. 132. ISSN: 1029-8479. https://doi.org/10.1007/JHEP05(2015)132.

[SSS19] Phil Saad, Stephen H. Shenker, and Douglas Stanford. *A Semiclassical Ramp in SYK and in Gravity*. July 23, 2019. https://doi.org/10.48550/arXiv.1806.06840. preprint.

[Sün+19] Christoph Sünderhauf et al. “Quantum Chaos in the Brownian SYK Model with Large Finite N : OTOCs and Tripartite Information.” In: *Journal of High Energy Physics* 2019.11 (Nov. 2019), p. 38. ISSN: 1029-8479. https://doi.org/10.1007/JHEP11(2019)038.

[Šun+20] Jan Šuntajs et al. “Quantum Chaos Challenges Many-Body Localization.” In: *Physical Review E* 102.6 (Dec. 24, 2020), p. 062144. https://doi.org/10.1103/PhysRevE.102.062144.

[SXS19] Subhayan Sahu, Shenglong Xu, and Brian Swingle. “Scrambling Dynamics across a Thermalization-Localization Quantum Phase Transition.” In: *Physical Review Letters* 123.16 (Oct. 18, 2019), p. 165902. https://doi.org/10.1103/PhysRevLett.123.165902.

[SY93] Subir Sachdev and Jinwu Ye. “Gapless Spin-Fluid Ground State in a Random Quantum Heisenberg Magnet.” In: *Physical Review Letters* 70.21 (May 24, 1993), pp. 3339–3342. https://doi.org/10.1103/PhysRevLett.70.3339.

[SymMPS] *The SciPAL SymMPS Toolkit*. URL: https://www.symmps.eu/.

[TM71] Myron Tribus and Edward C. McIrvine. “ENERGY AND INFORMATION.” In: *Scientific American* 225.3 (1971), pp. 179–190. ISSN: 00368733, 19467087. JSTOR: 24923125.

[Tri59] M. Tribus. *Thermostatics and Thermodynamics: An Introduction to Energy, Information and States of Matter, with Engineering Applications*. Thermostatics and Thermodynamics: An Introduction to Energy, Information and States of Matter, with Engineering Applications Bd. 1. Van Nostrand, 1959.

[TSG82] D. C. Tsui, H. L. Stormer, and A. C. Gossard. “Two-Dimensional Magnetotransport in the Extreme Quantum Limit.” In: *Physical Review Letters* 48.22 (May 31, 1982), pp. 1559–1562. ISSN: 0031-9007. https://doi.org/10.1103/PhysRevLett.48.1559.

[Ver26] G. S. Vernam. “Cipher Printing Telegraph Systems: For Secret Wire and Radio Telegraphic Communications.” In: *Journal of the A.I.E.E.* 45.2 (Feb. 1926), pp. 109–115. ISSN: 2376-5976. https://doi.org/10.1109/JAIEE.1926.6534724.

[vKey+18] C. W. von Keyserlingk et al. “Operator Hydrodynamics, OTOCs, and Entanglement Growth in Systems without Conservation Laws.” In: *Physical Review X* 8.2 (Apr. 11, 2018). ISSN: 2160-3308. https://doi.org/10.1103/PhysRevX.8.021013.

[vNeu32] John von Neumann. *Mathematische Grundlagen Der Quantenmechanik*. Berlin [u.a.]: Springer, 1932. https://doi.org/10.1007/978-3-642-61409-5.

[WB17] Phillip Weinberg and Marin Bukov. “QuSpin: A Python Package for Dynamics and Exact Diagonalisation of Quantum Many Body Systems Part I: Spin Chains.” In: *SciPost Physics* 2.1 (Feb. 13, 2017), p. 003. ISSN: 2542-4653. https://doi.org/10.21468/SciPostPhys.2.1.003.

[WB19] Phillip Weinberg and Marin Bukov. “QuSpin: A Python Package for Dynamics and Exact Diagonalisation of Quantum Many Body Systems. Part II: Bosons, Fermions and Higher Spins.” In: *SciPost Physics* 7.2 (Aug. 9, 2019), p. 020. ISSN: 2542-4653. https://doi.org/10.21468/SciPostPhys.7.2.020.

[Wil17] Mark Wilde. *Quantum Information Theory*. Second edition. Cambridge, UK ; New York: Cambridge University Press, 2017. 757 pp. ISBN: 978-1-107-17616-4. https://doi.org/10.1017/CBO9781139525343.

[Xu+18] Kai Xu et al. “Emulating Many-Body Localization with a Superconducting Quantum Processor.” In: *Physical Review Letters* 120.5 (Feb. 2, 2018), p. 050507. https://doi.org/10.1103/PhysRevLett.120.050507.

[Yan+19] Zhiguang Yan et al. “Strongly Correlated Quantum Walks with a 12-Qubit Superconducting Processor.” In: *Science* 364.6442 (May 24, 2019), pp. 753–756. https://doi.org/10.1126/science.aaw1611.

[Yao+16] N. Y. Yao et al. “Quasi-Many-Body Localization in Translation-Invariant Systems.” In: *Physical Review Letters* 117.24 (Dec. 7, 2016), p. 240601. ISSN: 0031-9007, 1079-7114. https://doi.org/10.1103/PhysRevLett.117.240601.

[YY66a] C. N. Yang and C. P. Yang. “One-Dimensional Chain of Anisotropic Spin-Spin Interactions. I. Proof of Bethe’s Hypothesis for Ground State in a Finite System.” In: *Physical Review* 150.1 (Oct. 7, 1966), pp. 321–327. https://doi.org/10.1103/PhysRev.150.321.

[YY66b] C. N. Yang and C. P. Yang. “One-Dimensional Chain of Anisotropic Spin-Spin Interactions. II. Properties of the Ground-State Energy Per Lattice Site for an Infinite System.” In: *Physical Review* 150.1 (Oct. 7, 1966), pp. 327–339. ISSN: 0031-899X. https://doi.org/10.1103/PhysRev.150.327.

[Žni20] Marko Žnidarič. “Weak Integrability Breaking: Chaos with Integrability Signature in Coherent Diffusion.” In: *Physical Review Letters* 125.18 (Oct. 28, 2020), p. 180605. https://doi.org/10.1103/PhysRevLett.125.180605.

[ŽPP08] Marko Žnidarič, Tomaž Prosen, and Peter Prelovšek. “Many-Body Localization in the Heisenberg XXZ Magnet in a Random Field.” In: *Physical Review B* 77.6 (Feb. 25, 2008), p. 064426. https://doi.org/10.1103/PhysRevB.77.064426.

Appendix A

Acknowledgements

First and foremost I would like to thank my advisor, Stefan Kehrein, who was always a deep fountain of physical knowledge and intuition and provided immensely valuable feedback during the entire project. The research group was always a comfortable place conducive to creative thinking and study. I'd also like to thank my colleagues in the group for the great atmosphere, especially my officemate Alexander Osterkorn, who also provided invaluable feedback both during the project and the writing of the thesis.

The numerical code by Oskar Schnaack and the SymMPS toolkit by Thomas Köhler and Sebastian Paeckel proved to be indispensable for verifying our numerical results. I thank Sebastian Paeckel in particular for his help with setting up a tripartite information calculation with SymMPS. I also thank Nils Abeling who provided the code for the unfolding of the level statistics.

I also want to thank the other members of my thesis advisory committee (and examination board), Fabian Heidrich-Meisner and Salvatore R. Manmana for guiding me through the PhD project successfully up to this point, and the other members of the examination board, Laura Covi, Matthias Krüger, Michael Seibt, and Steffen Schumann for their work.

I'd like to thank the entire institute of theoretical physics for providing my home away from home, in particular the capable secretaries Gabriele Schubert, Katrin Glormann and Kati Oldenburg. And finally my entire family, especially Eklekta, for always supporting me.

Appendix B

Source Code of the Partial Trace Implementation

```
#ifndef HARDCORE_BOSONS
int i, j, k, l;
#endif

const double sign[2] = {1.0, -1.0};

// We need indices for rho_TFD = rho_ABCD and rho_AC
// We calculate the matrix elements of rho_TFD on
// the fly from the TFD vector
int row_AB, col_AB, row_CD, col_CD;
int row_A,  col_A,  row_C,  col_C;

// We only need the diagonal masks for B and D!
// The actual index would be pext(*_diag, mask_*)
int B_diag, D_diag;

int AC, row_ABCD, col_ABCD;

int length_A = __builtin_popcount(mask_A);
int length_C = __builtin_popcount(mask_C);
int mask_B = ((1<<L) - 1) - mask_A;
```

```
int mask_D = ((1<<L) - 1) - mask_C;

char buf[1024];

start = clock();

memset(rho_red, '\0', (1<<length_A) *  (1<<length_A)
  * (1<<length_C) *  (1<<length_C) * sizeof(double _Complex));

for(row_AB = 0; row_AB < (1 << L); row_AB++)
{
  row_A = _pext_u32(row_AB, mask_A);
  B_diag = row_AB & mask_B;

  for(row_CD = 0; row_CD < (1 << L); row_CD++)
  {
    row_C = _pext_u32(row_CD, mask_C);
    D_diag = row_CD & mask_D;

    row_ABCD = row_CD + (row_AB << L);

    if(TFD[row_ABCD] == 0.0)
    {
      continue;
    }

    #ifndef HARDCORE_BOSONS
    k = 0;
    for(i = 1; i < L; i++)
    {
      k += __builtin_popcount(_pdep_u32(row_C, mask_C) & (D_diag << i));
      k += __builtin_popcount(_pdep_u32(row_A, mask_A) & (B_diag << i));
    }
    #endif

    for(col_A = 0; col_A < (1 << length_A); col_A++)
```

```
58      {
59        col_AB = _pdep_u32(col_A, mask_A) + B_diag;
60
61        #ifndef HARDCORE_BOSONS
62        j = 0;
63        for(i = 1; i < L; i++)
64        {
65          j += __builtin_popcount(_pdep_u32(col_A, mask_A) & (B_diag << i));
66        }
67        #endif
68
69        for(col_C = 0; col_C < (1 << length_C); col_C++)
70        {
71          col_CD = _pdep_u32(col_C, mask_C) + D_diag;
72
73          // Should be inverse order of for loops to help the compiler!
74          AC = col_C + ((col_A +
75            ((row_C + (row_A << length_C)) << length_A)) << length_C);
76          col_ABCD = col_CD + (col_AB << L);
77          // We need take into account the commutation relations of the
78          // fermionic operators!
79
80          #ifndef HARDCORE_BOSONS
81          l = 0;
82          for(i = 1; i < L; i++)
83          {
84            l += __builtin_popcount(_pdep_u32(col_C, mask_C) & (D_diag << i));
85          }
86          #endif
87
88          // Same here: make sure the conj() does not depend on the inner loops!
89
90          #ifdef HARDCORE_BOSONS
91          rho_red[AC] += conj(TFD[row_ABCD]) * TFD[col_ABCD];
92          #else
93          rho_red[AC] += sign[(j+k+l)&1] * conj(TFD[row_ABCD]) * TFD[col_ABCD];
```

```
94            #endif
95          }
96        }
97      }
98    #ifndef QUIET
99      snprintf(buf, sizeof(buf), "Partial Trace %i/%i", row_AB+1, 1 << L);
100     report_status(buf);
101   #endif
102   }
103   #ifdef QUIET
104   snprintf(buf, sizeof(buf), "Partial Trace %i/%i", 1 << L, 1 << L);
105   report_status(buf);
106   #endif
107
108   report_elapsed_time();
109
110   show_checksum(rho_red, (1<<length_A) * (1<<length_C) * sizeof (double _Complex));
111
112   #ifdef DEBUG
113   check_hermitian(rho_red, (1<<length_A) * (1<<length_C));
114   #endif
```

Appendix C

SymMPS Setup Files

The following finite state machine representation of the spinless fermion system was used in conjunction with SymMPS[SymMPS].

```
# local operators supported by this basis: Id; f; f_dagger; n_f; n_h
# in curly brackets exprtk is used to parse expressions,
# known variables are position, L, time, beta

subsection transposition
  set parameters              = i1; i2
  set description             = n_swaps=1
  set transitions             = I:Id:I; F:Id:F; \
        I:at_i1*f_dagger:A; A:Id:A; A:at_i2*f:F; \
        I:at_i1*f:B; B:Id:B; B:at_i2*f_dagger:F; \
        I:at_i1*n_f:C; C:Id:C; C:at_i2*n_f:F; \
        I:at_i1*n_h:D; D:Id:D; D:at_i2*n_h:F
  set print_ignore            = Id
  set weight_functions        = \
    at_i1: { if((position == i1), 1.0, 0.0) }; \
    at_i2: { if((position == i2), 1.0, 0.0) };
end

subsection spinless_fermions_tfd
  set parameters              = \
```

```
    t_aux; t_phys; lambda_aux; lambda_phys; V_aux; V_phys
  set description             =
  set transitions             = \
  I:Id:I; F:Id:F; \
    I:t1*f_dagger:T1; T1:Id:T2; T2:f:F; \
    I:t2*f:T3; T3:Id:T4; T4:f_dagger:F; \
    I:l1*f_dagger:TT1; TT1:Id:TT2; TT2:Id:T1; \
    I:l2*f:TT3; TT3:Id:TT4; TT4:Id:T3; \
    I:V*n_f:V1; V1:Id:V2; V2:n_f:F;
  set print_ignore            = Id
  set weight_functions        = \
    t1: {t_phys*even(position)+t_aux*odd(position)}; \
    t2: {-t_phys*even(position)-t_aux*odd(position)}; \
    l1: {lambda_phys*even(position)+lambda_aux*odd(position)}; \
    l2: {-lambda_phys*even(position)-lambda_aux*odd(position)}; \
    V: {V_phys*even(position)+V_aux*odd(position)};
end
```

The following model parameter file was also used.

```
subsection spinless_fermions_tfd
  subsection ground_state
    set t_phys    = -1.0
    set lambda_phys  = -0.5
    set V_phys    = 0.25
    set t_aux    = 0.0
    set lambda_aux  = 0.0
    set V_aux    = 0.0
  end
end
```

While the following commands were used to create the initial state of the system in the SymMPS framework:

```
L=8
DISC_WT="1e-12"
CHI_MAX=1000
```

```
#create real and complex lattice
sym-create-lattice -F d -L $(( 2*L )) -b custom -g 'n_f' -t $L -o lattice.real
sym-create-lattice -F c -L $(( 2*L )) -b custom -g 'n_f' -t $L -o lattice.complex

#create mpo for time-evolution
create_symmpo -i lattice.complex -r '' -P model_parameters.prm \
  -M spinless_fermions_tfd -n H -o mpo.complex

#create infinite temperature state in grand-canonical ensemble
sym-create-mps -i lattice.real -t max-entangled -w ${CHI_MAX} \
  -d ${DISC_WT} -o t_inf.symmps
```

The parameters for the DMRG simulation were: discarded weight 10^{-12}, $\chi_{\max} = 1000$ and the executable sym-calc-i3 was called with the parameters `-g 4 -n 10 -e 1e-12`.

The used version of SymMPS was b7a9541132bf7512b9d6c5490d72af445be29a64.

Appendix D

Short-time Behaviour of I_3

We can split up the Hamiltonian H into a part H_0 that only acts inside the respective partition and a part $H_{\bowtie}$ that connects the two partitions:

$$H = H_0 + H_{\bowtie}. \tag{D.1}$$

If we act unitarily on only one of the subsystems, say with $U_A : H_A \to H_A$, we cannot change the correlations between the subsystems, and the tripartite information will stay invariant. This also follows from the symmetry of the tripartite information, e.g. $I_3(A:B:C) \equiv I_3(B:C:D)$, which itself follows from the purity of the state of $ABCD$.

This in turn motivates us to write down the thermo-field double state $|\text{TFD}\rangle$ in such a way that the dependence of the short-time behaviour on $H_{\bowtie}$ becomes manifest.

$$|\text{TFD}\rangle = \frac{1}{\sqrt{Z}} \sum_n e^{-\beta H/2} \left|n\right\rangle_{AB} \otimes e^{iH_0 t} e^{-i(H_0+H_{\bowtie})t} \left|\left|n\right\rangle\right\rangle_{CD} \tag{D.2}$$

We now expand around $t = 0$ while applying the Baker–Campbell–Hausdorff formula:

$$e^{iH_0 t} e^{-i(H_0+H_{\bowtie})t} = e^{-iH_{\bowtie}t + \frac{1}{2}[H_0, H_{\bowtie}]t^2} + O(t^3) \tag{D.3}$$

$$= 1 - itH_{\bowtie} - \frac{t^2}{2} H_{\bowtie}^2 + \frac{t^2}{2}[H_0, H_{\bowtie}] + O(t^3) \tag{D.4}$$

For the free fermion system with open boundary conditions and partition boundary in the

centre of the chain, we have explicitly:

$$H_0 = -\sum_{j=1}^{L/2-1}\left(\hat{c}_j^\dagger \hat{c}_{j+1} + \text{h.c.}\right) - \sum_{j=L/2+1}^{L-1}\left(\hat{c}_j^\dagger \hat{c}_{j+1} + \text{h.c.}\right) \tag{D.5}$$

$$H_\bowtie = -\left(\hat{c}_j^\dagger \hat{c}_{j+1} + \text{h.c.}\right)\Big|_{j=L/2} \tag{D.6}$$

$$\begin{aligned}
H_\bowtie^2 &= \left(\hat{c}_j^\dagger \hat{c}_{j+1}\hat{c}_{j+1}^\dagger \hat{c}_j + \hat{c}_{j+1}^\dagger \hat{c}_j \hat{c}_j^\dagger \hat{c}_{j+1}\right)\Big|_{j=L/2} \\
&= \hat{n}_{L/2}(\hat{1} - \hat{n}_{L/2+1}) + \hat{n}_{L/2+1}(\hat{1} - \hat{n}_{L/2}) \\
[H_0, H_\bowtie] &= \left[\hat{c}_{L/2-1}^\dagger \hat{c}_{L/2} + \hat{c}_{L/2+1}^\dagger \hat{c}_{L/2+2}, \hat{c}_{L/2}^\dagger \hat{c}_{L/2+1}\right] - \text{h.c.} \\
&= \left[\hat{c}_{L/2-1}^\dagger \hat{c}_{L/2}, \hat{c}_{L/2}^\dagger \hat{c}_{L/2+1}\right] + \left[\hat{c}_{L/2+1}^\dagger \hat{c}_{L/2+2}, \hat{c}_{L/2}^\dagger \hat{c}_{L/2+1}\right] - \text{h.c.} \\
&= \left[\hat{c}_{L/2-1}^\dagger \hat{c}_{L/2}, \hat{c}_{L/2}^\dagger \hat{c}_{L/2+1}\right] - \left[\hat{c}_{L/2}^\dagger \hat{c}_{L/2+1}, \hat{c}_{L/2+1}^\dagger \hat{c}_{L/2+2}\right] - \text{h.c.} \\
&= \hat{c}_{L/2-1}^\dagger \left\{\hat{c}_{L/2}, \hat{c}_{L/2}^\dagger\right\} \hat{c}_{L/2+1} - \hat{c}_{L/2}^\dagger \left\{\hat{c}_{L/2+1}, \hat{c}_{L/2+1}^\dagger\right\} \hat{c}_{L/2+2} - \text{h.c.} \\
&= \hat{c}_{L/2-1}^\dagger \hat{c}_{L/2+1} - \hat{c}_{L/2}^\dagger \hat{c}_{L/2+2} - \text{h.c.}
\end{aligned}$$

We will now expand the thermo-field double state for $\beta = 0$.

$$
\begin{aligned}
\rho_0 &\overset{\text{def}}{=} \rho_{\text{TFD}}(t=0) = \frac{1}{Z}\sum_{n,m} |n\rangle\langle m| \otimes ||n\rangle\rangle\langle\langle m|| \\
\rho_{\text{TFD}} &= \frac{1}{Z}\sum_{n,m} |n\rangle\langle m| \otimes e^{iH_0 t} e^{-i(H_0+H_\bowtie)t} ||n\rangle\rangle\langle\langle m|| \, e^{i(H_0+H_\bowtie)t} e^{-iH_0 t} \\
&= \frac{1}{Z}\sum_{n,m} |n\rangle\langle m| \otimes \left(1 - itH_\bowtie - \frac{t^2}{2}H_\bowtie^2 + \frac{t^2}{2}[H_0, H_\bowtie]\right) ||n\rangle\rangle \\
&\langle\langle m|| \left(1 + itH_\bowtie - \frac{t^2}{2}H_\bowtie^2 - \frac{t^2}{2}[H_0, H_\bowtie]\right) + O(t^3) \\
&= \frac{1}{Z}\sum_{n,m} |n\rangle\langle m| \otimes \Bigg(||n\rangle\rangle\langle\langle m|| - itH_\bowtie ||n\rangle\rangle\langle\langle m|| + ||n\rangle\rangle\langle\langle m|| \, itH_\bowtie \\
&+ t^2 H_\bowtie ||n\rangle\rangle\langle\langle m|| \, H_\bowtie - \frac{t^2}{2}H_\bowtie^2 ||n\rangle\rangle\langle\langle m|| + \frac{t^2}{2}[H_0, H_\bowtie] ||n\rangle\rangle\langle\langle m|| \\
&- ||n\rangle\rangle\langle\langle m|| \, \frac{t^2}{2}H_\bowtie^2 - ||n\rangle\rangle\langle\langle m|| \, \frac{t^2}{2}[H_0, H_\bowtie]\Bigg) + O(t^3) \\
&= \rho_0 - it\frac{1}{Z}\sum_{n,m} |n\rangle\langle m| \otimes \left(H_\bowtie ||n\rangle\rangle\langle\langle m|| - ||n\rangle\rangle\langle\langle m|| \, H_\bowtie\right) \\
&+ \frac{t^2}{2}\frac{1}{Z}\sum_{n,m} |n\rangle\langle m| \otimes \Big(2H_\bowtie ||n\rangle\rangle\langle\langle m|| \, H_\bowtie - H_\bowtie^2 ||n\rangle\rangle\langle\langle m|| + [H_0, H_\bowtie] ||n\rangle\rangle\langle\langle m|| \\
&- ||n\rangle\rangle\langle\langle m|| \, H_\bowtie^2 - ||n\rangle\rangle\langle\langle m|| \, [H_0, H_\bowtie]\Big) + O(t^3)
\end{aligned}
$$

$$
\begin{aligned}
\rho^2_{\text{TFD}} &= \rho_0^2 \\
&\quad - it\frac{1}{Z}\rho_0 \sum_{n,m} |n\rangle\langle m| \otimes \Big(H_\bowtie ||n\rangle\rangle \langle\langle m|| - ||n\rangle\rangle \langle\langle m|| H_\bowtie \Big) \\
&\quad - it\frac{1}{Z} \sum_{n,m} |n\rangle\langle m| \otimes \Big(H_\bowtie ||n\rangle\rangle \langle\langle m|| - ||n\rangle\rangle \langle\langle m|| H_\bowtie \Big)\rho_0 \\
&\quad - t^2\frac{1}{Z^2} \sum_{n,m,\nu} |n\rangle\langle m| \otimes \Big(H_\bowtie ||n\rangle\rangle \underbrace{\langle\langle \nu|| H_\bowtie ||\nu\rangle\rangle}_{0} \langle\langle m|| - H_\bowtie ||n\rangle\rangle \langle\langle \nu||\nu\rangle\rangle \langle\langle m|| H_\bowtie \Big) \\
&\quad + t^2\frac{1}{Z^2} \sum_{n,m,\nu} |n\rangle\langle m| \otimes \Big(||n\rangle\rangle \langle\langle \nu|| H_\bowtie H_\bowtie ||\nu\rangle\rangle \langle\langle m|| - ||n\rangle\rangle \underbrace{\langle\langle \nu|| H_\bowtie ||\nu\rangle\rangle}_{0} \langle\langle m|| H_\bowtie \Big) \\
&\quad + \frac{t^2}{2}\frac{1}{Z}\rho_0 \sum_{n,m} |n\rangle\langle m| \otimes \Big(2H_\bowtie ||n\rangle\rangle \langle\langle m|| H_\bowtie - H_\bowtie^2 ||n\rangle\rangle \langle\langle m|| + [H_0, H_\bowtie] ||n\rangle\rangle \langle\langle m|| \\
&\quad - ||n\rangle\rangle \langle\langle m|| H_\bowtie^2 - ||n\rangle\rangle \langle\langle m|| [H_0, H_\bowtie] \Big) \\
&\quad + \frac{t^2}{2}\frac{1}{Z} \sum_{n,m} |n\rangle\langle m| \otimes \Big(2H_\bowtie ||n\rangle\rangle \langle\langle m|| H_\bowtie - H_\bowtie^2 ||n\rangle\rangle \langle\langle m|| + [H_0, H_\bowtie] ||n\rangle\rangle \langle\langle m|| \\
&\quad - ||n\rangle\rangle \langle\langle m|| H_\bowtie^2 - ||n\rangle\rangle \langle\langle m|| [H_0, H_\bowtie] \Big)\rho_0 + O(t^3)
\end{aligned}
$$

$$
\begin{aligned}
&= \rho_0^2 \\
&- it\frac{1}{Z} \sum_{n,m} |n\rangle\langle m| \otimes \Big(||n\rangle\rangle \sum_\nu \underbrace{\langle\langle \nu|| H_\bowtie ||\nu\rangle\rangle}_{0} \langle\langle m|| - ||n\rangle\rangle \langle\langle m|| H_\bowtie \Big) \\
&- it\frac{1}{Z} \sum_{n,m} |n\rangle\langle m| \otimes \Big(H_\bowtie ||n\rangle\rangle \langle\langle m|| - ||n\rangle\rangle \sum_\nu \underbrace{\langle\langle nu|| H_\bowtie ||nu\rangle\rangle}_{0} \langle\langle m|| \Big) \\
&+ t^2\frac{1}{Z^2} \sum_{n,m,\nu} |n\rangle\langle m| \otimes \Big(H_\bowtie ||n\rangle\rangle \langle\langle \nu||\nu\rangle\rangle \langle\langle m|| H_\bowtie + ||n\rangle\rangle \langle\langle \nu|| H_\bowtie H_\bowtie ||\nu\rangle\rangle \langle\langle m|| \Big) \\
&+ \frac{t^2}{2}\frac{1}{Z^2} \sum_{n,m} |n\rangle\langle m| \otimes \Big(||n\rangle\rangle \sum_\nu \underbrace{\langle\langle \nu|| 2H_\bowtie ||\nu\rangle\rangle}_{0} \langle\langle m|| H_\bowtie - ||n\rangle\rangle \sum_\nu \langle\langle \nu|| H_\bowtie^2 ||\nu\rangle\rangle \langle\langle m|| \\
&+ ||n\rangle\rangle \sum_\nu \underbrace{\langle\langle \nu|| [H_0, H_\bowtie] ||\nu\rangle\rangle}_{0} \langle\langle m|| - ||n\rangle\rangle \langle\langle m|| H_\bowtie^2 - ||n\rangle\rangle \langle\langle m|| [H_0, H_\bowtie] \Big) \\
&+ \frac{t^2}{2}\frac{1}{Z^2} \sum_{n,m} |n\rangle\langle m| \otimes \Big(2H_\bowtie ||n\rangle\rangle \sum_\nu \underbrace{\langle\langle \nu|| H_\bowtie ||\nu\rangle\rangle}_{0} \langle\langle m|| - H_\bowtie^2 ||n\rangle\rangle \langle\langle m|| + [H_0, H_\bowtie] ||n\rangle\rangle \langle\langle m|| \\
&- ||n\rangle\rangle \sum_\nu \langle\langle \nu|| H_\bowtie^2 ||\nu\rangle\rangle \langle\langle m|| - ||n\rangle\rangle \sum_\nu \underbrace{\langle\langle \nu|| [H_0, H_\bowtie] ||\nu\rangle\rangle}_{0} \langle\langle m|| \Big) + O(t^3)
\end{aligned}
$$

$$
\begin{aligned}
\rho^2_{\text{TFD}} &= \rho_0^2 + it\frac{1}{Z}\sum_{n,m}|n\rangle\langle m|\otimes\Big(\,||n\rangle\rangle\langle\langle m||\,H_{\bowtie}-H_{\bowtie}\,||n\rangle\rangle\langle\langle m||\,\Big)\\
&\quad+t^2\frac{1}{Z^2}\sum_{n,m}|n\rangle\langle m|\otimes H_{\bowtie}\,||n\rangle\rangle\langle\langle m||\,H_{\bowtie}\\
&\quad-\frac{t^2}{2}\frac{1}{Z^2}\sum_{n,m}|n\rangle\langle m|\otimes\Big\{\,||n\rangle\rangle\langle\langle m||\,,H^2_{\bowtie}\Big\}\\
&\quad+\frac{t^2}{2}\frac{1}{Z^2}\sum_{n,m}|n\rangle\langle m|\otimes\Big[\,||n\rangle\rangle\langle\langle m||\,,[H_0,H_{\bowtie}]\Big]+O(t^3)\\
\mathtt{Tr}\rho^2_{\text{TFD}} &= \mathtt{Tr}\rho_0^2+\frac{t^2}{Z}\mathtt{Tr}\left(H_{\bowtie}\sum_{\nu}||\nu\rangle\rangle\langle\langle\nu||\,H_{\bowtie}-\frac{1}{2}(H^2_{\bowtie}+H^2_{\bowtie})\right)+O(t^3)=1+O(t^3)\\
\Rightarrow S^{(2)}_{ABCD}&=0
\end{aligned}
$$

$$
\begin{aligned}
\rho_{AC}(t=0)&=\frac{2^{L/2}}{2^L}(\,|0\rangle\,||0\rangle\rangle+|1\rangle\,||1\rangle\rangle\,)^{\otimes L/2}(\,\langle 0|\,\langle\langle 0||+\langle 1|\,\langle\langle 1||\,)^{\otimes L/2}\\
\Rightarrow S_{AC}(t=0)&=0\\
\rho_{AD}(t=0)&=\frac{1}{2^L}(\,|0\rangle\langle 0|+|1\rangle\langle 1|\,)^{\otimes L/2}(\,||0\rangle\rangle\langle\langle 0||+||1\rangle\rangle\langle\langle 1||\,)^{\otimes L/2}\\
\Rightarrow S_{AD}(t=0)&=L\cdot S\left(\frac{|0\rangle\langle 0|+|1\rangle\langle 1|}{2}\right)=L
\end{aligned}
$$

$$
\begin{aligned}
\rho_{AC}=&\frac{2^{L/2-2}}{2^L}\left(|0\rangle\,||0\rangle\rangle+|1\rangle\,||1\rangle\rangle\right)^{\otimes L/2-2}\left(\langle 0|\,\langle\langle 0||+\langle 1|\,\langle\langle 1||\right)^{\otimes L/2-2}\\
&\sum_{i,j,k,l=0}^{1}\Big[\mathbb{1}_{L/2-1}\otimes\mathbb{1}_{L/2}\otimes\langle i|\,\langle\langle j||_{L/2+1}\otimes\langle k|\,\langle\langle l||_{L/2+2}\,e^{iH_0t}e^{-i(H_0+H_{\bowtie})t}\\
&(|0\rangle\,||0\rangle\rangle+|1\rangle\,||1\rangle\rangle)\otimes(|0\rangle\,||0\rangle\rangle+|1\rangle\,||1\rangle\rangle)\otimes(|0\rangle\,||0\rangle\rangle+|1\rangle\,||1\rangle\rangle)\otimes(|0\rangle\,||0\rangle\rangle+|1\rangle\,||1\rangle\rangle)\\
&(\langle 0|\,\langle\langle 0||+\langle 1|\,\langle\langle 1||)\otimes(\langle 0|\,\langle\langle 0||+\langle 1|\,\langle\langle 1||)\otimes(\langle 0|\,\langle\langle 0||+\langle 1|\,\langle\langle 1||)\otimes(\langle 0|\,\langle\langle 0||+\langle 1|\,\langle\langle 1||)\\
&e^{i(H_0+H_{\bowtie})t}e^{-iH_0t}\mathbb{1}_{L/2-1}\otimes\mathbb{1}_{L/2}\otimes|i\rangle\,||j\rangle\rangle_{L/2+1}\otimes|k\rangle\,||l\rangle\rangle_{L/2+2}\Big]
\end{aligned}
$$

$$
\begin{aligned}
\rho_{AD} = & \frac{1}{2^L}\left(|0\rangle\langle 0| + |1\rangle\langle 1|\right)^{\otimes L/2-2} \\
& \sum_{i,j,k,l=0}^{1} \Big[\langle\langle i|\big|_{L/2-1} \otimes \langle\langle j|\big|_{L/2} \otimes \langle k|_{L/2+1} \otimes \langle l|_{L/2+2}\, e^{iH_0 t} e^{-i(H_0+H_{\bowtie})t} \\
& \left(|0\rangle\,||0\rangle\rangle + |1\rangle\,||1\rangle\rangle\right) \otimes \left(|0\rangle\,||0\rangle\rangle + |1\rangle\,||1\rangle\rangle\right) \otimes \left(|0\rangle\,||0\rangle\rangle + |1\rangle\,||1\rangle\rangle\right) \otimes \left(|0\rangle\,||0\rangle\rangle + |1\rangle\,||1\rangle\rangle\right) \\
& \left(\langle 0|\,\langle\langle 0|| + \langle 1|\,\langle\langle 1||\right) \otimes \left(\langle 0|\,\langle\langle 0|| + \langle 1|\,\langle\langle 1||\right) \otimes \left(\langle 0|\,\langle\langle 0|| + \langle 1|\,\langle\langle 1||\right) \otimes \left(\langle 0|\,\langle\langle 0|| + \langle 1|\,\langle\langle 1||\right) \\
& e^{i(H_0+H_{\bowtie})t} e^{-iH_0 t}\,||i\rangle\rangle_{L/2-1} \otimes ||j\rangle\rangle_{L/2} \otimes |k\rangle_{L/2+1} \otimes |k\rangle\,||l\rangle\rangle_{L/2+2} \Big] \left(||0\rangle\rangle\,\langle\langle 0|| + ||1\rangle\rangle\,\langle\langle 1||\right)^{\otimes L/2-2}
\end{aligned}
$$

We now use the upper sign in $\pm$ or $\mp$ to denote hard-core bosonic systems, and the lower sign to denote fermionic systems.

$$
e^{iH_0 t} e^{-i(H_0+H_{\bowtie})t}
$$

$$
\begin{aligned}
& \left(|0\rangle\,||0\rangle\rangle + |1\rangle\,||1\rangle\rangle\right) \otimes \left(|0\rangle\,||0\rangle\rangle + |1\rangle\,||1\rangle\rangle\right) \otimes \left(|0\rangle\,||0\rangle\rangle + |1\rangle\,||1\rangle\rangle\right) \otimes \left(|0\rangle\,||0\rangle\rangle + |1\rangle\,||1\rangle\rangle\right) \\
& = \left(1 - itH_{\bowtie} - \frac{t^2}{2}H_{\bowtie}^2 + \frac{t^2}{2}[H_0, H_{\bowtie}] + O(t^3)\right) \\
& \left(|0\rangle\,||0\rangle\rangle + |1\rangle\,||1\rangle\rangle\right) \otimes \left(|0\rangle\,||0\rangle\rangle + |1\rangle\,||1\rangle\rangle\right) \otimes \left(|0\rangle\,||0\rangle\rangle + |1\rangle\,||1\rangle\rangle\right) \otimes \left(|0\rangle\,||0\rangle\rangle + |1\rangle\,||1\rangle\rangle\right) \\
& = \left(1 + it\left(\hat{c}_\beta^\dagger \hat{c}_\gamma + \text{h.c.}\right) - \frac{t^2}{2}\left(\hat{n}_\beta(\hat{1} - \hat{n}_\gamma) + \hat{n}_\gamma(\hat{1} - \hat{n}_\beta\right) + \frac{t^2}{2}\left(\hat{c}_\alpha^\dagger \hat{c}_\gamma - \hat{c}_\beta^\dagger \hat{c}_\delta - \text{h.c.}\right) + O(t^3)\right) \\
& \left(|0\rangle\,||0\rangle\rangle + |1\rangle\,||1\rangle\rangle\right)_\alpha \otimes \left(|0\rangle\,||0\rangle\rangle + |1\rangle\,||1\rangle\rangle\right)_\beta \otimes \left(|0\rangle\,||0\rangle\rangle + |1\rangle\,||1\rangle\rangle\right)_\gamma \otimes \left(|0\rangle\,||0\rangle\rangle + |1\rangle\,||1\rangle\rangle\right)_\delta \\
& = \left(|0\rangle\,||0\rangle\rangle + |1\rangle\,||1\rangle\rangle\right)_\alpha \otimes \left(|0\rangle\,||0\rangle\rangle + |1\rangle\,||1\rangle\rangle\right)_\beta \otimes \left(|0\rangle\,||0\rangle\rangle + |1\rangle\,||1\rangle\rangle\right)_\gamma \otimes \left(|0\rangle\,||0\rangle\rangle + |1\rangle\,||1\rangle\rangle\right)_\delta \\
& + it\left(|0\rangle\,||0\rangle\rangle + |1\rangle\,||1\rangle\rangle\right)_\alpha \otimes \left(|0\rangle\,||1\rangle\rangle\right)_\beta \otimes \left(|1\rangle\,||0\rangle\rangle\right)_\gamma \otimes \left(|0\rangle\,||0\rangle\rangle + |1\rangle\,||1\rangle\rangle\right)_\delta \\
& + it\left(|0\rangle\,||0\rangle\rangle + |1\rangle\,||1\rangle\rangle\right)_\alpha \otimes \left(|1\rangle\,||0\rangle\rangle\right)_\beta \otimes \left(|0\rangle\,||1\rangle\rangle\right)_\gamma \otimes \left(|0\rangle\,||0\rangle\rangle + |1\rangle\,||1\rangle\rangle\right)_\delta \\
& - \frac{t^2}{2}\left(|0\rangle\,||0\rangle\rangle + |1\rangle\,||1\rangle\rangle\right)_\alpha \otimes \left(|1\rangle\,||1\rangle\rangle\right)_\beta \otimes \left(|0\rangle\,||0\rangle\rangle\right)_\gamma \otimes \left(|0\rangle\,||0\rangle\rangle + |1\rangle\,||1\rangle\rangle\right)_\delta \\
& - \frac{t^2}{2}\left(|0\rangle\,||0\rangle\rangle + |1\rangle\,||1\rangle\rangle\right)_\alpha \otimes \left(|0\rangle\,||0\rangle\rangle\right)_\beta \otimes \left(|1\rangle\,||1\rangle\rangle\right)_\gamma \otimes \left(|0\rangle\,||0\rangle\rangle + |1\rangle\,||1\rangle\rangle\right)_\delta \\
& + \frac{t^2}{2}\left(|0\rangle\,||1\rangle\rangle\right)_\alpha \otimes \left(|0\rangle\,||0\rangle\rangle \pm |1\rangle\,||1\rangle\rangle\right)_\beta \otimes \left(|1\rangle\,||0\rangle\rangle\right)_\gamma \otimes \left(|0\rangle\,||0\rangle\rangle + |1\rangle\,||1\rangle\rangle\right)_\delta \\
& - \frac{t^2}{2}\left(|0\rangle\,||0\rangle\rangle + |1\rangle\,||1\rangle\rangle\right)_\alpha \otimes \left(|0\rangle\,||1\rangle\rangle\right)_\beta \otimes \left(|0\rangle\,||0\rangle\rangle \pm |1\rangle\,||1\rangle\rangle\right)_\gamma \otimes \left(|1\rangle\,||0\rangle\rangle\right)_\delta \\
& - \frac{t^2}{2}\left(|1\rangle\,||0\rangle\rangle\right)_\alpha \otimes \left(|0\rangle\,||0\rangle\rangle \pm |1\rangle\,||1\rangle\rangle\right)_\beta \otimes \left(|0\rangle\,||1\rangle\rangle\right)_\gamma \otimes \left(|0\rangle\,||0\rangle\rangle + |1\rangle\,||1\rangle\rangle\right)_\delta \\
& + \frac{t^2}{2}\left(|0\rangle\,||0\rangle\rangle + |1\rangle\,||1\rangle\rangle\right)_\alpha \otimes \left(|1\rangle\,||0\rangle\rangle\right)_\beta \otimes \left(|0\rangle\,||0\rangle\rangle \pm |1\rangle\,||1\rangle\rangle\right)_\gamma \otimes \left(|0\rangle\,||1\rangle\rangle\right)_\delta + O(t^3)
\end{aligned}
$$

$$
\begin{aligned}
\rho_{AC} = \frac{2^{L/2-2}}{2^L} & \left(|0\rangle\,||0\rangle\rangle + |1\rangle\,||1\rangle\rangle\right)^{\otimes L/2-2} \left(\langle 0|\,\langle\langle 0|| + \langle 1|\,\langle\langle 1||\right)^{\otimes L/2-2} \\
& \sum_{i,j,k,l=0}^{1} \Bigg[\mathbb{1}_{L/2-1} \otimes \mathbb{1}_{L/2} \otimes \langle i|\,\langle\langle j||_{L/2+1} \otimes \langle k|\,\langle\langle l||_{L/2+2} \\
& \Bigg[\left(|0\rangle\,||0\rangle\rangle + |1\rangle\,||1\rangle\rangle\right) \otimes \left(|0\rangle\,||0\rangle\rangle + |1\rangle\,||1\rangle\rangle\right) \otimes \left(|0\rangle\,||0\rangle\rangle + |1\rangle\,||1\rangle\rangle\right) \otimes \left(|0\rangle\,||0\rangle\rangle + |1\rangle\,||1\rangle\rangle\right) \\
& + it \left(|0\rangle\,||0\rangle\rangle + |1\rangle\,||1\rangle\rangle\right) \otimes \left(|0\rangle\,||1\rangle\rangle\right) \otimes \left(|1\rangle\,||0\rangle\rangle\right) \otimes \left(|0\rangle\,||0\rangle\rangle + |1\rangle\,||1\rangle\rangle\right) \\
& + it \left(|0\rangle\,||0\rangle\rangle + |1\rangle\,||1\rangle\rangle\right) \otimes \left(|1\rangle\,||0\rangle\rangle\right) \otimes \left(|0\rangle\,||1\rangle\rangle\right) \otimes \left(|0\rangle\,||0\rangle\rangle + |1\rangle\,||1\rangle\rangle\right) \\
& - \frac{t^2}{2} \left(|0\rangle\,||0\rangle\rangle + |1\rangle\,||1\rangle\rangle\right) \otimes \left(|1\rangle\,||1\rangle\rangle\right) \otimes \left(|0\rangle\,||0\rangle\rangle\right) \otimes \left(|0\rangle\,||0\rangle\rangle + |1\rangle\,||1\rangle\rangle\right) \\
& - \frac{t^2}{2} \left(|0\rangle\,||0\rangle\rangle + |1\rangle\,||1\rangle\rangle\right) \otimes \left(|0\rangle\,||0\rangle\rangle\right) \otimes \left(|1\rangle\,||1\rangle\rangle\right) \otimes \left(|0\rangle\,||0\rangle\rangle + |1\rangle\,||1\rangle\rangle\right) \\
& + \frac{t^2}{2} \left(|0\rangle\,||1\rangle\rangle\right) \otimes \left(|0\rangle\,||0\rangle\rangle \pm |1\rangle\,||1\rangle\rangle\right) \otimes \left(|1\rangle\,||0\rangle\rangle\right) \otimes \left(|0\rangle\,||0\rangle\rangle + |1\rangle\,||1\rangle\rangle\right) \\
& - \frac{t^2}{2} \left(|0\rangle\,||0\rangle\rangle + |1\rangle\,||1\rangle\rangle\right) \otimes \left(|0\rangle\,||1\rangle\rangle\right) \otimes \left(|0\rangle\,||0\rangle\rangle \pm |1\rangle\,||1\rangle\rangle\right) \otimes \left(|1\rangle\,||0\rangle\rangle\right) \\
& - \frac{t^2}{2} \left(|1\rangle\,||0\rangle\rangle\right) \otimes \left(|0\rangle\,||0\rangle\rangle \pm |1\rangle\,||1\rangle\rangle\right) \otimes \left(|0\rangle\,||1\rangle\rangle\right) \otimes \left(|0\rangle\,||0\rangle\rangle + |1\rangle\,||1\rangle\rangle\right) \\
& + \frac{t^2}{2} \left(|0\rangle\,||0\rangle\rangle + |1\rangle\,||1\rangle\rangle\right) \otimes \left(|1\rangle\,||0\rangle\rangle\right) \otimes \left(|0\rangle\,||0\rangle\rangle \pm |1\rangle\,||1\rangle\rangle\right) \otimes \left(|0\rangle\,||1\rangle\rangle\right) \Bigg]
\end{aligned}
$$

$$
\Big[\left(\langle 0| \langle\langle 0|| + \langle 1| \langle\langle 1||\right) \otimes \left(\langle 0| \langle\langle 0|| + \langle 1| \langle\langle 1||\right) \otimes \left(\langle 0| \langle\langle 0|| + \langle 1| \langle\langle 1||\right) \otimes \left(\langle 0| \langle\langle 0|| + \langle 1| \langle\langle 1||\right)
$$

$$
- it \left(\langle 0| \langle\langle 0|| + \langle 1| \langle\langle 1||\right) \otimes \left(\langle 0| \langle\langle 1||\right) \otimes \left(\langle 1| \langle\langle 0||\right) \otimes \left(\langle 0| \langle\langle 0|| + \langle 1| \langle\langle 1||\right)
$$

$$
- it \left(\langle 0| \langle\langle 0|| + \langle 1| \langle\langle 1||\right) \otimes \left(\langle 1| \langle\langle 0||\right) \otimes \left(\langle 0| \langle\langle 1||\right) \otimes \left(\langle 0| \langle\langle 0|| + \langle 1| \langle\langle 1||\right)
$$

$$
- \frac{t^2}{2} \left(\langle 0| \langle\langle 0|| + \langle 1| \langle\langle 1||\right) \otimes \left(\langle 1| \langle\langle 1||\right) \otimes \left(\langle 0| \langle\langle 0||\right) \otimes \left(\langle 0| \langle\langle 0|| + \langle 1| \langle\langle 1||\right)
$$

$$
- \frac{t^2}{2} \left(\langle 0| \langle\langle 0|| + \langle 1| \langle\langle 1||\right) \otimes \left(\langle 0| \langle\langle 0||\right) \otimes \left(\langle 1| \langle\langle 1||\right) \otimes \left(\langle 0| \langle\langle 0|| + \langle 1| \langle\langle 1||\right)
$$

$$
+ \frac{t^2}{2} \left(\langle 0| \langle\langle 1||\right) \otimes \left(\langle 0| \langle\langle 0|| \pm \langle 1| \langle\langle 1||\right) \otimes \left(\langle 1| \langle\langle 0||\right) \otimes \left(\langle 0| \langle\langle 0|| + \langle 1| \langle\langle 1||\right)
$$

$$
- \frac{t^2}{2} \left(\langle 0| \langle\langle 0|| + \langle 1| \langle\langle 1||\right) \otimes \left(\langle 0| \langle\langle 1||\right) \otimes \left(\langle 0| \langle\langle 0|| \pm \langle 1| \langle\langle 1||\right) \otimes \left(\langle 1| \langle\langle 0||\right)
$$

$$
- \frac{t^2}{2} \left(\langle 1| \langle\langle 0||\right) \otimes \left(\langle 0| \langle\langle 0|| \pm \langle 1| \langle\langle 1||\right) \otimes \left(\langle 0| \langle\langle 1||\right) \otimes \left(\langle 0| \langle\langle 0|| + \langle 1| \langle\langle 1||\right)
$$

$$
+ \frac{t^2}{2} \left(\langle 0| \langle\langle 0|| + \langle 1| \langle\langle 1||\right) \otimes \left(\langle 1| \langle\langle 0||\right) \otimes \left(\langle 0| \langle\langle 0|| \pm \langle 1| \langle\langle 1||\right) \otimes \left(\langle 0| \langle\langle 1||\right) \Big]
$$

$$
\mathbb{1}_{L/2-1} \otimes \mathbb{1}_{L/2} \otimes |i\rangle \, ||j\rangle\rangle_{L/2+1} \otimes |k\rangle \, ||l\rangle\rangle_{L/2+2} \Bigg] + O(t^3)
$$

$$\rho_{AC} = \frac{2^{L/2-2}}{2^L} \left(|0\rangle\rangle + |1\rangle\rangle\right)^{\otimes L/2-2} \left(\langle\langle 0| + \langle\langle 1|\right)^{\otimes L/2-2} \Bigg[$$
$$\left(|0\rangle\rangle + |1\rangle\rangle\right) \otimes \left(|0\rangle\rangle + \left(1 - \frac{t^2}{2}\right)|1\rangle\rangle\right)$$
$$\left(\langle\langle 0| + \langle\langle 1|\right) \otimes \left(\langle\langle 0| + \left(1 - \frac{t^2}{2}\right)\langle\langle 1|\right)$$
$$+ \left(|0\rangle\rangle + |1\rangle\rangle\right) \otimes \left(|0\rangle\rangle + \left(1 - \frac{t^2}{2}\right)|1\rangle\rangle\right)$$
$$\left(\langle\langle 0| + \langle\langle 1|\right) \otimes \left(\langle\langle 0| + \left(1 - \frac{t^2}{2}\right)\langle\langle 1|\right)$$
$$+ t^2 \left(|0\rangle\rangle \pm |1\rangle\rangle\right) \otimes \left(|1\rangle\rangle\right) \left(\langle\langle 0| \pm \langle\langle 1|\right) \otimes \left(\langle\langle 0|\right)$$
$$+ t^2 \left(|0\rangle\rangle \pm |1\rangle\rangle\right) \otimes \left(|1\rangle\rangle\right) \left(\langle\langle 0| \pm \langle\langle 1|\right) \otimes \left(\langle\langle 0|\right)$$
$$+ t^2 \left(|0\rangle\rangle \pm |1\rangle\rangle\right) \otimes \left(|0\rangle\rangle\right) \left(\langle\langle 0| \pm \langle\langle 1|\right) \otimes \left(\langle\langle 1|\right)$$
$$+ t^2 \left(|0\rangle\rangle \pm |1\rangle\rangle\right) \otimes \left(|0\rangle\rangle\right) \left(\langle\langle 0| \pm \langle\langle 1|\right) \otimes \left(\langle\langle 1|\right)$$
$$+ \left(|0\rangle\rangle + |1\rangle\rangle\right) \otimes \left(\left(1 - \frac{t^2}{2}\right)|0\rangle\rangle + |1\rangle\rangle\right)$$
$$\left(\langle\langle 0| + \langle\langle 1|\right) \otimes \left(\left(1 - \frac{t^2}{2}\right)\langle\langle 0| + \langle\langle 1|\right)$$
$$+ \left(|0\rangle\rangle + |1\rangle\rangle\right) \otimes \left(\left(1 - \frac{t^2}{2}\right)|0\rangle\rangle + |1\rangle\rangle\right)$$
$$\left(\langle\langle 0| + \langle\langle 1|\right) \otimes \left(\left(1 - \frac{t^2}{2}\right)\langle\langle 0| + \langle\langle 1|\right)\Bigg] + O(t^3)$$

$$
\begin{aligned}
&= \frac{2^{L/2-1}}{2^L} \left(|0\rangle\rangle + |1\rangle\rangle\right)^{\otimes L/2-2} \left(\langle\langle 0| + \langle\langle 1|\right)^{\otimes L/2-2} \Bigg[\\
&\left(|0\rangle\rangle + |1\rangle\rangle\right) \otimes \left(|0\rangle\rangle + \left(1 - \frac{t^2}{2}\right)|1\rangle\rangle\right) \\
&\left(\langle\langle 0| + \langle\langle 1|\right) \otimes \left(\langle\langle 0| + \left(1 - \frac{t^2}{2}\right)\langle\langle 1|\right) \\
&+ t^2 \left(|0\rangle\rangle \pm |1\rangle\rangle\right) \otimes \left(|1\rangle\rangle\right) \left(\langle\langle 0| \pm \langle\langle 1|\right) \otimes \left(\langle\langle 0|\right) \\
&+ t^2 \left(|0\rangle\rangle \pm |1\rangle\rangle\right) \otimes \left(|0\rangle\rangle\right) \left(\langle\langle 0| \pm \langle\langle 1|\right) \otimes \left(\langle\langle 1|\right) \\
&+ \left(|0\rangle\rangle + |1\rangle\rangle\right) \otimes \left(\left(1 - \frac{t^2}{2}\right)|0\rangle\rangle + |1\rangle\rangle\right) \\
&\left(\langle\langle 0| + \langle\langle 1|\right) \otimes \left(\left(1 - \frac{t^2}{2}\right)\langle\langle 0| + \langle\langle 1|\right)\Bigg] + O(t^3) \\
&= \frac{2^{L/2-1}}{2^L} \left(|0\rangle\rangle + |1\rangle\rangle\right)^{\otimes L/2-2} \left(\langle\langle 0| + \langle\langle 1|\right)^{\otimes L/2-2} \Bigg[\\
&(2 - t^2) \sum_{jk} |j\rangle\rangle \otimes |k\rangle\rangle \sum_{lm} \langle\langle l| \otimes \langle\langle m| \\
&+ t^2 \left(|0\rangle\rangle \pm |1\rangle\rangle\right) \left(\langle\langle 0| \pm \langle\langle 1|\right) \otimes \left(|1\rangle\rangle\right) |0\rangle\rangle \langle\langle 1| + |0\rangle\rangle |1\rangle\rangle \langle\langle 0| \left(\langle\langle 1|\right) \\
&\Bigg] + O(t^3)
\end{aligned}
$$

The eigenvalues of the matrix describing the sites close to the boundary can be calculated and they are $\{0, \frac{t^2}{4}, \frac{t^2}{4}, 1 - \frac{t^2}{2}\} + O(t^3)$, (for both fermions and hard-core bosons), which implies that ρ_{AC} will have the same three non-vanishing eigenvalues up to second order in t.

$$
\begin{aligned}
\rho_{AD} = & \frac{1}{2^L} \left(|0\rangle \langle 0| + |1\rangle \langle 1| \right)^{\otimes L/2-2} \\
& \sum_{i,j,k,l=0}^{1} \Bigg[\langle\langle i| |_{L/2-1} \otimes \langle\langle j| |_{L/2} \otimes \langle k|_{L/2+1} \otimes \langle l|_{L/2+2} \\
& \Bigg[(|0\rangle ||0\rangle\rangle + |1\rangle ||1\rangle\rangle) \otimes (|0\rangle ||0\rangle\rangle + |1\rangle ||1\rangle\rangle) \otimes (|0\rangle ||0\rangle\rangle + |1\rangle ||1\rangle\rangle) \otimes (|0\rangle ||0\rangle\rangle + |1\rangle ||1\rangle\rangle) \\
& + it \, (|0\rangle ||0\rangle\rangle + |1\rangle ||1\rangle\rangle) \otimes (|0\rangle ||1\rangle\rangle) \otimes (|1\rangle ||0\rangle\rangle) \otimes (|0\rangle ||0\rangle\rangle + |1\rangle ||1\rangle\rangle) \\
& + it \, (|0\rangle ||0\rangle\rangle + |1\rangle ||1\rangle\rangle) \otimes (|1\rangle ||0\rangle\rangle) \otimes (|0\rangle ||1\rangle\rangle) \otimes (|0\rangle ||0\rangle\rangle + |1\rangle ||1\rangle\rangle) \\
& - \frac{t^2}{2} \, (|0\rangle ||0\rangle\rangle + |1\rangle ||1\rangle\rangle) \otimes (|1\rangle ||1\rangle\rangle) \otimes (|0\rangle ||0\rangle\rangle) \otimes (|0\rangle ||0\rangle\rangle + |1\rangle ||1\rangle\rangle) \\
& - \frac{t^2}{2} \, (|0\rangle ||0\rangle\rangle + |1\rangle ||1\rangle\rangle) \otimes (|0\rangle ||0\rangle\rangle) \otimes (|1\rangle ||1\rangle\rangle) \otimes (|0\rangle ||0\rangle\rangle + |1\rangle ||1\rangle\rangle) \\
& + \frac{t^2}{2} \, (|0\rangle ||1\rangle\rangle) \otimes (|0\rangle ||0\rangle\rangle \pm |1\rangle ||1\rangle\rangle) \otimes (|1\rangle ||0\rangle\rangle) \otimes (|0\rangle ||0\rangle\rangle + |1\rangle ||1\rangle\rangle) \\
& - \frac{t^2}{2} \, (|0\rangle ||0\rangle\rangle + |1\rangle ||1\rangle\rangle) \otimes (|0\rangle ||1\rangle\rangle) \otimes (|0\rangle ||0\rangle\rangle \pm |1\rangle ||1\rangle\rangle) \otimes (|1\rangle ||0\rangle\rangle) \\
& - \frac{t^2}{2} \, (|1\rangle ||0\rangle\rangle) \otimes (|0\rangle ||0\rangle\rangle \pm |1\rangle ||1\rangle\rangle) \otimes (|0\rangle ||1\rangle\rangle) \otimes (|0\rangle ||0\rangle\rangle + |1\rangle ||1\rangle\rangle) \\
& + \frac{t^2}{2} \, (|0\rangle ||0\rangle\rangle + |1\rangle ||1\rangle\rangle) \otimes (|1\rangle ||0\rangle\rangle) \otimes (|0\rangle ||0\rangle\rangle \pm |1\rangle ||1\rangle\rangle) \otimes (|0\rangle ||1\rangle\rangle) \Bigg]
\end{aligned}
$$

$$
\Big[(\langle 0| \langle\langle 0|| + \langle 1| \langle\langle 1||) \otimes (\langle 0| \langle\langle 0|| + \langle 1| \langle\langle 1||) \otimes (\langle 0| \langle\langle 0|| + \langle 1| \langle\langle 1||) \otimes (\langle 0| \langle\langle 0|| + \langle 1| \langle\langle 1||)
$$

$$
- it\, (\langle 0| \langle\langle 0|| + \langle 1| \langle\langle 1||) \otimes (\langle 0| \langle\langle 1||) \otimes (\langle 1| \langle\langle 0||) \otimes (\langle 0| \langle\langle 0|| + \langle 1| \langle\langle 1||)
$$

$$
- it\, (\langle 0| \langle\langle 0|| + \langle 1| \langle\langle 1||) \otimes (\langle 1| \langle\langle 0||) \otimes (\langle 0| \langle\langle 1||) \otimes (\langle 0| \langle\langle 0|| + \langle 1| \langle\langle 1||)
$$

$$
- \frac{t^2}{2}\, (\langle 0| \langle\langle 0|| + \langle 1| \langle\langle 1||) \otimes (\langle 1| \langle\langle 1||) \otimes (\langle 0| \langle\langle 0||) \otimes (\langle 0| \langle\langle 0|| + \langle 1| \langle\langle 1||)
$$

$$
- \frac{t^2}{2}\, (\langle 0| \langle\langle 0|| + \langle 1| \langle\langle 1||) \otimes (\langle 0| \langle\langle 0||) \otimes (\langle 1| \langle\langle 1||) \otimes (\langle 0| \langle\langle 0|| + \langle 1| \langle\langle 1||)
$$

$$
+ \frac{t^2}{2}\, (\langle 0| \langle\langle 1||) \otimes (\langle 0| \langle\langle 0|| \pm \langle 1| \langle\langle 1||) \otimes (\langle 1| \langle\langle 0||) \otimes (\langle 0| \langle\langle 0|| + \langle 1| \langle\langle 1||)
$$

$$
- \frac{t^2}{2}\, (\langle 0| \langle\langle 0|| + \langle 1| \langle\langle 1||) \otimes (\langle 0| \langle\langle 1||) \otimes (\langle 0| \langle\langle 0|| \pm \langle 1| \langle\langle 1||) \otimes (\langle 1| \langle\langle 0||)
$$

$$
- \frac{t^2}{2}\, (\langle 1| \langle\langle 0||) \otimes (\langle 0| \langle\langle 0|| \pm \langle 1| \langle\langle 1||) \otimes (\langle 0| \langle\langle 1||) \otimes (\langle 0| \langle\langle 0|| + \langle 1| \langle\langle 1||)
$$

$$
+ \frac{t^2}{2}\, (\langle 0| \langle\langle 0|| + \langle 1| \langle\langle 1||) \otimes (\langle 1| \langle\langle 0||) \otimes (\langle 0| \langle\langle 0|| \pm \langle 1| \langle\langle 1||) \otimes (\langle 0| \langle\langle 1||) \Big]
$$

$$
||i\rangle\rangle_{L/2-1} \otimes ||j\rangle\rangle_{L/2} \otimes |k\rangle_{L/2+1} \otimes |k\rangle\, ||l\rangle\rangle_{L/2+2} \Big] \left(||0\rangle\rangle \langle\langle 0|| + ||1\rangle\rangle \langle\langle 1|| \right)^{\otimes L/2-2} + O(t^3)
$$

$$\rho_{AD} = \frac{1}{2^L} \left(|0\rangle \langle 0| + |1\rangle \langle 1| \right)^{\otimes L/2-2} \Bigg[$$
$$\left(|0\rangle |0\rangle ||0\rangle\rangle ||0\rangle\rangle + it |0\rangle |1\rangle ||1\rangle\rangle ||0\rangle\rangle - \frac{t^2}{2} |1\rangle |0\rangle ||1\rangle\rangle ||0\rangle\rangle + \frac{t^2}{2} |0\rangle |1\rangle ||0\rangle\rangle ||1\rangle\rangle \right)$$
$$\left(\langle 0| \langle 0| \langle\langle 0|| \langle\langle 0|| - it \langle 0| \langle 1| \langle\langle 1|| \langle\langle 0|| - \frac{t^2}{2} \langle 1| \langle 0| \langle\langle 1|| \langle\langle 0|| + \frac{t^2}{2} \langle 0| \langle 1| \langle\langle 0|| \langle\langle 1|| \right)$$
$$+ \left(|0\rangle |0\rangle ||0\rangle\rangle ||1\rangle\rangle \pm it |0\rangle |1\rangle ||1\rangle\rangle ||1\rangle\rangle \mp \frac{t^2}{2} |1\rangle |0\rangle ||1\rangle\rangle ||1\rangle\rangle \right)$$
$$\left(\langle 0| \langle 0| \langle\langle 0|| \langle\langle 1|| \mp it \langle 0| \langle 1| \langle\langle 1|| \langle\langle 1|| \mp \frac{t^2}{2} \langle 1| \langle 0| \langle\langle 1|| \langle\langle 1|| \right)$$
$$+ \left((1 - \frac{t^2}{2}) |0\rangle |0\rangle ||1\rangle\rangle ||0\rangle\rangle + \frac{t^2}{2} |0\rangle |1\rangle ||1\rangle\rangle ||1\rangle\rangle \right) \left((1 - \frac{t^2}{2}) \langle 0| \langle 0| \langle\langle 1|| \langle\langle 0|| + \frac{t^2}{2} \langle 0| \langle 1| \langle\langle 1|| \langle\langle 1|| \right)$$
$$+ \left((1 - \frac{t^2}{2}) |0\rangle |0\rangle ||1\rangle\rangle ||1\rangle\rangle \right) \left((1 - \frac{t^2}{2}) \langle 0| \langle 0| \langle\langle 1|| \langle\langle 1|| \right)$$
$$+ \left((1 - \frac{t^2}{2}) |0\rangle |1\rangle ||0\rangle\rangle ||0\rangle\rangle \mp \frac{t^2}{2} |1\rangle |1\rangle ||1\rangle\rangle ||0\rangle\rangle \right) \left((1 - \frac{t^2}{2}) \langle 0| \langle 1| \langle\langle 0|| \langle\langle 0|| \mp \frac{t^2}{2} \langle 1| \langle 1| \langle\langle 1|| \langle\langle 0|| \right)$$
$$+ \left(\pm (1 - \frac{t^2}{2}) |0\rangle |1\rangle ||0\rangle\rangle ||1\rangle\rangle - \frac{t^2}{2} |0\rangle |0\rangle ||0\rangle\rangle ||0\rangle\rangle \mp \frac{t^2}{2} |1\rangle |1\rangle ||1\rangle\rangle ||1\rangle\rangle \right)$$
$$\left(\pm (1 - \frac{t^2}{2}) \langle 0| \langle 1| \langle\langle 0|| \langle\langle 1|| - \frac{t^2}{2} \langle 0| \langle 0| \langle\langle 0|| \langle\langle 0|| \mp \frac{t^2}{2} \langle 1| \langle 1| \langle\langle 1|| \langle\langle 1|| \right)$$
$$+ (\pm |0\rangle |1\rangle ||1\rangle\rangle ||0\rangle\rangle + it |0\rangle |0\rangle ||0\rangle\rangle ||0\rangle\rangle) (\pm \langle 0| \langle 1| \langle\langle 1|| \langle\langle 0|| - it \langle 0| \langle 0| \langle\langle 0|| \langle\langle 0||)$$

$$
\begin{aligned}
&+\left(|0\rangle|1\rangle||1\rangle\rangle||1\rangle\rangle+it\,|0\rangle|0\rangle||0\rangle\rangle||1\rangle\rangle\mp\frac{t^2}{2}\,|0\rangle|0\rangle||1\rangle\rangle||0\rangle\rangle\right)\\
&\left(\langle 0|\langle 1|\langle\langle 1||\langle\langle 1||-it\,\langle 0|\langle 0|\langle\langle 0||\langle\langle 1||\mp\frac{t^2}{2}\,\langle 0|\langle 0|\langle\langle 1||\langle\langle 0||\right)\\
&+\left(|1\rangle|0\rangle||0\rangle\rangle||0\rangle\rangle+it\,|1\rangle|1\rangle||1\rangle\rangle||0\rangle\rangle+\frac{t^2}{2}\,|1\rangle|1\rangle||0\rangle\rangle||1\rangle\rangle\right)\\
&\left(\langle 1|\langle 0|\langle\langle 0||\langle\langle 0||-it\,\langle 1|\langle 1|\langle\langle 1||\langle\langle 0||+\frac{t^2}{2}\,\langle 1|\langle 1|\langle\langle 0||\langle\langle 1||\right)\\
&+(\pm|1\rangle|0\rangle||0\rangle\rangle||1\rangle\rangle+it\,|1\rangle|1\rangle||1\rangle\rangle||1\rangle\rangle)\,(\pm\langle 1|\langle 0|\langle\langle 0||\langle\langle 1||-it\,\langle 1|\langle 1|\langle\langle 1||\langle\langle 1||)\\
&+\left(\pm(1-\frac{t^2}{2})\,|1\rangle|0\rangle||1\rangle\rangle||0\rangle\rangle+\frac{t^2}{2}\,|0\rangle|0\rangle||0\rangle\rangle||0\rangle\rangle\pm\frac{t^2}{2}\,|1\rangle|1\rangle||1\rangle\rangle||1\rangle\rangle\right)\\
&\left(\pm(1-\frac{t^2}{2})\,\langle 1|\langle 0|\langle\langle 1||\langle\langle 0||+\frac{t^2}{2}\,\langle 0|\langle 0|\langle\langle 0||\langle\langle 0||\pm\frac{t^2}{2}\,\langle 1|\langle 1|\langle\langle 1||\langle\langle 1||\right)\\
&+\left((1-\frac{t^2}{2})\,|1\rangle|0\rangle||1\rangle\rangle||1\rangle\rangle+\frac{t^2}{2}\,|0\rangle|0\rangle||0\rangle\rangle||1\rangle\rangle\right)\left((1-\frac{t^2}{2})\,\langle 1|\langle 0|\langle\langle 1||\langle\langle 1||+\frac{t^2}{2}\,\langle 0|\langle 0|\langle\langle 0||\langle\langle 1||\right)\\
&+\left((1-\frac{t^2}{2})\,|1\rangle|1\rangle||0\rangle\rangle||0\rangle\rangle\right)\left((1-\frac{t^2}{2})\,\langle 1|\langle 1|\langle\langle 0||\langle\langle 0||\right)\\
&+\left((1-\frac{t^2}{2})\,|1\rangle|1\rangle||0\rangle\rangle||1\rangle\rangle\mp\frac{t^2}{2}\,|1\rangle|0\rangle||0\rangle\rangle||0\rangle\rangle\right)\left((1-\frac{t^2}{2})\,\langle 1|\langle 1|\langle\langle 0||\langle\langle 1||\mp\frac{t^2}{2}\,\langle 1|\langle 0|\langle\langle 0||\langle\langle 0||\right)
\end{aligned}
$$

$$
\begin{aligned}
&+\left(|1\rangle|1\rangle||1\rangle\rangle||0\rangle\rangle\pm it\,|1\rangle|0\rangle||0\rangle\rangle||0\rangle\rangle+\frac{t^2}{2}\,|0\rangle|1\rangle||0\rangle\rangle||0\rangle\rangle\right)\\
&\left(\langle 1|\langle 1|\langle\langle 1||\langle\langle 0||\mp it\,\langle 1|\langle 0|\langle\langle 0||\langle\langle 0||+\frac{t^2}{2}\,\langle 0|\langle 1|\langle\langle 0||\langle\langle 0||\right)\\
&+\left(|1\rangle|1\rangle||1\rangle\rangle||1\rangle\rangle+it\,|1\rangle|0\rangle||0\rangle\rangle||1\rangle\rangle\pm\frac{t^2}{2}\,|0\rangle|1\rangle||0\rangle\rangle||1\rangle\rangle\mp\frac{t^2}{2}\,|1\rangle|0\rangle||1\rangle\rangle||0\rangle\rangle\right)\\
&\left(\langle 1|\langle 1|\langle\langle 1||\langle\langle 1||-it\,\langle 1|\langle 0|\langle\langle 0||\langle\langle 1||\pm\frac{t^2}{2}\,\langle 0|\langle 1|\langle\langle 0||\langle\langle 1||\mp\frac{t^2}{2}\,\langle 1|\langle 0|\langle\langle 1||\langle\langle 0||\right)\\
&\Big](||0\rangle\rangle\langle\langle 0||+||1\rangle\rangle\langle\langle 1||)^{\otimes L/2-2}+O(t^3)
\end{aligned}
$$

For hard-core bosons this matrix is diagonal with eigenvalues $1+t^2$ or $1-t^2$ with equal multiplicity, which means that $S^{(2)}_{AD}(t)=L+O(t^3)$ and $I^{(2)}_3=-S^{(2)}_{AC}+O(t^3)=-t^2/\log(2)+O(t^3)$.

For the free-fermion case, we now neglect the off-diagonal elements of order t^2 since they do not change the eigenvalues in the second order.

$$
\begin{aligned}
\rho_{AD} = \frac{1}{2^L} \left(|0\rangle\langle 0| + |1\rangle\langle 1|\right)^{\otimes L/2-2} \Bigg[\\
&(|0\rangle|0\rangle||0\rangle\rangle||0\rangle\rangle + it\,|0\rangle|1\rangle||1\rangle\rangle||0\rangle\rangle)\,(\langle 0|\langle 0|\langle\langle 0||\langle\langle 0|| - it\,\langle 0|\langle 1|\langle\langle 1||\langle\langle 0||) \\
&+ (|0\rangle|0\rangle||0\rangle\rangle||1\rangle\rangle \pm it\,|0\rangle|1\rangle||1\rangle\rangle||1\rangle\rangle)\,(\langle 0|\langle 0|\langle\langle 0||\langle\langle 1|| \mp it\,\langle 0|\langle 1|\langle\langle 1||\langle\langle 1||) \\
&+ (1-t^2)\,|0\rangle|0\rangle||1\rangle\rangle||0\rangle\rangle\,\langle 0|\langle 0|\langle\langle 1||\langle\langle 0|| \\
&+ (1-t^2)\,|0\rangle|0\rangle||1\rangle\rangle||1\rangle\rangle\,\langle 0|\langle 0|\langle\langle 1||\langle\langle 1|| \\
&+ (1-t^2)\,|0\rangle|1\rangle||0\rangle\rangle||0\rangle\rangle\,\langle 0|\langle 1|\langle\langle 0||\langle\langle 0|| \\
&+ (1-t^2)\,|0\rangle|1\rangle||0\rangle\rangle||1\rangle\rangle\,\langle 0|\langle 1|\langle\langle 0||\langle\langle 1|| \\
&+ (\pm|0\rangle|1\rangle||1\rangle\rangle||0\rangle\rangle + it\,|0\rangle|0\rangle||0\rangle\rangle||0\rangle\rangle)\,(\pm\langle 0|\langle 1|\langle\langle 1||\langle\langle 0|| - it\,\langle 0|\langle 0|\langle\langle 0||\langle\langle 0||) \\
&+ (|0\rangle|1\rangle||1\rangle\rangle||1\rangle\rangle + it\,|0\rangle|0\rangle||0\rangle\rangle||1\rangle\rangle)\,(\langle 0|\langle 1|\langle\langle 1||\langle\langle 1|| - it\,\langle 0|\langle 0|\langle\langle 0||\langle\langle 1||) \\
&+ (|1\rangle|0\rangle||0\rangle\rangle||0\rangle\rangle + it\,|1\rangle|1\rangle||1\rangle\rangle||0\rangle\rangle)\,(\langle 1|\langle 0|\langle\langle 0||\langle\langle 0|| - it\,\langle 1|\langle 1|\langle\langle 1||\langle\langle 0||) \\
&+ (\pm|1\rangle|0\rangle||0\rangle\rangle||1\rangle\rangle + it\,|1\rangle|1\rangle||1\rangle\rangle||1\rangle\rangle)\,(\pm\langle 1|\langle 0|\langle\langle 0||\langle\langle 1|| - it\,\langle 1|\langle 1|\langle\langle 1||\langle\langle 1||) \\
&+ (1-t^2)\,|1\rangle|0\rangle||1\rangle\rangle||0\rangle\rangle\,\langle 1|\langle 0|\langle\langle 1||\langle\langle 0|| \\
&+ (1-t^2)\,|1\rangle|0\rangle||1\rangle\rangle||1\rangle\rangle\,\langle 1|\langle 0|\langle\langle 1||\langle\langle 1|| \\
&+ (1-t^2)\,|1\rangle|1\rangle||0\rangle\rangle||0\rangle\rangle\,\langle 1|\langle 1|\langle\langle 0||\langle\langle 0|| \\
&+ (1-t^2)\,|1\rangle|1\rangle||0\rangle\rangle||1\rangle\rangle\,\langle 1|\langle 1|\langle\langle 0||\langle\langle 1|| \\
&+ (|1\rangle|1\rangle||1\rangle\rangle||0\rangle\rangle \pm it\,|1\rangle|0\rangle||0\rangle\rangle||0\rangle\rangle)\,(\langle 1|\langle 1|\langle\langle 1||\langle\langle 0|| \mp it\,\langle 1|\langle 0|\langle\langle 0||\langle\langle 0||) \\
&+ (|1\rangle|1\rangle||1\rangle\rangle||1\rangle\rangle + it\,|1\rangle|0\rangle||0\rangle\rangle||1\rangle\rangle)\,(\langle 1|\langle 1|\langle\langle 1||\langle\langle 1|| - it\,\langle 1|\langle 0|\langle\langle 0||\langle\langle 1||) \\
\Bigg] &\left(||0\rangle\rangle\langle\langle 0|| + ||1\rangle\rangle\langle\langle 1||\right)^{\otimes L/2-2} + O(t^3)
\end{aligned}
$$

It is then possible to notice that the matrix can be written in block diagonal form in the sense that the two sites closest to the boundary in A and also D can be described by a matrix with 4 identical 4×4 blocks on the diagonal:

$$
\frac{1}{2^2}\begin{pmatrix}
1-t^2 & 0 & 0 & 0 \\
0 & 1+t^2 & 2it & 0 \\
0 & -2it & 1+t^2 & 0 \\
0 & 0 & 0 & 1-t^2
\end{pmatrix}
$$

So the eigenvalues (that are all identical originally) will be multiplied by the eigenvalues of this block $1-t^2$, $1-t^2$, $(1-t)^2$ and $(1+t)^2$ respectively, where we quickly verify that the

trace is preserved since

$$\mathrm{Tr}\rho_{AD} = \frac{1}{4}\left[(1-t^2)+(1-t^2)+(1-t)^2+(1+t)^2\right]+O(t^3) = 1+O(t^3).$$

We can now expand the logarithm in the collision entropy $S^{(2)}$ around $t=0$ as well to find the small time expansion for the (collision) tripartite information:

Spinless Fermions

$$\begin{aligned} S^{(2)}_{AC} &= t^2/\log(2)+O(t^3) \\ S^{(2)}_{AD} &= L-2t^2/\log(2)+O(t^3) \\ I^{(2)}_3 &= L-(S^{(2)}_{AC}+S^{(2)}_{AD}) = t^2/\log(2)+O(t^3). \end{aligned}$$

Hardcore Bosons

$$\begin{aligned} S^{(2)}_{AC} &= t^2/\log(2)+O(t^3) \\ S^{(2)}_{AD} &= L+O(t^3) \\ I^{(2)}_3 &= L-(S^{(2)}_{AC}+S^{(2)}_{AD}) = -t^2/\log(2)+O(t^3). \end{aligned}$$

These results (and the results for the eigenvalues) are consistent with our numerical results for $L=10$ and small times.

Appendix E

Quenches in the Completely Connected Transverse Field Ising Model

We also investigated the transverse field Ising model on a completely connected graph (also known as the Lipkin-Meshkov-Glick model [LMG65]). Because the model is completely connected, the dynamics can be restricted to the subspace of site permutation symmetric states, which is an extremely strong restriction that breaks down the dimensionality of the Hilbert space from exponential to linear in the system size, as the states can be identified by the total number of up or down spins [SB11]. The Hamiltonian appears as follows [SB11; HK19]:

$$H = -\frac{J}{2N}\sum_{ij} S_i^z S_j^z - \Gamma \sum_i S_i^x, \tag{E.1}$$

where N is the system size and we pick natural units with $J = 1$. The system undergoes a quantum phase transition at a critical transverse field $\Gamma_c = \frac{1}{2}$, where the ground state is a z-ferromagnet for $\Gamma < \Gamma_c$ and a quantum paramagnet for $\Gamma > \Gamma_c$ [Das+06].

Starting point for the numerical calculation is an effective Hamiltonian constrained to the permutation symmetric Dicke subspace [SB11; HK19], where we first define the magnetization per site:

$$s = \frac{N^+}{N} - \frac{1}{2}, \tag{E.2}$$

which allows us to write down the effective Hamiltonian more compactly:

$$\langle \tilde{N}^+ | \hat{H} | N^+ \rangle = -\frac{s^2}{2}\delta_{N^+,\tilde{N}^+} - \frac{\Gamma\sqrt{0.25 - s^2}}{2}\delta_{N^+,\tilde{N}^+\pm 1}, \quad N^+, \tilde{N}^+ \in \{0, 1, \dots, N\} \tag{E.3}$$

The full derivation can be found in Appendix A of Homrighausen and Kehrein [HK19].

We diagonalize the Hamiltonian numerically:

$$\hat{H}\left|\Psi_n\right\rangle = E_n\left|\Psi_n\right\rangle, \quad n \in \{0, 1, ..., N\}, \tag{E.4}$$

and construct the thermofield double state:

$$\left|U(t)\right\rangle_\beta = \sum_{n=0}^{N} e^{-\beta E_n/2}\left|\Psi_n\right\rangle \otimes e^{-iE_n t}\left|\Psi_n\right\rangle \tag{E.5}$$

$$= \sum_{N_{AB}^+=0}^{N}\sum_{N_{CD}^+=0}^{N} m_{N_{AB}^+,N_{CD}^+}\left|N_{AB}^+\right\rangle \otimes \left|N_{CD}^+\right\rangle, \tag{E.6}$$

$$\rho_{\text{TFD}} = \left|U(t)\right\rangle_\beta\left\langle U(t)\right|, \tag{E.7}$$

where we have defined the vector elements $\mathbf{m}$ of $|U(t)\rangle$.

The Dicke states can be split into two permutation symmetric subspaces [HK19]:

$$\left|N^+\right\rangle = \sum_{A^+ + B^+ = N^+} \sqrt{\frac{\binom{N_A}{A^+}\binom{N_B}{B^+}}{\binom{N}{N^+}}}\left|A^+\right\rangle\left|B^+\right\rangle. \tag{E.8}$$

We can now calculate reduced density matrices of this state, e.g. ρ_{AC}:

$$\rho_{AC} = \langle N_A^+, N_C^+|\rho_{\text{TFD}}|\tilde{N}_A^+, \tilde{N}_C^+\rangle \tag{E.9}$$

$$= \sum_{N_B^+=0}^{N_B}\sum_{N_D^+=0}^{N_D} \sqrt{\frac{\binom{N_A}{N_A^+}\binom{N_B}{N_B^+}}{\binom{N}{N_A^+ + N_B^+}}\frac{\binom{N_C}{N_C^+}\binom{N_D}{N_D^+}}{\binom{N}{N_C^+ + N_D^+}}} m_{N_A^+ + N_B^+, N_C^+ + N_D^+}$$

$$\cdot \sqrt{\frac{\binom{N_A}{\tilde{N}_A^+}\binom{N_B}{N_B^+}}{\binom{N}{\tilde{N}_A^+ + N_B^+}}\frac{\binom{N_C}{\tilde{N}_C^+}\binom{N_D}{N_D^+}}{\binom{N}{\tilde{N}_C^+ + N_D^+}}} m_{\tilde{N}_A^+ + N_B^+, \tilde{N}_C^+ + N_D^+}. \tag{E.10}$$

And then compute the tripartite information I_3 as described in Chapter 2.

In contrast to the main part, we want to look at quantum quenches between different val-

ues of the transverse field Γ in this model, which requires some rethinking. To describe the quench $\Gamma_\mathrm{i} \to \Gamma_\mathrm{f}$ we have to construct the initial thermal state using the initial Hamiltonian as $\rho_{AB} = e^{-\beta H(\Gamma_i)}$ and then use the final Hamiltonian for the time evolution $U(t) = e^{-itH(\Gamma_f)}$. Usually, we want to quench from the ground state ($\beta \to \infty$), but in this case the tripartite information would vanish and also the HAAR-averaged value of the tripartite information is only a sensible comparison value in the limit of infinite temperature ($\beta \to 0$). At infinite temperature on the other hand the concept of a quench is meaningless, as the infinite-temperature state is independent of the features of the Hamiltonian. As a compromise, we tried to use intermediate values of β to quench from a thermal state of intermediate temperature.

Because of the quench, the entropies of the time-evolved subsystems C and D are also no longer time-independent and have to be calculated numerically to correctly calculate the tripartite information.

Since we are now interested in the low-lying states of the system, there is the additional complication that in the ferromagnetic phase the ground state has two ergodic components: because the Hamiltonian has a total spin-flip symmetry, there are two minima in the free energy and a naive calculation of the ground state would mix states with the spin pointing along both the positive and the negative z-axis. We instead add a small longitudinal field $h = \mathcal{O}(1/N)$ to the Hamiltonian to break the $\mathbb{Z}_2$ symmetry explicitly to correctly obtain a non-vanishing magnetization in the ferromagnetic phase:

$$\langle \tilde{N}^+ | \hat{H} | N^+ \rangle = -\left(\frac{s^2}{2} + s \cdot h\right) \delta_{N^+,\tilde{N}^+} - \frac{\Gamma\sqrt{0.25 - s^2}}{2} \delta_{N^+,\tilde{N}^+\pm 1}. \tag{E.11}$$

The magnetization has been plotted over the longitudinal field in Fig.E.1, where the field has been rescaled to remove the $1/N$ factor. We see that the ferromagnetic curves collapse until they reach a plateau at about $h = 0.55/N$, which we identify with the appropriate field strength to break the symmetry without affecting the system too much.

We then looked at different quenches and plotted the tripartite information and the magnetization in Figs. E.2,E.3,E.4, and E.5.

We evaluated the frequency of oscillation after the quench inside the paramagnetic phase and compared it to the frequency of the entanglement hamiltonian in Homrighausen and Kehrein [HK19], which is shown in Fig. E.6. The results are consistent with each other as the semi-classical value is approached for large system sizes.

We also calculated an effective inverse temperature β by calculating the post-quench en-

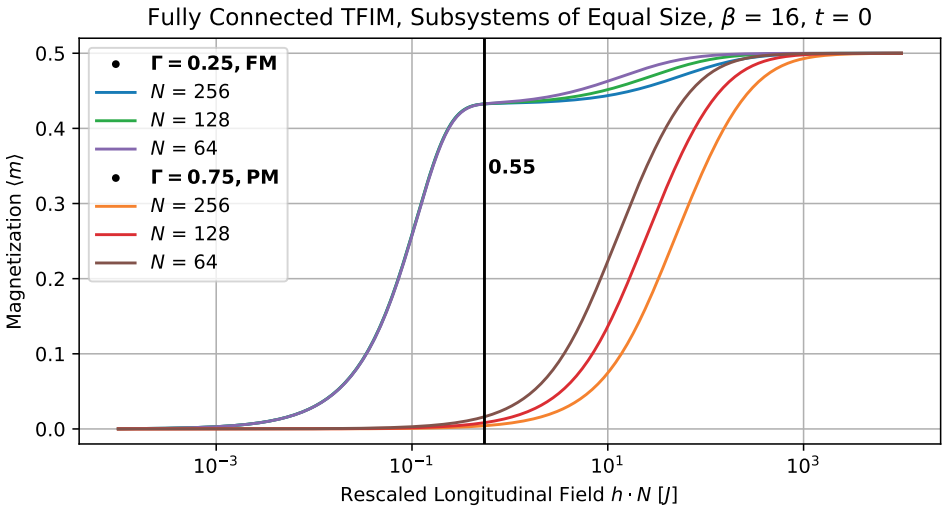

Figure E.1: Magnetization over the small longitudinal field h in the ferromagnetic and paramagnetic phase of the fully connected transverse field ISING model

ergy density and finding the temperature of a GIBBS state with the same energy density using a bisection method. The implementation, in this case, has to take into account that the post-quench temperature can be lower than the original temperature depending on the parameters of the Hamiltonian. We also calculated some higher moments of the magnetization, in particular the skewness and the kurtosis.

We were not certain how to interpret the results at this point, did not continue the project further and because of the doubling of the system size, we still could only reach slightly higher system sizes of 256 sites. In particular, since the Hilbert space dimension scales linearly in the system size, the entropy is not extensive and has to be rescaled with the system size in the free energy to get non-trivial results, and we never really developed a physical understanding of this system. This is also because by construction there is no interpretation of the system as a chain of individual qubits which makes it hard to understand information transport from the point of view of information theory.

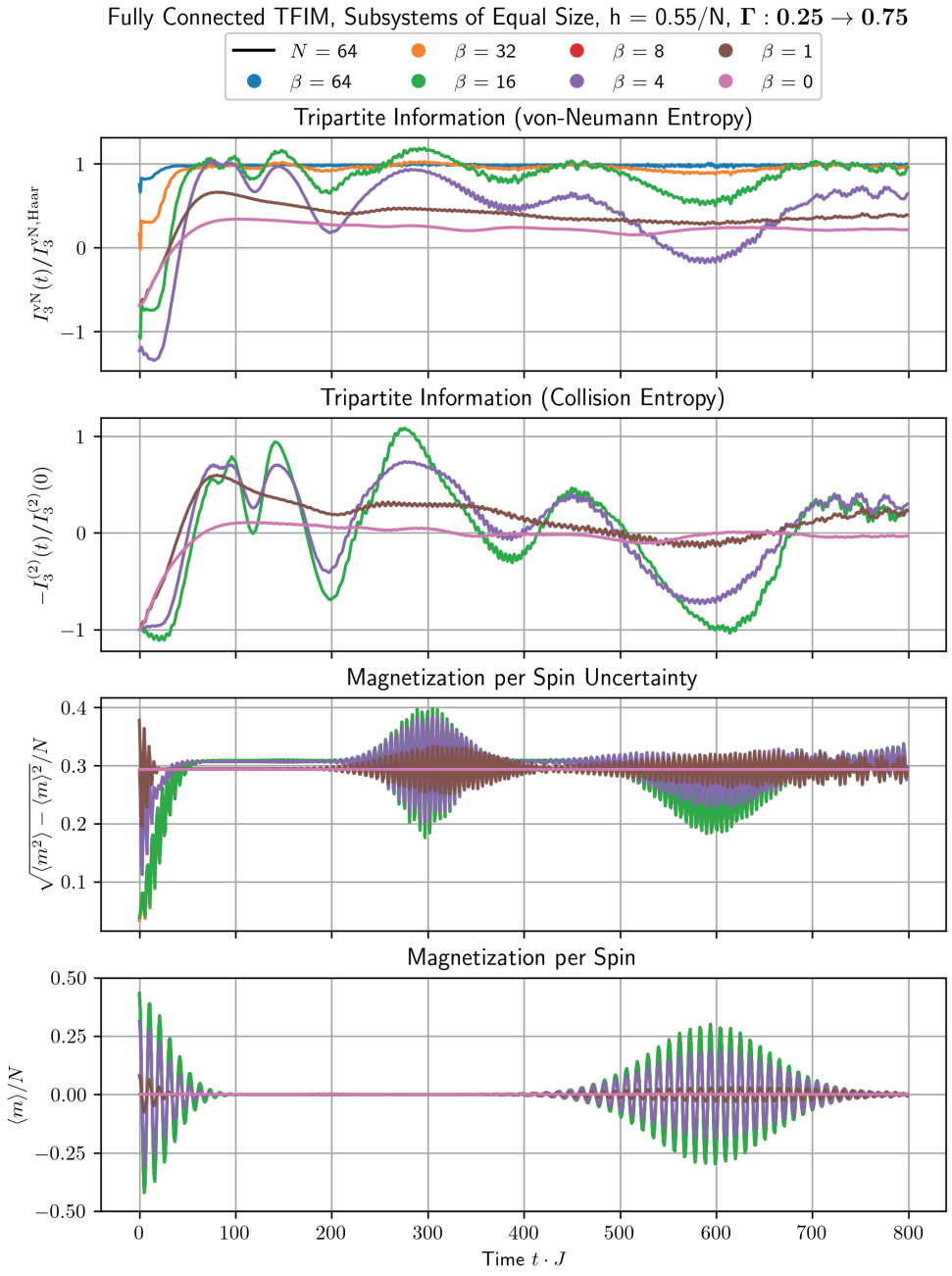

Figure E.2: Quench from the ferromagnetic to the paramagnetic phase

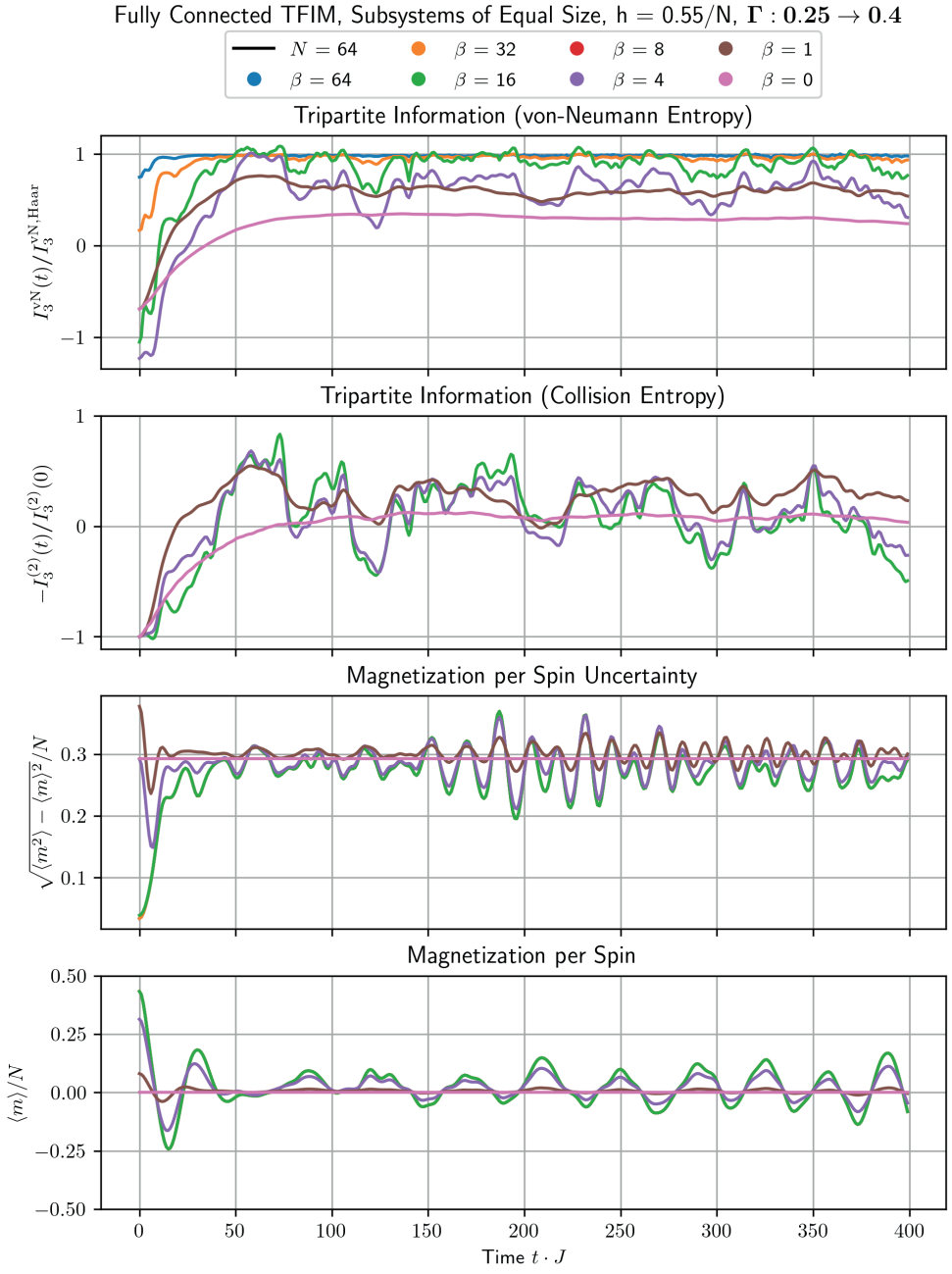

Figure E.3: Quench inside the ferromagnetic phase

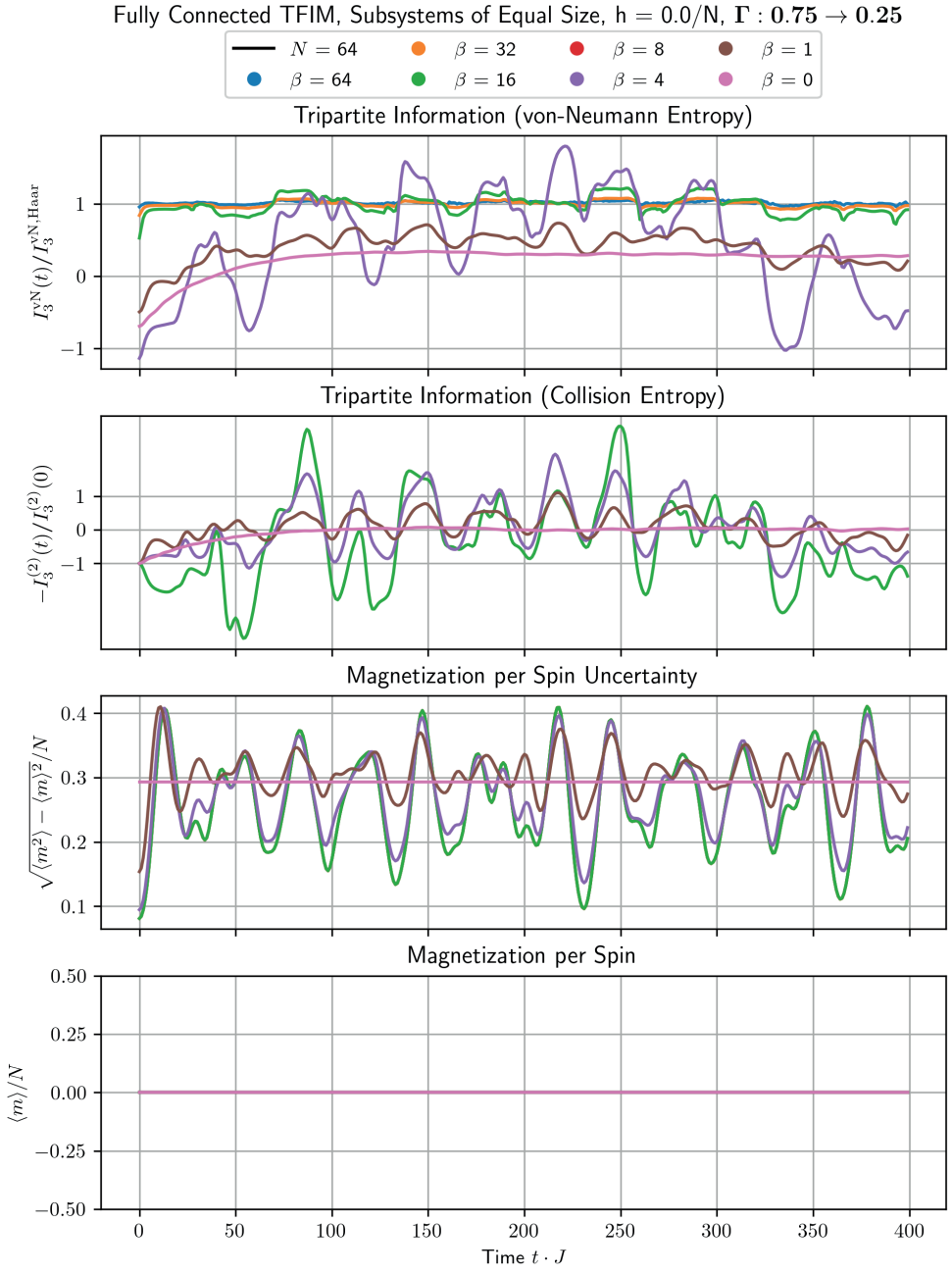

Figure E.4: Quench from the paramagnetic to the ferromagnetic phase

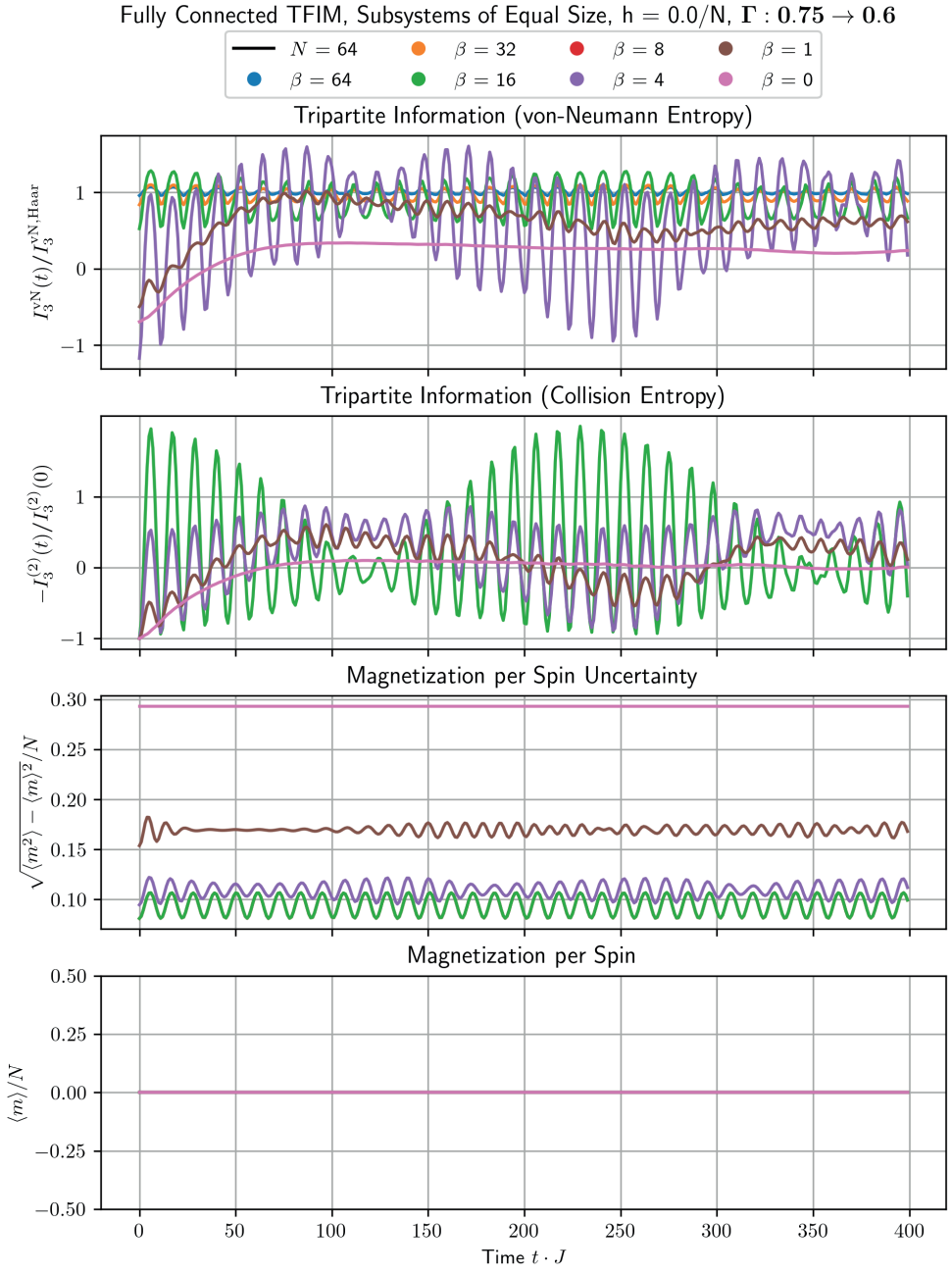

Figure E.5: Quench inside the paramagnetic phase

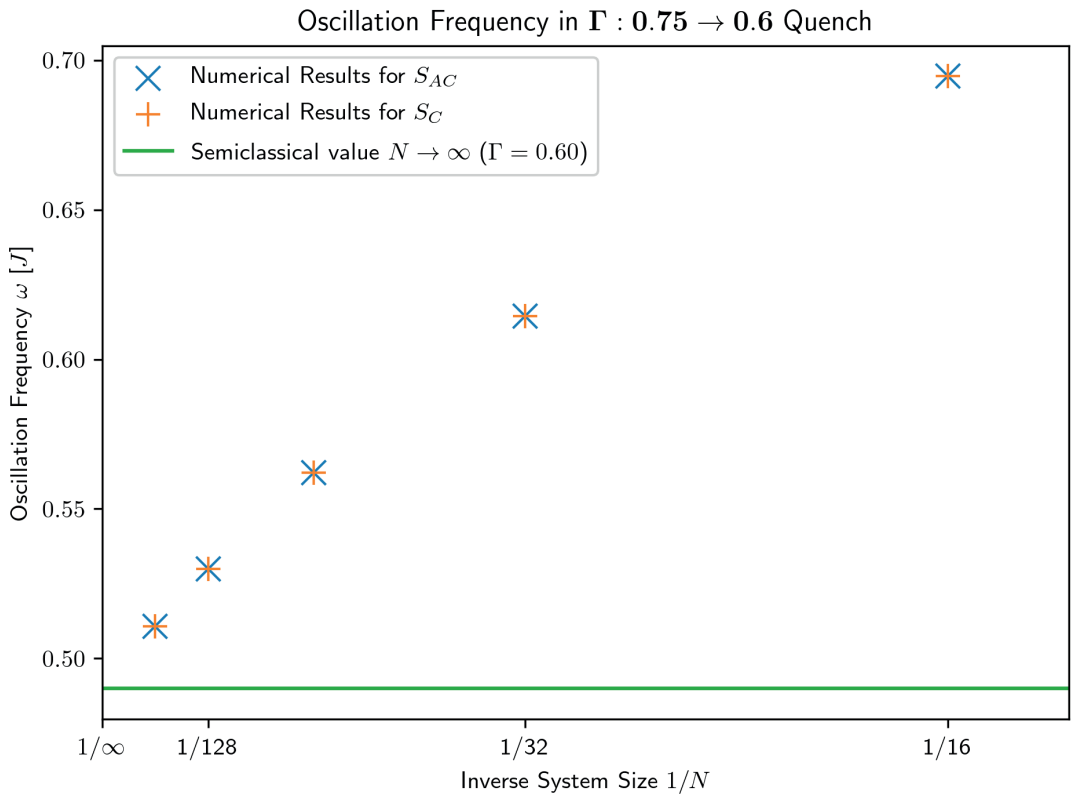

Figure E.6: Frequency of the post-quench oscillations after the quench inside the paramagnetic phase compared to the frequency of the semi-classical results